

The VTTVIS line imaging spectrometer - principles, error sources, and calibration

Jørgensen, Rasmus Nyholm

Publication date:
2002

Document Version
Publisher's PDF, also known as Version of record

[Link back to DTU Orbit](#)

Citation (APA):
Jørgensen, R. N. (2002). The VTTVIS line imaging spectrometer - principles, error sources, and calibration. (Denmark. Forskningscenter Risoe. Risoe-R; No. 1302(EN)).

DTU Library

Technical Information Center of Denmark

General rights

Copyright and moral rights for the publications made accessible in the public portal are retained by the authors and/or other copyright owners and it is a condition of accessing publications that users recognise and abide by the legal requirements associated with these rights.

- Users may download and print one copy of any publication from the public portal for the purpose of private study or research.
- You may not further distribute the material or use it for any profit-making activity or commercial gain
- You may freely distribute the URL identifying the publication in the public portal

If you believe that this document breaches copyright please contact us providing details, and we will remove access to the work immediately and investigate your claim.

The VTTVIS Line Imaging Spectrometer - Principles, Error Sources, and Calibration

Rasmus Nyholm Jørgensen

*Plant Nutrition and Soil Fertility Laboratory, Department of Agricultural Sciences, The Royal Veterinary and Agricultural University
DK-1871 Frederiksberg C (Copenhagen), Denmark*

Present address:

*Plant Environment Interactions, Plant Research Department, Risø National Laboratory, DK-4000 Roskilde, Denmark
e-mail: Rasmus.Joergensen@risoe.dk*

**Risø National Laboratory, Roskilde
February 2002**

Abstract

Hyperspectral imaging with a spatial resolution of a few mm² has proved to have a great potential within crop and weed classification and also within nutrient diagnostics. A commonly used hyperspectral imaging system is based on the Prism-Grating-Prism (PGP) principles produced by Specim Ltd. Finland. One of the novel systems based on the PGP spectrograph (VTTVIS) was build by The Department of Agricultural Sciences, AgroTechnology, KVL, Denmark, in 1995. Several other agricultural institutions have now implemented the technology in their research. None of these has published any thoroughly work describing the basic principles, potential error sources, and/or adjustment and calibration procedures. This report fulfils the need for such documentation with special focus on the system at KVL.

The PGP based system has several severe error sources, which should be removed prior to any analysis. Most of the random noise sources can be minimised by carefully selecting high-grade components especially with concern to the camera. Systematic error sources like CCD fixed pattern noise (FPN), CCD photoresponse nonuniformity (PRNU), CCD charge transfer efficiency (CTE), slit width variations, changes in off-axis transmission efficiencies, diffraction efficiencies, and image distortion have a significant impact on the instrument performance. Procedures removing or minimising these systematic error sources are developed and described for the system build at KVL but can be generalised to other PGP based systems.

The know-how achieved is put into perspectives describing novel ideas for a new scanning hyperspectral imaging system and potentials estimating species specific plant performance within a multi cropping system.

Keywords: imaging spectrograph, Inspector V7, image distortion, hyperspectral flat-fielding

ISBN: 87-550-2967-1; 87-550-2969-8 (Internet)
ISSN: 0106-2840

Print: Pitney Bowes Management Services Denmark, 2002

Contents

1	INTRODUCTION	7
2	AIMS.....	10
3	THE PRINCIPLES OF VTT LINE IMAGING SPECTROMETERS	11
3.1.1	<i>The overall system: lens - PGP element - matrix detector</i>	<i>11</i>
3.1.2	<i>An example of a line spectrometer response</i>	<i>12</i>
3.1.3	<i>Using the line imaging technology for crop/weed discrimination.....</i>	<i>13</i>
3.2	THE FRONT LENS.....	13
3.2.1	<i>Demands.....</i>	<i>14</i>
3.2.2	<i>Error sources and correction</i>	<i>14</i>
3.2.2.1	Dispersion	15
3.2.2.2	Spherical aberration.....	15
3.2.2.3	Coma	16
3.2.2.4	Vignetting.....	17
3.2.2.5	Distortion (Melles Griot 1999).....	17
3.2.2.6	Astigmatism (Melles Griot 1999).....	18
3.2.2.7	Reflection and stray light.....	18
3.2.2.8	Errors of higher order due to dirt and scratches.....	19
3.2.2.9	The mesurant is a canopy resulting in multiple focus depths.....	20
3.2.3	<i>Summary.....</i>	<i>21</i>
3.3	THE DISPERSING PGP SPECTROGRAPH.....	22
3.3.1	<i>Lenses.....</i>	<i>22</i>
3.3.2	<i>Entrance slit</i>	<i>22</i>
3.3.3	<i>PGP element.....</i>	<i>23</i>
3.3.3.1	The refractive nature of the prisms	24
3.3.3.2	The disperse nature of the prism.....	24
3.3.3.3	Principles of diffraction transmission gratings	25
3.3.3.4	Putting together the Prism-Grating-Prism element.....	27
3.3.3.5	Housing	28
3.3.4	<i>Summary.....</i>	<i>28</i>
3.4	THE CAMERA UNIT – THE SENSING UNIT	28
3.4.1	<i>The CCD array in brief.....</i>	<i>29</i>
3.4.2	<i>Noise sources.....</i>	<i>31</i>
3.4.2.1	Shot noise.....	31
3.4.2.2	Photon noise	32
3.4.2.3	Charge Transfer Efficiency (CTE)	32
3.4.2.4	Dark current noise	33
3.4.2.5	Pattern noise	33
3.4.2.6	Flat fielding.....	34
3.4.2.7	Reset noise	35
3.4.2.8	Amplifier noise.....	36
3.4.2.9	Quantification noise	36
3.4.2.10	Noise reduction by use of dark frames	36
3.4.2.11	Photon transfer.....	37
3.4.2.12	Signal-to-Noise-Ratio (SNR)	38
3.4.2.13	Pixel binning	39
3.4.2.14	Dynamic range.....	40
3.4.2.15	<i>Summary</i>	<i>40</i>
3.5	LINEARITY OF SPECTRAL RANGE AT THE IMAGING PLANE.....	41
3.6	BENDING OF SPECTRAL LINES AT THE IMAGING PLANE (SMILING).....	42
3.7	DISTORTION OF THE SPATIAL AXIS.....	43
3.7.1	<i>A worst case study of the distortion of the spatial axis.....</i>	<i>44</i>
3.8	DISTORTION OF THE SPECTRAL AXIS	46
3.9	ASSEMBLING THE CAMERA UNIT TO THE PGP SPECTROGRAPH	47
3.9.1	<i>Displacement of the back focal length.....</i>	<i>47</i>
3.9.2	<i>Rotation of the camera unit alias the CCD array.....</i>	<i>48</i>
3.9.3	<i>Twisting of the camera at the assembling point of the VTTVIS.....</i>	<i>48</i>
3.10	SUMMARY AND DISCUSSION	49

4	SPECIFICATIONS OF THE LINE IMAGING SPECTROMETER	51
4.1	THE FRONT LENS	51
4.2	THE VTTVIS PGP UNIT.....	52
4.2.1	<i>The slit.....</i>	53
4.2.2	<i>The lenses.....</i>	53
4.2.3	<i>The PGP-element.....</i>	53
4.2.4	<i>Performance of the VTTVIS based on ray tracing</i>	54
4.2.4.1	Testing linearity of spectral lines at the imaging plane.....	55
4.2.4.2	Testing the bending of the spectral lines at the imaging plane.....	57
4.2.4.3	Fitted equation describing the wavelength at the CCD array	59
4.2.4.4	Smearing of object points at the PGP imaging plane	60
4.2.4.5	Distortion of the spatial axis depending on the wavelength	61
4.3	THE CCD CAMERA UNIT	62
4.4	MOUNTING THE CAMERA TO THE SPECTROGRAPH	64
4.5	THE MEASURING RIG	66
4.5.1	<i>Concerns using doped SpectralonTM as irradiation reference</i>	66
4.6	THE DOCUMENTATION AND CLASSIFICATION CAMERA	67
4.7	SUMMARY	68
5	ADJUSTMENT AND CALIBRATION PROCEDURE	69
5.1	ADJUSTMENT OF THE CAMERA MOUNTING TO THE SPECTROGRAPH	69
5.1.1	<i>The principles of moment analysis.....</i>	69
5.1.2	<i>Axis alignment procedure</i>	71
5.1.2.1	Principles for fine-tuning the axis alignment	71
5.1.3	<i>Back focal length (BFL) adjustment.....</i>	72
5.2	ADJUSTMENT AND FOCUS OF THE FRONT OPTIC	73
5.3	SPECTRAL CALIBRATION PROCEDURES FOR THE VTTVIS SPECTROGRAPH ..	73
5.3.1	<i>Spectral calibration using Hg, He, Cd, and Neon lamps</i>	75
5.3.1.1	The measuring setup	75
5.3.1.2	Pretreatment of the data	75
5.3.1.3	The results after using moment analysis for the peak centre positioning ..	76
5.3.1.4	The spectral calibration for each of the 242 spatial pixel rows	77
5.3.1.5	A general spectral calibration model for the whole CCD array	78
5.3.1.6	Discussion and conclusion	79
5.4	SPECTRAL CALIBRATION BASED ON THE SUN.....	79
5.4.1	<i>Measurement setup</i>	80
5.4.2	<i>Noise reduction and estimation of local minima.....</i>	80
5.4.2.1	Locating common local minima.....	81
5.4.3	<i>Developing the solar calibration procedure</i>	82
5.4.3.1	The final spectral calibration based on the solar spectrum and validation ..	83
5.4.4	<i>Discussion and conclusion.....</i>	85
5.5	HYPERSPECTRAL FLAT-FIELDING OF THE CCD ARRAY.....	85
5.5.1	<i>The measuring setup and data pre-treatment.....</i>	86
5.5.2	<i>Results and discussion.....</i>	87
5.6	AN ALTERNATIVE FLAT FIELDING PROCEDURE	91
5.6.1	<i>Procedure for estimating a normalization image in brief.....</i>	93
5.6.2	<i>Comparison with an earlier normalization image used.....</i>	94
5.7	PROCEDURE CORRECTING PGP IMAGE DISTORTION	94
5.8	SUMMARY	95
6	DISCUSSION	97
7	CONCLUSION.....	100
8	PERSPECTIVES.....	101
8.1	THE APPLICATION BASED ON THIS REPORT	102
8.1.1	<i>Background.....</i>	102
8.1.2	<i>Project outline.....</i>	103
8.1.2.1	Title.....	103
8.1.2.2	Hypothesis	103
8.1.2.3	Aim	103

8.1.3	<i>Specific demands to the hyperspectral imaging system.....</i>	<i>103</i>
8.1.3.1	The Inspector unit.....	103
8.1.3.2	The CCD camera.....	104
8.1.3.3	Assembling the Inspector and CCD camera.....	104
8.1.3.4	Illumination.....	104
8.1.3.5	Varying focus depths.....	105
8.1.3.6	The measuring chamber	105
8.1.3.7	The software.....	106
9	REFERENCE LIST.....	108

Preface

This report has become a significant part of my Ph.D. project with the title: “Development of Line Imaging Spectroscopy as a nitrogen diagnostic tool in field grown winter wheat”. The primary aim was initially to develop and validate a method using line-imaging spectroscopy with a high spectral and spatial resolution for nitrogen diagnostics in winter wheat. However, it was soon realised that there were almost no literature present describing in details the principles, the potential error sources, and how to calibrate the PGP imaging spectrograph I planned to use for my project. Specim Ltd. provides some information on the latter subjects from there website: <http://www.specim.fi/>. However, for research applications, more detailed characterization and documentation of the total imaging system is required. Thus I decided to build up this documentation parallel to the primary aim of my Ph.D. project.

It has been an enriching and sometimes also a frustrating task for me to write this report since every aspect covered has been novel land since my expertise as agronomist is within classical agronomy and definitely not within technical science. Therefore I hope inexperienced people within this area will find this report inspiring creating a good basis for performing scientific projects with PGP based spectrographs still maintaining a critical view on the data delivered by the system.

The Department of Agricultural Science, Agricultural Engineering at The Royal Veterinary and Agricultural University, Denmark is gratefully acknowledged for lending out their line imaging system full time during my Ph.D. project. I also want to thank Product Manager Esko Herrala, Specim Ltd. for the technical support and constructive comments on this report. Furthermore I am grateful to Associated Professor Henning Nielsen, The Royal Veterinary and Agricultural University, Department of Agricultural Sciences for good and fruitful discussions. Tom Schutt, Plant Research International, The Netherlands has been a great inspiration demonstrating his scanning line imaging spectrometer and for commenting this report. Finally, I especially thank all those who read draft copies of the manuscript: Professor, D.Sc., Ph.D. Niels Erik Nielsen, Research Professor Simon Blackmore, and Ph.D. Stud. Lene Krøl Christensen, The Royal Veterinary and Agricultural University, Department of Agricultural Sciences; Professor D.Sc. Gunnar Gissel Nielsen, Risø National Laboratory, Plant Research Department.

Thursday, 28 February 2002

Rasmus N. Jørgensen

1 Introduction

Farmers have for centuries by visible inspection been able to tell how well their crop is performing at different locations within the field. For example a dark green plant is as a rule of thumb performing better than a light green plant. The visual evaluation performed by the farmer is to a large extent relative because the evaluation is based on the color differences within the specific field. The human eye is extremely good in directly comparing color differences but is however not very good in absolute color measurements (Hatfield and Pinter 1993). In other words, if the farmer was asked to evaluate plants one by one without any reference, his capability to separate by color would be significantly reduced.

The human eye and a standard color camera (RGB camera) are in their own way imaging "spectrometers" at the limited visible wavelength region which ranges in wavelength from approximately 400nm to 750nm (Hagman 1996). A human eye registers the basic tristimulus values, which are relatively broad bands, and is capable of separating up to 36,000 different colors. Likewise the RGB camera is designed to register basically the same three bands to be able to differentiate colors and "imitate" the human eye (Spectral Imaging Ltd. 1999b).

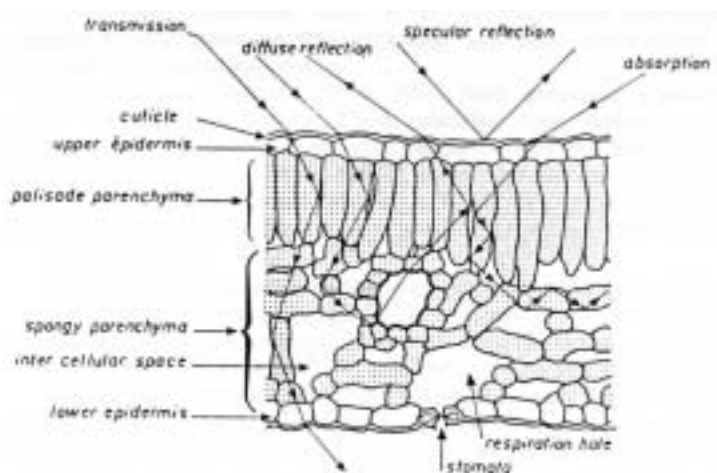


Figure 1: Schematic representation of the interaction of incoming radiation with leaf tissues. (Guyot et al. 1992)

The color of a plant leaf is the end result after the light from the leaf has entered the eye, which integrates the incoming light in three broad spectral bands as mentioned earlier. The light from the leaf is mainly reflected light from an external light source like the sun. Some of the incoming radiation is transmitted and some is absorbed in the leaf depending on the structure and composition of the leaf as illustrated in Figure 1. Therefore, the composition of the reflected light entering the eye is a code telling something about the leaf composition.

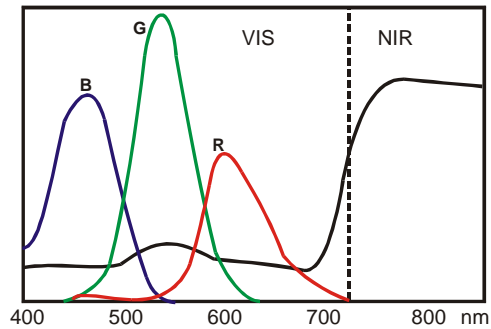


Figure 2: Schematic illustration of a typical reflection spectrum of a green plant in the visual (VIS) and near infrared (NIR) range of light when illuminated by the sun. The three graphs (R, G, B) illustrate how an RGB camera integrates light from three broad bands centred on red (650 nm), green (530 nm), and blue (460 nm) simulating the human color vision. (After (Guyot et al. 1992; Searcy 1989))

However studying Figure 2 it becomes clear that the information contained in the three broad bands are rather limited when compared to the character of a leaf reflectance spectra in the visual and near infrared light. One way to obtain the 'true' reflectance spectrum is to use a spectrophotometer, which is able to measure both VIS and NIR in very narrow bands. A standard spectrophotometer is usually only able to measure from a small integrated area at a time. This means that if one wants to measure the optical spectrum from different spatial locations of an object, either the measuring instrument or the target has to be moved or scanned (Spectral Imaging Ltd. 1999b). By using a spectrometer, valuable spectral information can be achieved, but the spatial or imaging information is lost. Therefore an imaging spectrometer is needed.

Then, how to realise an imaging spectrometer in practise? Basically, some kind of component capable of separating different wavelengths (prism, grating or filter), optics which are used to image spatial features and a detector for measuring the acquired image. The possibilities are limited considering the present available components and their properties. Technically it is not possible, by using a standard 2D CCD matrix element¹ to measure simultaneously the 2 - dimensional surface as a matrix plane (X, Y -plane) and the spectrum components with high resolution and the intensity of each spectral element. However, it is possible to measure the spatial information from a line (with specified length and small but finite width) and the spectral information from equally spaced points on this line. In this way the other dimension of the CCD array retains its spatial function but the other axis is used to record the spectrum in each spatial point! The resulting image from the target is certainly limited, just one narrow line, but still it is much more than just a point (Spectral Imaging Ltd. 1999b).

¹ A semiconductor chip with a grid of light-sensitive elements, used for converting light images, as in a television camera, into electrical signals.

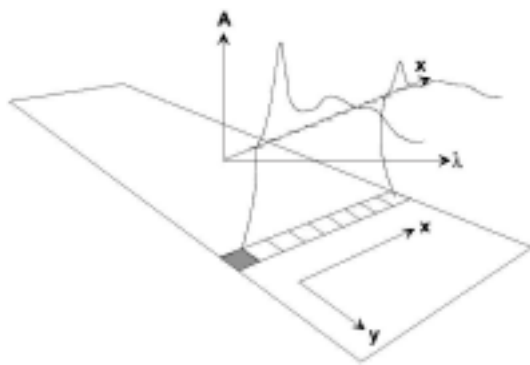


Figure 3: Imaging spectroscopy (spectral imaging) across a two dimensional plate. An area detector is able to register position in the X -coordinate axis, wavelength and intensity. The Y-axis of the plate is measured by acquiring line images while moving the plate in the Y-direction (Spectral Imaging Ltd. 1997).

Equipment using the latter principles has been designed and manufactured by VTT, Finland, now commercialised by Spectral Imaging or Specim Ltd. (www.specim.fi) (Hyvarinen et al. 1998).

The Department of Agricultural Sciences, AgroTechnology, KVL, Denmark, has since 1995 been working with the line imaging spectrometer technology from VTT. The main focus has been on crop/weed discrimination and it has been proven that this technology is capable of this kind of discrimination (Bennedsen and Rasmussen 2001; Borregaard 1997; Borregaard et al. 2000). F. Feyaerts and L. van Gool (2001) have in recent work shown the great potential of using a line imaging spectrometer for crop/weed discrimination under field conditions. In 1998 R. N. Jørgensen, KVL Denmark, started a Ph.D. project using the line imaging spectrometer equipment at the Department of Agricultural Sciences, KVL, with the aim of establishing a nitrogen index in winter wheat grown under natural conditions. Preliminary results made in corporation with the Department of Agricultural Sciences, KVL, indicate great potential within this area (Nielsen et al. 1999). During this work it was realised that the software included with the cameras mounted at the two linespectrometer units could only control one camera unit at the time. Furthermore, it was not possible to take a digital photo simultaneously with the linespectrometer, since all sampling units used individual controlling software. Finally a GPS position stored together with the measurements could ease the organisation of the data significantly.

During this work it was realised that systematic documentation describing the equipment at KVL was lacking. It was therefore decided to manufacture such material creating the knowledge base describing the following points.

- The principles of the line imaging spectrometer
- Potential error sources
- Technical description of the specific system at KVL
- Adjustment and calibration of the line imaging spectrometer

2 Aims

The first aim of this report is to gain insight by giving a detailed description of the VTTVIS line imaging spectrometer used at The Department of Agricultural Sciences, AgroTechnology, KVL, Denmark, for measurements in the visual wavelength range.

The second aim is to describe potential error sources of the VTTVIS line imaging spectrometer system.

The third aim is to develop procedures for adjusting and calibrating the VTTVIS line imaging spectrometer system.

3 The principles of VTT line imaging spectrometers

This section will briefly describe the elements the line imaging spectrometers consists of. Initially the overall system will be described and hereafter the sub-elements. Within each of the components used in the spectrometer there will be potential error sources, which must be taken into consideration when calibrating and evaluating the performance of the line imaging spectrometer.

3.1.1 The overall system: lens - PGP element - matrix detector

The overall system of the VTTVIS line imaging spectrometer from VTT², Finland, consists of three main parts a front lens, a spectrograph, and a Charge Coupled Device (CCD) camera.

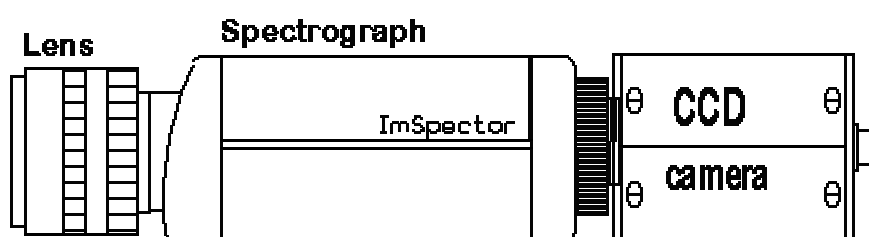


Figure 4: Sketch of the overall system (Spectral Imaging Ltd. 1999b).

The front lens brings the plant or leaf into focus at the entrance into the spectrograph. The spectrograph only allows a narrow line of the object to pass by use of an entrance slit. Within the spectrograph the rays from the narrow line of the object is dispersed according to its spectral composition.

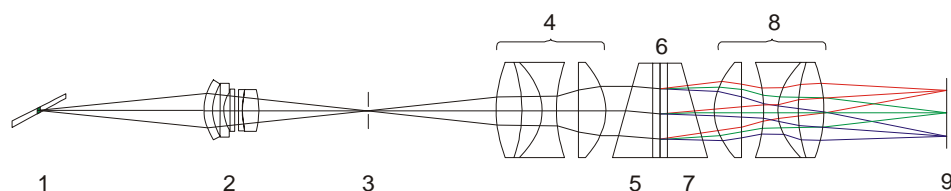


Figure 5: Imaging spectroscopy. Sketch of the overall system from the light leaves the measurant till it gets separated according to wavelength and finally focused at the imaging plane. 1 ~ object line at the measurant; 2 ~ front lens; 3-8 ~ the PGP spectrograph; 3 ~ entrance slit; 4 ~ collimating lens; 5 & 7 ~ symmetric prisms; 6 ~ grating; 8 ~ focusing lens; 9 ~ imaging plane. (after Aikio (1994; 1995)).

² VTT, Finland, produces new applied technology in cooperation with domestic and foreign partners. The number of our employees is about 3000. Turnover is about 200 million euros.

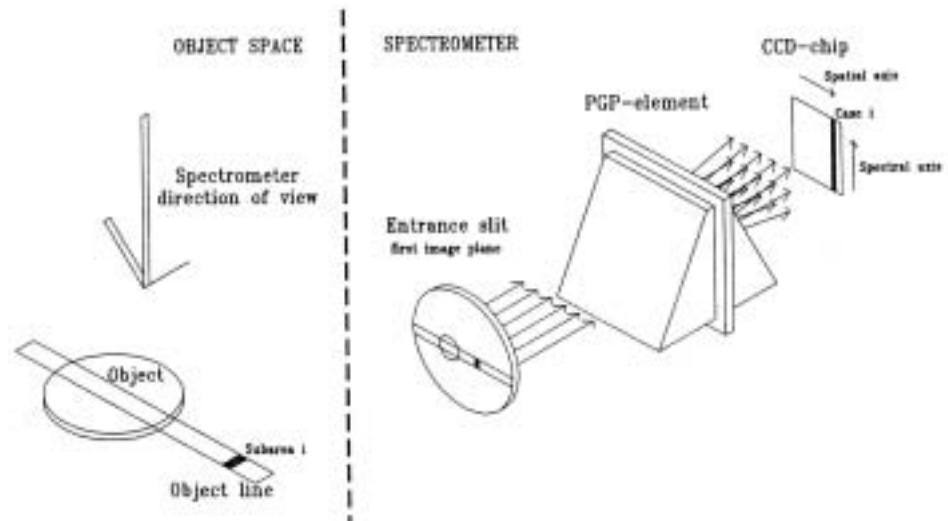


Figure 6: Schematic representation of line imaging spectroscopy. The spectral response of sub area i, dispersed by PGP-element, is depicted onto the CCD in row i as in the image (Borregaard 1997).

The dispersed line forms a 2D matrix consisting of spatial and a spectral axis, which reach the matrix detector in form of a CCD camera. Each pixel measures the light intensity according to the spatial position and spectral location.

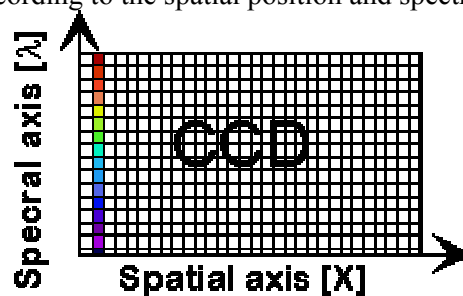


Figure 7: Spatial and spectral representation of the dispersed object line depicted onto the CCD matrix detector (Spectral Imaging Ltd. 1999b).

3.1.2 An example of a line spectrometer response

Place a color sample target made of paper as in the figure below and measure the narrow line marked in the middle using a PGP spectrograph and a B/W camera having 384 (V) x 286 (H) elements.

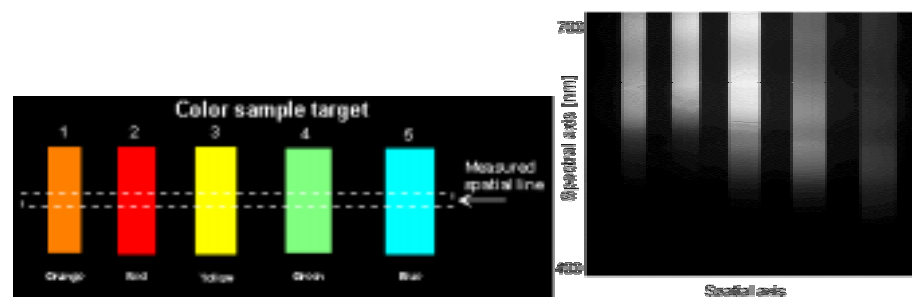


Figure 8: A colour sample target measured by a line imaging spectrometer and an illustration of the resulting CCD response. Black on the CCD matrix detector represents low radiation intensity and white represents high intensities.

This single measurement results in a spatial/spectral map as presented in Figure 8 right. The image is naturally a grey scale because it is measured with a B/W camera. The horizontal axis represents now the single narrow spatial line and can easily be recognised to have similar to the target. Each coloured area gives distinctive reflection spectrum at the vertical axis and the black areas are of course black (Spectral Imaging Ltd. 1999b).

This is an uncorrected image so the typical behaviour of common halogen light source and drop of CCD response in the blue end can be seen as lower intensity level (see also 5.5 on page 85).

3.1.3 Using the line imaging technology for crop/weed discrimination

Studying Figure 8 it becomes not surprisingly clear that it is possible to do colour separation. This technology has as mentioned in the introduction made it possible to discriminate between plant species. The principle is illustrated in the figure below.

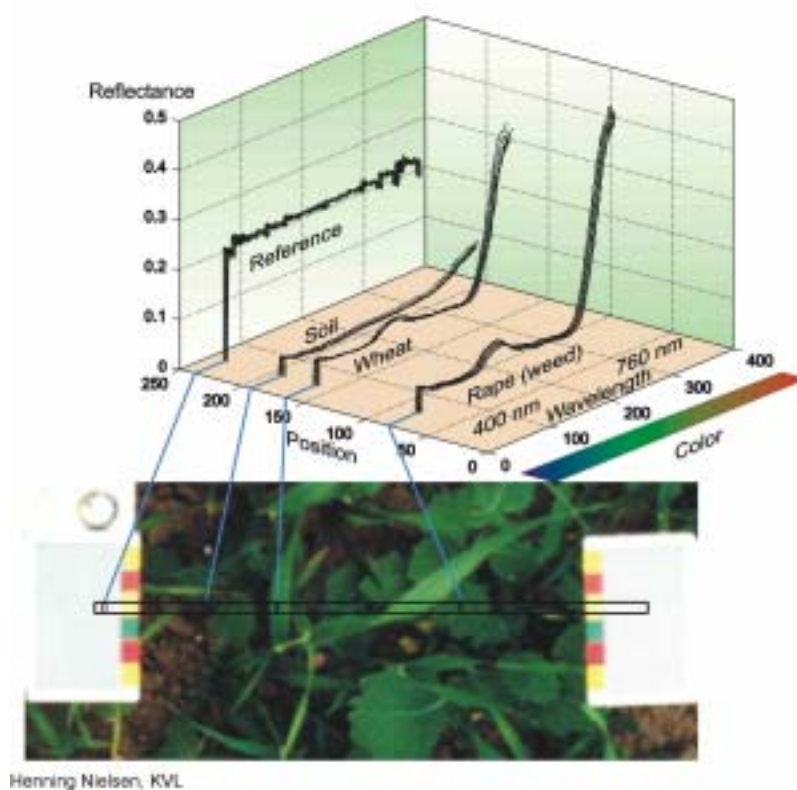


Figure 9: Schematic representation of using the VISVTT line spectrometer for crop/weed discrimination.

Note that in order to obtain a good discrimination between soil, crop, and weeds the near infrared region should also be used (Hahn and Muir 1993).

3.2 The front lens

The function of the front lens mounted on the PGP is to collect and focus the reflected light, from the measured object e.g. a leaf, onto the entrance slit at the PGP element. Due to the nature of light when passing through media's with different optical densities like air to glass to air the construction of a lens with minimum errors is a complicated task.

The speed of light depends on the media it passing through. In vacuum the speed of light is approx. $300,000 \text{ km s}^{-1}$. In atmospheric air the speed is reduced a little and the air is therefore said to have a higher optical density. In glass the speed of light is reduced to $150,000\text{-}200,000 \text{ km s}^{-1}$. Due to the wave nature of light the direction of a light beam will change direction when passing from a media with one specific optical density to a media with another optical density. This phenomenon is referred to as light refraction. The degree of deflection depends on the angle of incidence, the wavelength, and the difference in optical density. The latter can be used for wavelength separation of light by use of prisms but it can also be used for collecting light by use of lenses. Since the deflection of light depend on several factors it is a rather complicated task to focus light into a point if consisting of several wavelengths from one point source and with different angle of reflections (Frenning 1984; Melles Griot 1999).

In the following subsections the needed demands to such a lens setup will be discussed together with possible error sources and ways to overcome these.

3.2.1 Demands

As mentioned earlier the main purpose of the front lens is the collect and concentrate reflected light from the measurant focussing it at the front end plate containing the entrance slit to the PGP-element. Since the idea of using a line imaging spectrometer is to quantify spectral composition of reflected light from several small areas along a narrow line some overall demands can be set for the front-end lens.

- The reflected light from a specific point of the measurant must have a common focal point for the whole width of wavelengths entering the PGP-element through the entrance slit
- It must be possible to mount the lens at the PGP-element so that the optical axis is orthogonal and centred at the entrance slit of the PGP
- Since the reflected light beam is separated according to wavelength when passing the PGP a high light intensity is needed. Therefore a high transmission of the front-end lens is needed
- Accurate and precise adjustment of focus and stop number should be possible according to scale displays at the lens. Furthermore screws for securing the sitting should be present
- The lens must be robust so that it can withstand outdoor conditions and vibrations due to transport
- The lens surface facing the surroundings must be hard so that it is possible to do cleaning without making scratches

3.2.2 Error sources and correction

A simple lens has besides the prior mentioned color dispersion several other error sources, which counteract the formation of an unsmeared picture. These error sources are normally referred to as the 7 lens errors (Frenning 1984).

1. Dispersion (also called chromatic aberration or color dispersion)
2. Spherical aberration
3. Coma
4. Vignetting
5. Distortion
6. Astigmatism
7. Reflection and stray light

In the following these 7 lens error and correction of these will be discussed briefly. Furthermore two additional error sources need to be considered. 1: Under field conditions the lens surface becomes dirty and scathed causing errors of higher order. 2: The measurant is a canopy resulting in multiple focus depths.

3.2.2.1 Dispersion

When a beam of white light hits a lens parallel to the optical axis the light is refracted different according to wavelength. The focal point of the blue (short waved) is closer to the lens compared to the focal point of the red light with a longer wavelength (Frenning 1984; Melles Griot 1999). This is also referred to as longitudinal chromatic aberration as illustrated in Figure 10.

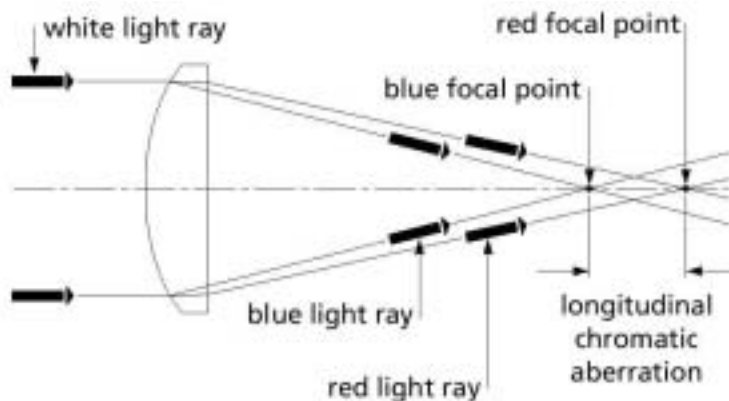


Figure 10: Longitudinal chromatic aberration (Melles Griot 1999).

The color dispersion can be neutralised by using compounded objectives consisting of two lenses with different properties. One lens consists of a material with a low refraction and a high degree of color dispersion and the other consist of a material with a high refraction and a low degree of color dispersion. This system will by proper combination give a common focal point and is referred to as a two-element achromat.

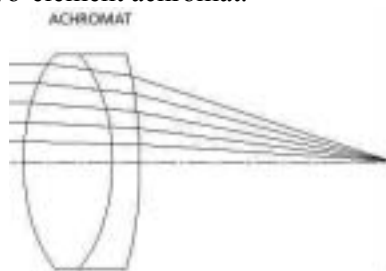


Figure 11: A two-element achromat (Melles Griot 1999).

3.2.2.2 Spherical aberration

When a symmetric convex lens focuses collimated incoming light then the further away from the optical axis the ray enters the lens, the nearer to the lens it focuses (crosses the optical axis). The distance along the optical axis between the intercept of the rays that are nearly on the optical axis (paraxial rays) and the rays that go through the edge of the lens (marginal rays) is called longitudinal spherical aberration (LSA). The height at which these rays intercept the paraxial focal plane is called transverse spherical aberration (TSA) (Melles Griot 1999).

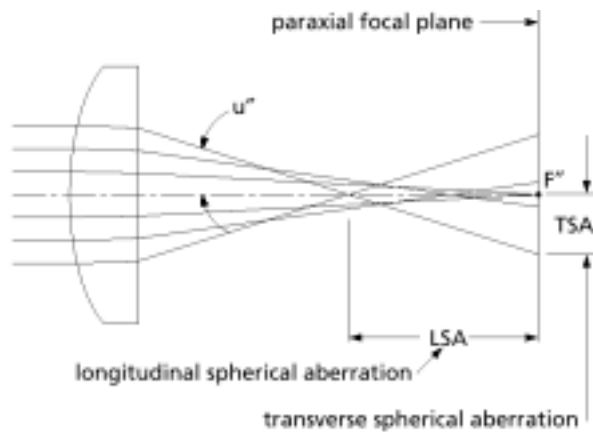


Figure 12: Spherical aberration of a plano-convex lens (Melles Griot 1999).

Spherical aberration is dependent on lens shape, orientation, and conjugate ratio, as well as on the refraction of the materials present.

In a single spherical lens the error will be smallest if both lens surfaces take equal part in the refraction of the light. Theoretically, the simplest way to eliminate or reduce the latter problem is to make lens surface(s) with a varying radius of curvature (i.e., an aspheric surface) (Melles Griot 1999) like when the rear lens surface has a radius for a sphere surface which is 6 times the radius for the front lens surface (Frenning 1984).

The manufacture of aspheric surfaces is more complex, and it is difficult to produce a lens of sufficient surface accuracy to eliminate spherical aberration completely. Fortunately, these aberrations can be virtually eliminated, for a chosen set of conditions, by combining the effects of two or more spherical (or cylindrical) surfaces (Melles Griot 1999).

3.2.2.3 Coma

In spherical lenses, different parts of the lens surface exhibit different degrees of magnification. This gives rise to an aberration known as coma. As shown in Figure 13, each concentric zone of a lens forms a ring-shaped image called a comatic circle. This causes blurring in the image plane (surface) of off-axis object points. An off-axis object point is not a sharp image point, but it appears as a characteristic comet-like flare. Even if spherical aberration is corrected and the lens brings all rays to a sharp focus on axis, a lens may still exhibit coma off axis (Melles Griot 1999). An example of coma is shown in Figure 51 on page 55 where a comet-like flare shows up as the distance from the slit centre increase.

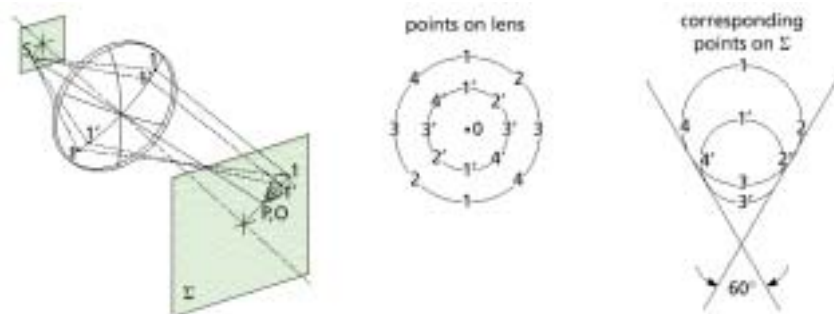


Figure 13: Imaging an off-axis point source by a lens with positive transverse coma (Melles Griot 1999).

As for spherical aberration the coma error is decreasing at increasing stop numbers (<http://www.britannica.com/>, 1999-12-15). In compound objectives

coma is reduced by choosing the single lens elements in such a way that coma errors in one lens element is cancelled by the opposite error in another lens element. Especially in symmetrical constructions of compound objectives coma can be reduced significantly by the latter solution (Frenning 1984).

3.2.2.4 Vignetting

The mounts of some of the lens elements cut into the oblique beams and the edges along the image plan is then not fully filled with light. This effect is known as vignetting and leads to a reduction in illumination in the outer parts of the field of view.

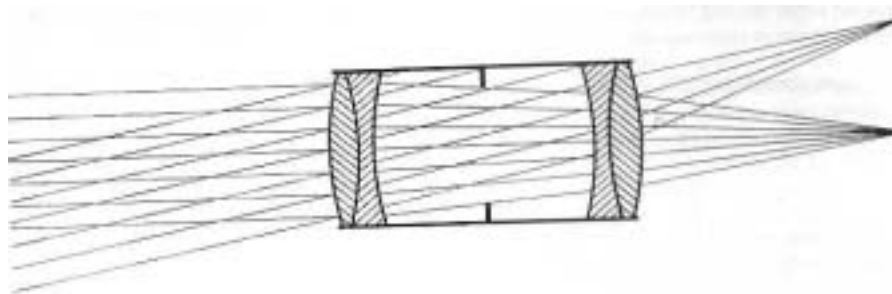


Figure 14: Cause of vignetting in long objective constructions (Frenning 1984).

Correction of vignetting can be done by at increasing stop numbers and/or by building the objective as short as possible (Frenning 1984).

3.2.2.5 Distortion (Melles Griot 1999)

The image field not only may have curvature but may also be distorted. The image of an off-axis point may be formed at a location on this surface other than that predicted by the simple paraxial equations. This distortion is different from coma (where rays from an off-axis point fail to meet perfectly in the image plane). Distortion means that even if a perfect off-axis point image is formed, its location on the image plane is not correct. Furthermore, the amount of distortion usually increases with increasing image height. The effect of this can be seen as two different kinds of distortion: pincushion and barrel (see Figure 15). Distortion does not lower system resolution; it simply means that the image shape does not correspond exactly to the shape of the object. Distortion is a separation of the actual image point from the paraxially predicted location on the image plane and can be expressed either as an absolute value or as a percentage of the paraxial image height.

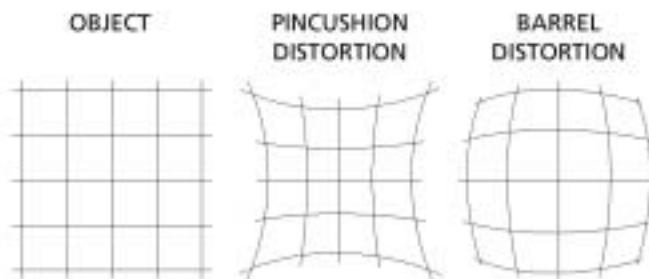


Figure 15: Pincushion and barrel distortion

It should be apparent that a lens or lens system has opposite types of distortion depending on whether it is used forward or backward. This means that if a lens were used to make a photograph, and then used in reverse to

project it, there would be no distortion in the final screen image. Also, perfectly symmetrical optical systems at 1:1 magnification have no distortion or coma.

3.2.2.6 Astigmatism (Melles Griot 1999)

When an off-axis object is focused by a spherical lens, the natural asymmetry leads to astigmatism. The system appears to have two different focal lengths. As shown in Figure 16, the plane containing both optical axis and object point is called the tangential plane. Rays that lie in this plane are called tangential rays. Rays not in this plane are referred to as skew rays. The chief, or principal, ray goes from the object point through the centre of the aperture of the lens system. The plane perpendicular to the tangential plane that contains the principal ray is called the sagittal or radial plane.

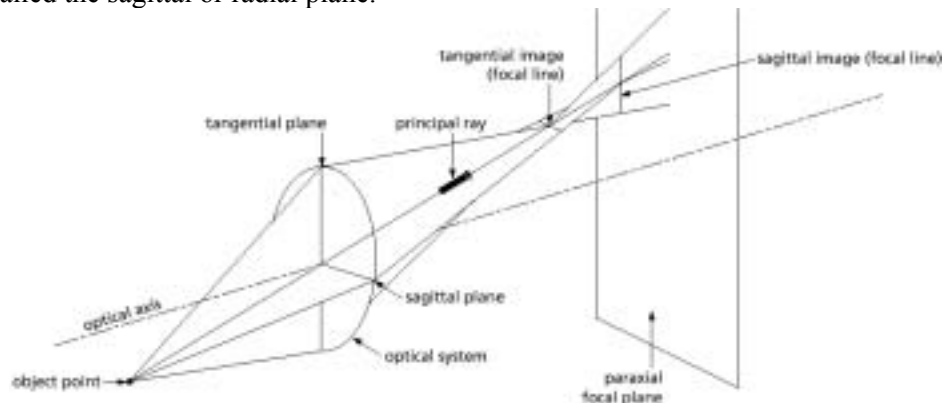


Figure 16: Astigmatism represented by sectional views (Melles Griot 1999).

The figure illustrates that tangential rays from the object come to a focus closer to the lens than do rays in the sagittal plane. When the image is evaluated at the tangential conjugate, we see a line in the sagittal direction. A line in the tangential direction is formed at the sagittal conjugate. Between these conjugates, the image is either an elliptical or a circular blur. Astigmatism is defined as the separation of these conjugates.

The amount of astigmatism in a lens depends on lens shape only when there is an aperture in the system that is not in contact with the lens itself. (In all optical systems there is an aperture or stop, although in many cases it is simply the clear aperture of the lens element itself). Astigmatism strongly depends on the conjugate ratio.

In order to obtain a good correction of astigmatism at least 3 or preferably more lenses must be used plus at least one of these must have a high degree of refraction and a low degree of color dispersion (Frenning 1984).

3.2.2.7 Reflection and stray light

When light passes from one optical medium to another (especially from air to glass and vice versa in a lens), about 4 to 8 percent of it is lost by reflection at the interface. This light loss builds up appreciably in complex multielement lenses. Some of the reflected light still reaches the film as ghost images or light spots or as general contrast-reducing scattered light (<http://www.britannica.com/>, 1999-12-15).

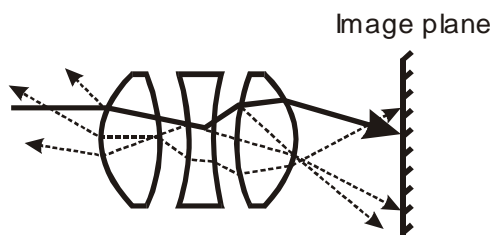


Figure 17: Secondary reflections can find their way back to the image plane, where they form ghost images. The full line illustrates the incoming ray and punctuated lines are the primary and secondary reflections.

To reduce such losses, the air-to-glass surfaces of modern lenses typically carry a microscopically thin coating of metallic fluorides. The coating eliminates most reflected rays as illustrated in Figure 18. Complete elimination can occur only for light of one wavelength if the coating thickness and refractive index are exactly right. In practice a coated lens surface reflects about 0.5 percent of incident white light and approx. 10% of the light lost by an uncoated lens. Multiple coatings can reduce reflections over a wider spectral range (<http://www.britannica.com/>, 1999-12-15). The effect of stray light or light scattering is also reduced within objectives and PGP spectrographs by blackening the inside of the housing and by placing baffles between the lenses. This is illustrated for a PGP spectrograph with two vertical lines at the horizontal centre of Figure 21 on page 22 (Spectral Imaging Ltd. 2000).



Figure 18: Example of stray light causing poor image quality to the left and to the right the improved image after using anti-reflective coatings eliminating stray light (www.zeiss.de 2002).

Stray light is an important artefact and should not be neglected. There are two main types in the VTTVIS systems. Fore optics stray light causes only spatial deterioration whereas stray light inside the spectrograph causes both spatial and spectral deterioration [Esko Herrala, Specim, *pers. comm.* 2002).

3.2.2.8 Errors of higher order due to dirt and scratches

When the line imaging spectrometer is used in the laboratory or in the field the outermost lens surface of the front-end lens is exposed to dust, condensation creating films and potential scratching when cleaning. Dust particles will reflect some light but it will also diffract some causing stray light. Depending on the composition, thickness, and the form of the film the light passing will to some degree be spread depending on angle of incidence and wavelength. Such a film spread at small areas at the lens surface can almost be considered as an extra sparse coating causing unpredictable errors. Scratches in the lens surface will result in diffraction of light resulting in undesirable stray light.

The simplest way to avoid the latter errors is to keep the lens surface clean and without scratches. Of course these error can also be present at the internal lens surfaces, but a proper selection of a high quality lens should negligible this.

3.2.2.9 The measurant is a canopy resulting in multiple focus depths

As illustrated in Figure 9 on page 13 the line imaging spectrometer is looking orthogonal at a canopy along a narrow line which depending on slit width, distance to object, and the resolution of the camera splitting the line up in rectangles as illustrated in Figure 19. However since the canopy is not a plane surface the distance from the lens to a canopy point within the object line will not be constant. The focal point at the entrance slit at the PGP element will consequently also change.

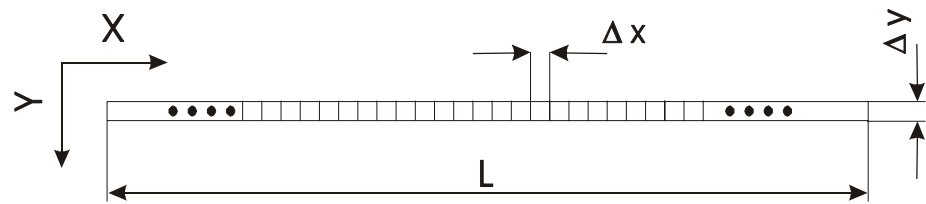


Figure 19: Schematic representation of an object line of length L with a number of subareas ($\Delta A = \Delta x \Delta y$) along the line (Borregaard 1997).

Therefore the focal point at the entrance slit is no longer a point but an area of various size. This area is referred to as "circle of confusion" as illustrated in Figure 20. As long as the diameter of the circle of confusion is less than Δx (see Figure 19) which is the pixel width in the CCD array the image will seem to be in focus. But when the diameter of the circle of confusion is larger than Δx the contrast will decrease. In the orthogonal direction Δy an increase in the diameter of the circle of confusion will allow reflected light from areas parallel to the object line to merge with the reflected light from the object line.

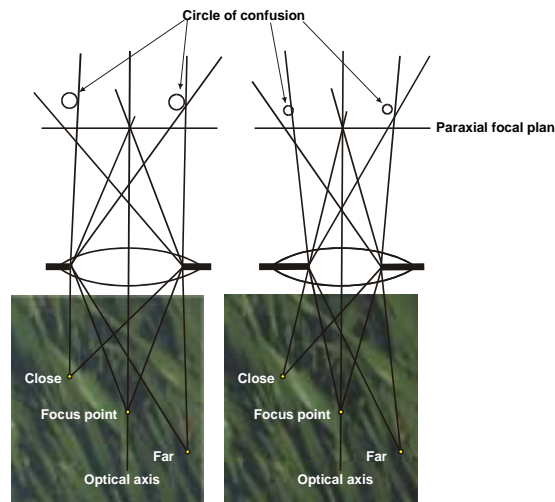


Figure 20: Schematic illustration of the effect to the focus on the paraxial focal plan when trying to image a canopy. The lens has full aperture and is stopped down to the left and right, respectively. The distance from the lens to canopy imaging points vary and the resulting focal distances do not fit with the paraxial focal plan. The canopy imaging point, which is not in similar distance as the focus point, is therefore spread in a circular area at the paraxial focus plan and is referred to as the circle of confusion.

Taking the latter into consideration there will be a certain range of depth where the canopy is in focus according to the maximum size of the circle of confusion. This range depend on following factors:

- The amount of sharpness loss regarded as acceptable alias the circle of confusion
- The lens aperture used
- The distance to the object point in perfect focus
- The focal length of the lens

The near and far distance from the lens enclosing this range can be determined using the following equations:

$$ND = \frac{FL^2 \cdot d}{FL^2 + f \cdot d_c (d - f)} \quad , \quad FD = \frac{FL^2 \cdot d}{FL^2 - f \cdot d_c (d - f)}$$

ND : Near Distance

FD : Far Distance

FL : Focal Length

d : Distance between the object in focus and the front lens

f : Aperature

d_c : Circle of confusion diameter

Equation 1: The near and far distance from the front lens enclosing the range where the amount of focus loss regarded as acceptable alias the circle of confusion.

If for example the focal length is 35mm, the object distance 1 metre, the aperture number 5.6, and the circle of confusion diameter is 1/20 mm then range from the lens to the object with acceptable sharpness is from 0.82 meter till 1.28 meter.

When imaging a canopy it is therefore important not to focus the line imaging spectrometer at the leaves closest to the lens but further down the canopy. The distance to focus on should therefore by the distance from the lens till the closest leaf plus half the difference between ND and FD in Equation 1.

3.2.3 Summary

It is clear there are several error sources, which can introduce noise into the image or the line projected at the entrance slit of the PGP-element. Fortunately most of them can be avoided or at least minimised by carefully selecting a high quality lens. However the operator must be aware of keeping the lens surface clean of dust, condense films, and scratches. The varying focus depth measuring a canopy from a nadir position cannot be removed. Therefore the individual sub areas (~ horizontal pixels at the CCD array) along the object line will vary in size. Using a CCD camera the circle of confusion should not exceed the width of one pixel. Studying Equation 1 the most efficient way the increase the range of acceptable focus is to increase the distance to the canopy.

3.3 The dispersing PGP spectrograph

The operating principle of the dispersing PGP spectrograph is illustrated in Figure 21. The PGP is composed of a specially designed volume transmission plane grating made of dichromated gelatine (DCG) and cemented between two symmetrical or nearly symmetrical prisms. The grating is designed to operate under Bragg condition and the prism angles change accordingly. A collimated light beam is dispersed passing the PGP so that the central wavelength passes axially through the grating and prisms. Shorter and longer wavelengths are dispersed symmetrically on both sides of the central wavelength (Herrala et al. 1994a; Herrala and Okkonen 1996; Spectral Imaging Ltd. 1997).

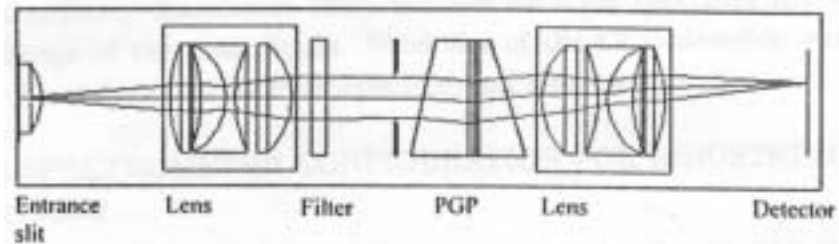


Figure 21: Basic optical principle of the PGP spectrograph. Raytrace for one color is shown (Herrala and Okkonen 1996).

3.3.1 Lenses

There are two high quality triplet lenses in the dispersing PGP spectrograph. They are used to collimate light to the dispersing PGP element and to focus light to the detector surface of the CCD camera, respectively. These lenses are specially designed for a wide field of view and a low f-number. Furthermore they provide a high image quality by reducing several common aberrations mentioned in section 3.2 on page 13 (Spectral Imaging Ltd. 1997). There is however some loss of resolution due to chromatic aberration induced by the use of refractive optics, primarily by the first collimating lens, but this can be minimised by a proper lens selection (Herrala and Okkonen 1996).

As mentioned earlier any tubular optics is sensitive to ghost images caused by reflections in the optical surfaces (Herrala and Okkonen 1996) and it is therefore important to minimise the lens reflection by use of multiple broad band coatings at the lens surfaces. Further the reflection between the lenses and the PGP dispersing element is minimised by use of baffles inside the tube of the PGP spectrograph (Herrala et al. 1994a; Herrala and Okkonen 1996).

3.3.2 Entrance slit

The spectral resolution of the spectrograph depends on the width of the entrance slit, the pixels size or sample density of the CCD element, and the linear dispersion produced by the spectrograph optics. Minimum limit for the spectral resolution is set by the imaging capability of the optics (point of spread size). The input slit is lithographically manufactured on a glass substrate. Thus, there is physical hole to the inner parts of the spectrograph (Spectral Imaging Ltd. 1997).

The optical bandwidth corresponding to the slit width covers a line area on the detector, which has the same width as the slit. If increased scene line width is allowed, it is advantageous (for minimising required light power) to use as wide a slit as the optical resolution allows. Furthermore, for maximum S/N, the number of pixel lines corresponding to slit width can always be averaged (either

by binning or software summing) without deteriorating the spectral resolution or increasing the scene line width (Hyvarinen et al. 1998; Spectral Imaging Ltd. 1997; Spectral Imaging Ltd. 1999a).

If broader spectral resolution than the resolution defined by the slit is sufficient, but a broader slit cannot be used due to line width requirement, the number of pixel lines corresponding to the required spectral resolution can be averaged. As an example, if the line width requires 80 μm slit, but optical resolution of 10 nm is sufficient, and pixel size is 10 μm , each 16 successive lines can be averaged producing S/N improvement of $16^{1/2} = 4$ (Spectral Imaging Ltd. 1999a). However due to the discrete nature of the CCD chip the minimum slit width should be 3 times the smallest pixel size if possible (Borregaard 1997).

The slit can cause direct error and/or calibrations problems of the projected spectral image at the CCD chips. These will briefly be described:

- When light has passed the front lens only a narrow slit of light is allowed to enter the PGP disperse element. The remaining light absorbed in the glass containing the slit. However some of the blocked light is reflected back onto the rear surface of the rear lens in the front optics and then back into PGP disperse element through the entrance slit as observed by T. Borregaard (1997). The impact of the latter can be minimised by blackened the environment of the entrance slit and by partly blackened the back-surface of front objective (Borregaard 1997).
- Varying slit width across the spatial direction results in an uneven intensity of light entering dispersing PGP spectrograph in the spatial direction of the object line. Consequently the width object line will also vary. The latter will also affect the spectral resolution since resolution depends on the slit width. Interpretation of spectral peak condition along the spatial axis will be highly sensitive to an uneven spectral resolution. Consequently the demands to the lithographically manufacturing of the slit on a glass substrate must be very high especially at narrow slit widths. According to Esko Herrala this has been minimised in Specim Instruments (Esko Herrala, Specim, *pers. comm.* 2002).
- The edges of the slit will cause diffraction of the outer part of the light beam entering PGP (Alonso and Edward 1972a; Eisberg and Lerner 1982). This is due to the wave nature of light as described by the Huygens' principle. The angle of diffraction is inversely related the slit width and should therefore be take into consideration at narrow slit widths.
- When the glass plate containing the slit is fitted to the house of the dispersing PGP spectrograph it is important that the longitudinal direction of the slit is parallel to the horizontal plane of the front prism and the grating.

3.3.3 PGP element

The main purpose of the PrismGratingPrism (PGP) element is to spread the incident light from the narrow slit after it has passed the collimating lens system. The PGP-element consists two prism, a holographic transmission grating and blocking filters (Borregaard 1997; Hagman 1996; Herrala and Okkonen 1996; Spectral Imaging Ltd. 1997). By combining the refractive nature of the prisms with the diffraction nature of the holographic transmission grating it is possible to employ a direct sight (on-axis) (Spectral Imaging Ltd. 1997). The main principles will briefly be described.

3.3.3.1 The refractive nature of the prisms

A prism is a medium bounded by two-plane surface making an angle between the orthogonal of these surfaces. When light passes from one medium to another with a different optical density the light is refracted (see also section 3.2 page 13) (Alonso and Edward 1972a; Alonso and Edward 1972b). According to Snell's law the ratio between the sine of the incident and the sine of the angle of refraction is constant. This constant n_{12} is referred to as index of refraction (Alonso and Edward 1972a).

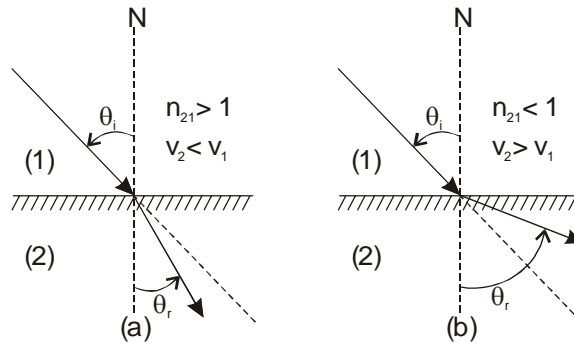


Figure 22: Refracted rays for $n_{12} > 1$ and $n_{21} < 1$. a) Light enters a media with a higher optical density resulting in a lower velocity of propagation of the wave $\Rightarrow v_2 < v_1$. b) Opposite case a. θ_i is angle of incidence; θ_r is angle of refraction; n_{12} is index of refraction (Alonso and Edward 1972a).

3.3.3.2 The disperse nature of the prism

When a wave is refracted into a disperse medium like a prism which index of refraction depends not only on the angle of incidence but also on the wavelength, the angle of refraction will also depend on the wavelength (Alonso and Edward 1972c).

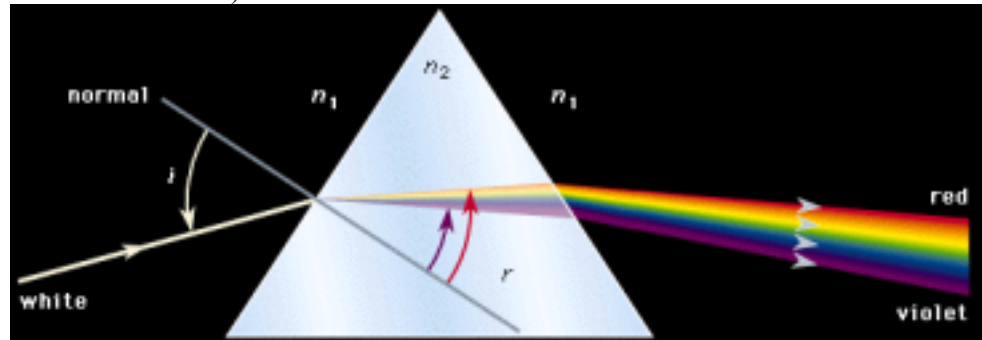
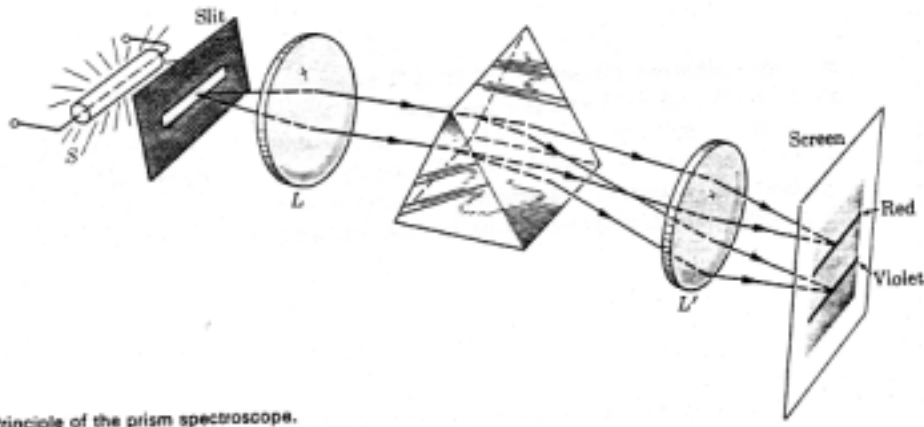


Figure 23: The principle of dispersion by use of a prism. The angles i and r that the rays make with the normal are the angles of incidence and refraction. Because n_2 depends upon wavelength, the incident white ray separates into its constituent colours upon refraction, with deviation of the red ray the least and the violet rays the most (www.britannica.com, 2000-01-21).

For this reason prisms can be used for analysing light in spectroscopes. A simple type of spectroscope is illustrated in Figure 24. Studying Figure 24 it becomes clear that the principle is the same as for the dispersing PGP spectrograph (Alonso and Edward 1972c).



Principle of the prism spectroscopy.

Figure 24: Principle of the prism spectroscopy (Alonso and Edward 1972c).

However the magnitude of the wavelength dispersion from a single prism is limited and several prisms are therefore needed to obtain a good dispersion. The two prisms in the PGP-element therefore also represent a spectrograph. However the prime function of the prisms is related to the angle of the light beam and not to the dispersion of light. The spectral dispersion is mainly performed by the holographic transmission grating explained in the next section (Herrala and Voutilainen 1994).

3.3.3.3 Principles of diffraction transmission gratings

Diffraction is noticeable when an obstacle, which has dimensions comparable to the wavelength of the wave, distorts a wave. The obstacle may be a screen with a small opening or a slit, which allows only a small portion of the incident light to pass. A diffraction grating is produced by placing several parallel slit of equal width b and equally spaced at a distance a . If the number of slits is large, the pattern will consist of a series of narrow bright fringes corresponding to the main maximum of the interference pattern which for normal incidence is given by $a \cdot \sin(\theta) = n \cdot \lambda$ where θ is angle of incidence and n is order of diffraction (Alonso and Edward 1972c). This is illustrated in Figure 25.

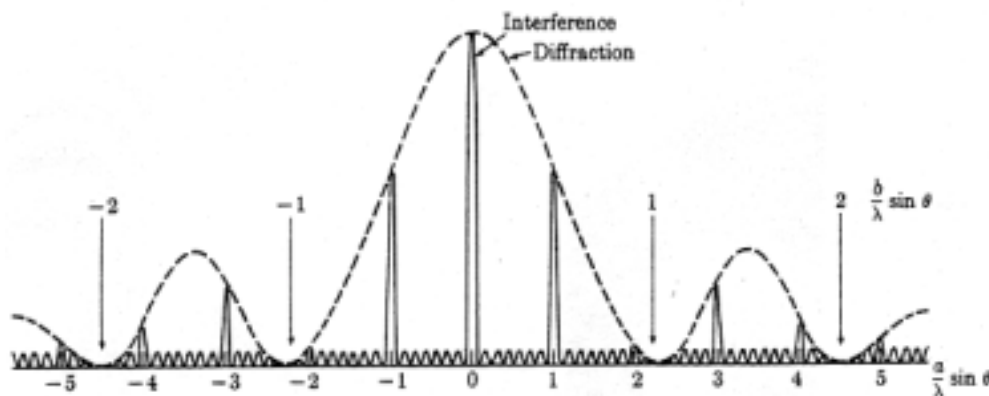


Figure 25: Intensity distribution produced by a diffraction grating on a plan normal to the incident light and parallel to the grating (Alonso and Edward 1972c).

When light of several wavelength falls on a grating, the different wavelengths produce diffraction maxima at different angles, except the zero order, which is the same for all. The set of maxima of a given order for all wavelengths

constitute a spectrum of first, second, third, etc., orders. Note that the longer the wavelength, the larger the deviation for a given order of spectrum. Therefore the red is deviated more than the violet, which is the opposite of what happens when a prism disperses light (Alonso and Edward 1972a).

Diffraction gratings have several distinct advantages over prisms. One advantage is that diffraction grating does not depend on the dispersive properties of the material, but only on the geometry of the grating (Alonso and Edward 1972a). Furthermore the spectrum from gratings are nearly linear (Esko Herrala, Specim, *pers. Comm.* 2002). However some material have superior characteristics compared to other when producing transmission gratings. The PGP element uses a holographically produced transmission grating manufactured on DCG (Dichromated Gelatin) between two protective glass plates. Due to its superior characteristics this material is commonly used to produce holographic optical elements (HOE's). The DCG has the following characteristics (Dickson et al. 1994; Hyvarinen et al. 1998; Spectral Imaging Ltd. 1997):

- High diffraction efficiency, usually between 40-70 % and theoretically reaching nearly 100% at a narrow spectral band under Bragg condition. The diffraction efficiency is practically independent of polarisation (Hyvarinen et al. 1998)
- Low scattering minimised stray light
- No ghost lines
- Low unwanted diffraction orders

The total throughput is determined by the grating diffraction efficiency and the transmission of other optical components. The latter is mainly determined in the 400-2000 nm range by surface reflectance that can be reduced with a multi-layer anti-reflection coating to about 0.5% in 400-700 nm and to 0.5-1% in 400-1000 nm (Hyvarinen et al. 1998).

By using a transmission grating it is therefore possible to construct a spectroscope as illustrated in Figure 26 and then it is possible to analyse the composition of light according to the telescope angle θ .

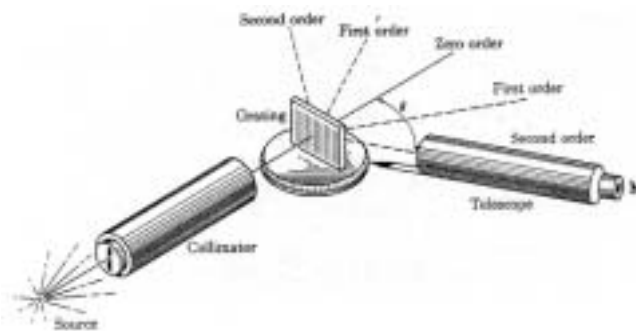


Figure 26: Grating spectroscope. The source is placed in front of the slit on the collimator. The diffraction grating is placed perpendicular to the collimator's axis and the spectra of different orders are investigated by the telescope (Alonso and Edward 1972a).

However, when a spectrograph is based on a transmission diffraction grating where the different wavelengths are diffracted to angle θ according to the grating equation: $n\lambda = a(\sin i + \sin \theta)$, where n is the diffraction order ($0, \pm 1, \pm 2, \dots$), λ is the wavelength, a is the groove spacing and i is the incoming angle to grating (Alonso and Edward 1972a; Herrala and Voutilainen 1994; Spectral

Imaging Ltd. 1999c). It can be seen that there is more than one wavelength that satisfy this equation for a particular set of values. This means that there are overlapping orders of spectra, which go to the same place (Herrala and Voutilainen 1994; Spectral Imaging Ltd. 1999c). Assume a spectrograph is designed so that it produces the first order ($n=1$) spectrum in range of 430-900nm across a detector surface. It can be seen that the second order ($n=2$) spectrum in the range of 430-450nm is now diffracted to the same angle range as the first order spectrum in the range of 860-900nm. The superposition would lead to ambiguous spectroscopic data if suitable filtering is not applied preventing the overlapping situation. The spectral overlapping can be avoided by placing an order blocking filter (OBF) at or close to the detector. An OBF solving the latter problem by having 50% of the detector surface coated to block wavelengths below 550 nm and transmit wavelengths in the band of 550-1000 nm as illustrated in Figure 27 (Spectral Imaging Ltd. 1999c).

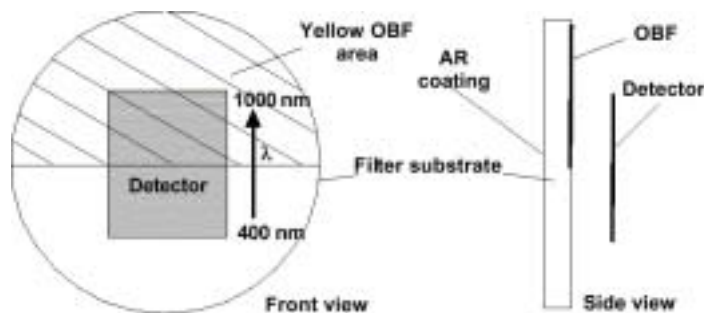


Figure 27: Installation of an order blocking filter (OBF) (Spectral Imaging Ltd. 1999c).

A disadvantage of a grating spectroscope not utilising the benefits of the PGP principles is its off-axis construction resulting in geometrical aberrations like astigmatism, which results in reduced image quality (Spectral Imaging Ltd. 1997). Further a curved detection plane is needed which is complicated to build compared to conventional plane CCD-arrays.

3.3.3.4 Putting together the Prism-Grating-Prism element

The problems mentioned above with prism and grating spectrographs can be solved using an axial transmission spectrograph that combines the qualities of the prism and the grating principles. This is done in the PGP-element by composing a specially designed volume transmission plane grating made of dichromated gelatin (DCG) and cemented between two symmetrical or nearly symmetrical prisms (Hagman 1996; Herrala and Okkonen 1996). PGP principle almost eliminates polarisation dependence that is still a problem in 90-degree (L-shaped) transmission spectrographs like the Axial Transmissive $f/1.8$ Imaging Raman Spectrograph described by Battey *et al.* (1993) and Hyvarinen *et al.* (1998).

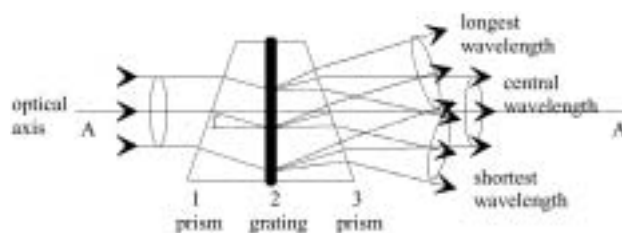


Figure 28: Basic principle of the direct-vision PGP-element (Herrala *et al.* 1994a; Herrala and Voutilainen 1994; Spectral Imaging Ltd. 1997).

After the light beam from the slit has passed the collimating lens it is dispersed at the PGP-element so that the central wavelength passes symmetrically through the grating and prisms (so that it stays at the optical axis) and the shorter and longer wavelengths are dispersed downward and upward relative to the central wavelength as illustrated in Figure 28. The latter construction results in a minimum deviation from the ideal on-axis condition and minimises geometrical aberrations both in the spatial and spectral axis. This makes a significant advantage when used in an imaging spectrograph (Herrala et al. 1994a; Herrala and Voutilainen 1994; Spectral Imaging Ltd. 1997).

3.3.3.5 Housing

Mechanically the all parts in the dispersing PGP spectrograph is assembled into a single tube resulting in an rugged construction with no adjustable or moving parts inside (Herrala et al. 1994a; Spectral Imaging Ltd. 1997). In order to avoid higher order diffraction problems from stray light, light beyond the spectral range of the spectral range of the spectrograph, and or to flatten the spectral response a blocking filter is placed after the collimating lens as illustrated in Figure 21 on page 22 (Herrala and Okkonen 1996). The inside walls must be blackened in the full spectral range of the spectrograph minimising the reflections (Borreagaard 1997). Reflections between the surfaces of the components creating ghost images is minimised by placing baffles inside the tube lens as illustrated in Figure 21 page 22 (Herrala and Okkonen 1996).

The spectrograph tube can be (equipped with standard mounts at the ends if needed) used as such for OEM purposes or in a C-mount housing (Herrala and Voutilainen 1994; Hyvarinen et al. 1998).

3.3.4 Summary

The construction on the VTTVIS line imaging spectrograph combines the refractive principles of two symmetrical prisms with the diffractive principles of a holographic transmission grating obtaining an on-axis system minimising geometrical aberrations. The system is well adapted to rough environments like e.g. outdoor conditions since all parts is assembled into a single tube resulting in an rugged construction with no adjustable or moving parts inside.

When selecting the optimal pixel resolution of the CCD it important take the potential loss of resolution into consideration due to chromatic aberration by the first collimating lens.

3.4 The camera unit – the sensing unit

After the light has passed the PGP element the reflected light from the measurant is projected in a rectangular plane consisting of a spatial and a spectral axis as illustrated in Figure 7 on page 12. This rectangular plane or imaging plane now needs to be quantified and converted into a digital signal interpretable by a computer. A digital camera unit is performing this task.

The heart of a digital camera is a array of Charge Coupled Devices (CCD). The overall principles are eloquently described by James Janesick and Tom Elliot of the Jet Propulsion Laboratory (Santa Barbara Instrument Group 1993a): “Imagine an array of buckets covering a field. After a rainstorm, the buckets are sent by conveyor belts to a metering station where the amount of water in each bucket is measured. Then a computer would take these data and display a picture of how much rain fell on each part of the field. In a CCD the

‘raindrops’ are photons, the ‘buckets’ the pixels, the ‘conveyor belts’ the CCD shift registers and the ‘metering system’ an on-chip amplifier”.

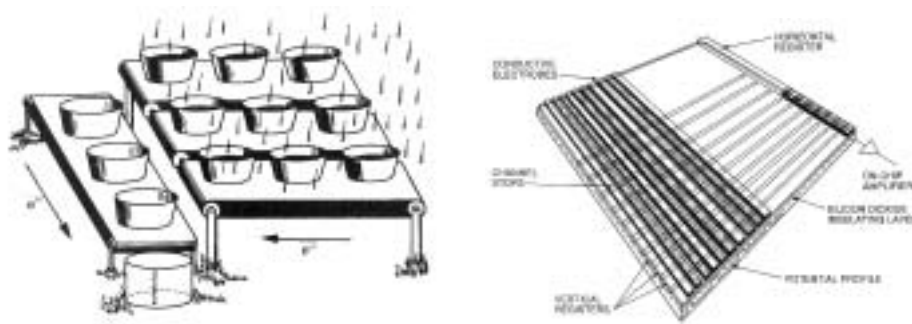


Figure 29: Left: Bucket analogy used to describe CCD operation. Right: Primary components that makes up a three-phase CCD (Janesick 2001).

The two main sources used to describe the important principles of a CCD and potential error sources is the book by Gerald C. Holst (1998): “CCD arrays Cameras and Displays – second edition” and a book by J.R. Janesick (2001): “Scientific Charge-Coupled Devices”.

3.4.1 The CCD array in brief

The CCD architecture has three basic functions: (1) charge collection, (2) charge transfer, and (3) the conversion of charge into a measurable voltage. The basic building block is the metal-insulator-semiconductor (MIS) capacitor also called a gate. The most important MIS is the metal-oxide-semiconductor (MOS) build of the oxide of silicon.

Applying a positive charge to a gate causes the mobile positive holes in a p-type silicon to migrate towards the ground electrode. This region, which is void of positive charge, is the depletion region. If a photon whose energy is greater than the energy gap is absorbed in the depletion region, it produces a electron-hole pair. The amount of negative charge (electrons) that can be collected is proportional to the applied voltage, oxide thickness, and gate area (Holst 1998).

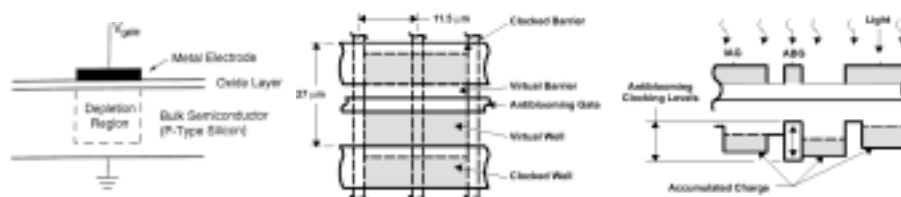


Figure 30: Left: Metal-oxide-semiconductor (MOS) gate for p-type silicon (Holst 1998). Right: Cross section of a potential well diagram for a pixel placed in a CCD model TC241 from Texas Instrument used in the digital camera ST-6 from SBIG (Texas Instruments 1991).

The total number of electrons that can be stored is called the well capacity (Holst 1998). The wells or pixels will spill into neighbouring pixels when the channel potential maximum of the collecting phase equals that of the adjacent barrier phase. This phenomenon is referred to as blooming. Due to channel stops separating the pixels columns (pictured as conveyers) is at a much lower potential than the within column barrier phases, blooming charge only spills into neighbouring pixels within the pixel column (Janesick 2001). Antibloom

integration cycle, charge is transferred quickly from the light sensitive pixels to the storage area. The FT imager may have a few dummy charge wells between the active and the storage area (Holst 1998).

The sense node or detection node can be a buffered amplifier converting the charge from the pixels into a video signal. Figure 32 shows the circuit diagram of a charge-detection node and one of three amplifiers. As charge is transferred into the detection node, the potential of this node changes in proportion to the amount of signal received. This change is sensed by an MOS transistor and after proper buffering the signal is supplied to the output terminal of the image sensor. After the potential change has been sensed, the node is reset to a reference voltage supplied by an on-chip reference generator (Texas Instruments 1991). The accumulated amount of light for each pixel is delivered in a sequential way to the output terminal of the CCD as a voltage. This analog signal is then further amplified into a measurable voltage and delivered to an analog-to-digital converter (ADC) (Holst 1998). The ADC is the final step quantifying and translating the light received by the single pixels into digital units, which can be handled by a computer.

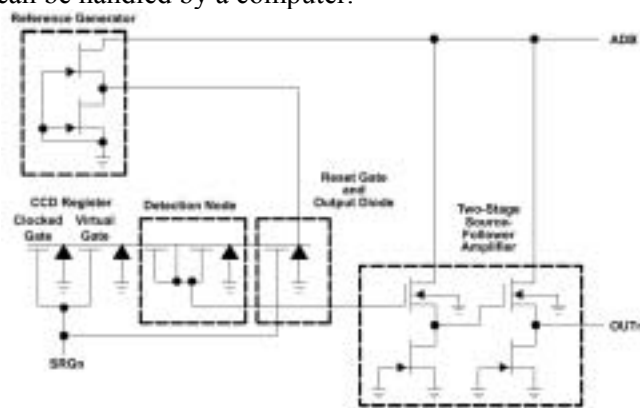


Figure 32: Buffer amplifier and charge-detection node in the CCD TC241 used in the SBIG ST-6 CCD camera (Texas Instruments 1991).

3.4.2 Noise sources

There are numerous noise sources, which must be taken into consideration working with CCD image devices. This area is huge and there are many books and articles on this subject. In this section only the most important noise sources will be presented briefly.

3.4.2.1 Shot noise

Shot noise is due to the discrete nature of electrons. It occurs when photoelectrons are created and when dark current electrons are present in the detector area. Further noise is added when the pixel charge is transported to the sense node capacitor due to charge transfer efficiencies lower than 1. Additional noise is added when reading the charge (reset noise) and introduced by the amplifier (1/f noise and white noise). When the output is digitised, inclusion of quantification noise may be necessary. The different noise sources and their location are shown in Figure 33.

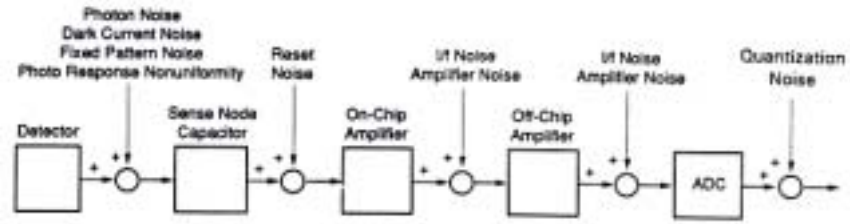


Figure 33: The various subsystems are considered as ideal elements with the noise introduced at appropriate locations (Holst 1998).

Although the origin of noise sources are different, they all appear as variations in the image intensity (Holst 1998).

3.4.2.2 Photon noise

Photon shot noise produces a temporal variation in the output signal that is proportional to the square root of the signal level in electrons (Holst 1998).

When the physical signal that we observe is based upon light, then the quantum nature of light plays a significant role. A single photon at $\lambda = 500$ nm carries an energy of $E = hc/\lambda = 3.97 \times 10^{-19}$ Joules. Modern CCD cameras are sensitive enough to be able to count individual photons. The noise problem arises from the fundamentally statistical nature of photon production. We cannot assume that, in a given pixel for two consecutive but independent observation intervals of length T , the same number of photons will be counted. Photon production is governed by the laws of quantum physics which restrict us to talking about an average number of photons within a given observation window. The probability distribution for p photons in an observation window of length T seconds is known to be Poisson:

$$P(p | \rho, T) = \frac{(\rho T)^p e^{-\rho T}}{p!}$$

Equation 2: The probability distribution for p photons in an observation window of length T seconds. ρ is the rate or intensity parameter measured in photons per second.

It is critical to understand that even if there were no other noise sources in the imaging chain, the statistical fluctuations associated with photon counting over a finite time interval T would still lead to a finite signal-to-noise ratio (SNR). The average value and the standard deviation are given by ρT and $\sqrt{\rho T}$, respectively. SNR for photon noise is therefore $10\log_{10}(\rho T)$ dB.

The three traditional assumptions about the relationship between signal and noise do not hold for photon noise:

1. Photon noise is not independent of the signal
2. Photon noise is not Gaussian
3. Photon noise is not additive

For very bright signals, where ρT exceeds 10^5 , the noise fluctuations due to photon statistics can be ignored if the sensor has a sufficiently high saturation level (<http://www.ph.tn.tudelft.nl/Courses/FIP/noframes/fip-Photon.html>).

3.4.2.3 Charge Transfer Efficiency (CTE)

As a charge packet in a pixel moves from storage site to storage site a few electrons are left behind. The ability to transfer all the charge is given by the Charge Transfer Efficiency (CTE). A fraction of the charge, as specified by the

charge inefficiency, is left behind. After the first transfer a fraction similar to CTE (ϵ) remains in the leading well and a fraction $(1-\epsilon)$ enters first trailing well. After the second transfer, the leading well transfer ϵ of the previous transfer and loses $(1-\epsilon)$ to the trailing well. The trailing well gains the loss from the first well and adds it to the charge transferred into the trailing well in the last go-around. During this process charge is not lost, just rearranged smearing the image (Holst 1998). It can be argued that CTE is not noise but bias depending of the CCD architecture and the measured image. However since CTE is not a constant value but depends upon the charge packet size it can be considered a noise source. For very low charge packets, the CTE decreases due to surface state interactions. This is particularly bothersome when the signal-to-noise ratio is low and the array is very large. CTE also decreases near saturation due to charge spill effects. Today CTE for consumer applications typically is greater than 0.9999 (Holst 1998).

3.4.2.4 Dark current noise

Dark current noise is thermally generated electrons in the CCD device itself. All CCDs have dark current, which can cause each pixel to fill with electrons in only a few seconds at room temperature even in absence of light (Santa Barbara Instrument Group 1993a). The CCD output is proportional to the exposure and increasing the integration time can therefore increase the output. However this approach is ultimately limited by dark current leakage that is integrated along with the photocurrent. A critical design parameter is dark current noise reduction. There are three main source of dark current: (1) thermal generation in the depletion region, (2) thermal generation and diffusion in the neutral bulk material, and (3) thermal generation due to CCD surface states (Holst 1998). In principle, dark current density can be made negligible with sufficient cooling. The dark current density decrease approx. twofold for every 8 to 9 °C drop in the CCD array from ambient (Holst 1998; Santa Barbara Instrument Group 1993a). The most common cooler is a thermoelectric cooler (TEC) which is a Peltier device driven by electronic current that pumps heat from the CCD to a heat sink (Holst 1998). For example the TEC at the SBIG ST-6 camera is capable of cooling the CCD down to -15 °C reducing the dark current density approx. 20 times if the ambient temperature is 20 °C. Because the temperature is in the exponent for the thermal generation in the depletion region small changes at in the CCD temperature say 1 °C can change the dark current significantly, 10% or more (Holst 1998).

3.4.2.5 Pattern noise

Pattern noise refers to any spatial pattern that does not change significantly from frame-to-frame. Dark current varies from pixel-to-pixel and this variation is called fixed pattern noise (FPN). FPN is due to differences in detector size, doping density, and foreign matter getting trapped during fabrication. Photoresponse nonuniformity (PRNU) is the variation in pixel responsivity and it is seen when the device is illuminated. The noise is due to differences in detector size, spectral response, and thickness in coatings. These “noises” is not noises in the usual sense. Frame averaging will reduce all the noise sources except FPN and PRNU. Although FPN and PRNU are different they are sometimes collectively called scene noise, pixel noise, pixels nonuniformity, or simply pattern noise. Because dark current becomes negligible by efficiently cooling the array, PRNU is normally the dominant pattern noise component (Holst 1998). When manufactures refer to PRNU by itself, it is generally refers to the low-frequency type of PRNU, which is a gradient of slower variation in

the responsiveness measured from one side of the array to the other (high-frequency PRNU is the variation in the responsivity between adjacent pixels). With this measure, adjacent pixels may actually show high uniformity, their output matches to within 0.1%. More widely separated pixels may be very different from each other, though. That is, as you go from one edge of the chip to the other, responsiveness may change by as much as 10%. This could show up in form of a gradient across the chip or perhaps as a ripple pattern. PRNU should for a flat field of uniform illumination ideally be 0% but is typically on the order $\pm 10\%$. PRNU can be highly dependent on illumination frequency as shown in Figure 34. The degree of PRNU generally increases as wavelength increases, so that red and NIR lighting produce more PRNU than blue and green wavelengths. This is due in part to the deeper penetration at the redder end of the spectrum (Burke 1996).

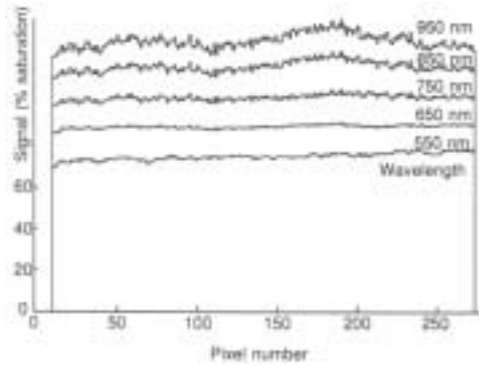


Figure 34: Variation in PRNU with wavelength (Burke 1996).

3.4.2.6 Flat fielding

The Signal-to-Noise ratio (SNR) for low contrast scenes is limited by pixel nonuniformity over most of the dynamic range of the CCD. Fortunately, the excellent linear characteristics exhibited by the CCD permit simple computer process that adjusts sensitivity easily and accurately. “Flat fielding” is a technique extensively used in scientific CCD application, a computer process that adjusts the sensitivity of each pixel to the same level. The algorithm is given in Equation 3 (Janesick 2001):

$$S_i = \mu_{scene} \frac{b_i}{a_i}$$

Equation 3: Flat fielding algorithm to adjust the sensitivity of each pixel in a CCD array to the same level. Dark current has been subtracted according to exposure before flat fielding. S_i is the value of the corrected i^{th} pixel, μ_{scene} is the average signal level of the scene, b_i is the value the data i^{th} pixel and a_i is the value of the i^{th} flat-field calibration pixel (Janesick 2001).

When performing flat-fielding the flattened image will contain additional shot noise from the calibration frame, thereby degrading SNR performance. By average several calibration frames this noise contribution can be minimised. Optimal flat fields are taken immediately after raw CCD images have been collected. It is important that these frames are collected under identical conditions or remnant fixed pattern noise will be in the processed image. This includes using the same camera gain, optical setup (e.g. filters), CCD operating temperature and clock voltage (Janesick 2001).

Dealing with PRNU in PGP image systems where the vertical axis is spectral the flat fielding approach becomes rather complicated. Besides the causes mentioned in the previous section, spectral interference in narrowband systems ($< 10\text{nm}$) is an additional form of fixed-pattern noise creating fringing patterns. Fringing is a problem due to multiple reflections within the gates and other topside layers. An example of this is given in Figure 35 (Janesick 2001).

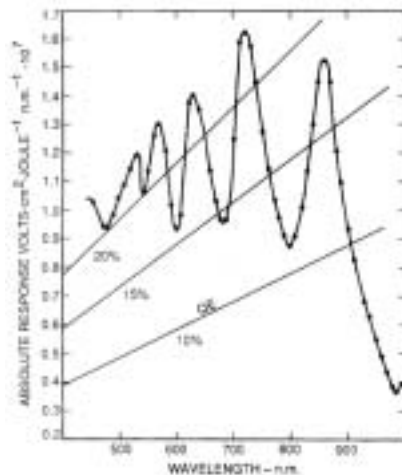


Figure 35: Narrow band Quantum Efficiency (QE) response for a single pixel as a function of wavelength (Janesick 2001).

The spectral lines are not straight within the image plane from a PGP spectrograph but are bended as described later in this report. When taking the spectral interference and the spectral bending into consideration the flat-fielding procedure becomes rather complicated. For further details please see section 5 “Adjustment and calibration procedure” on page 69.

3.4.2.7 Reset noise

Reset noise is generated by the periodic resetting of the sense node by the reset Metal-Oxide-Semiconductor Field-Effect-Transistor (MOSFET). Therefore, the reference level is different from pixel to pixel. The noise induced on the sense node is caused by thermal noise generated by the channel resistance of the reset transistor (Janesick 2001). This noise associated with resetting the sense node capacitor is often called kTC noise. Cooling of the CCD can reduce the reset noise by \sqrt{T} but is primarily used to reduce the dark current. Correlated Double Sampling (CDS) is the primary way of reducing the kTC noise significantly. CDS removes the uncertainty in the amount of charge remaining on the capacitor between the pixel charge packets being read. The CDS operation principles are shown in Figure 36. CDS also reduces amplifier 1/f noise (Holst 1998) discussed below. The SBIG ST-6 digital camera is an example of a system capable of using CDS (Santa Barbara Instrument Group 1993a).

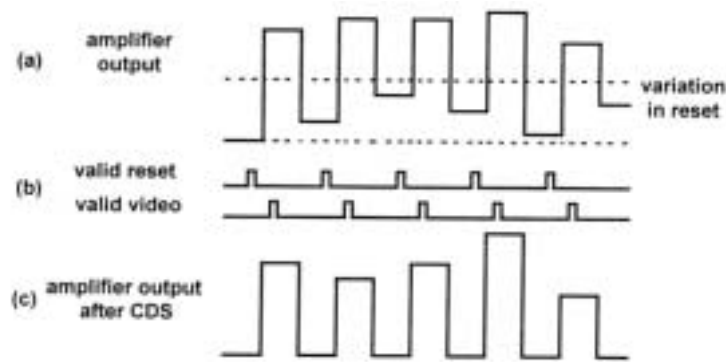


Figure 36: Correlated double sampling. (a) Amplifier output signal before CDS, (b) timing to measure video and reset levels, and (c) the difference between the video and reset levels after CDS. The dashed lines indicate the variation in the reset levels (Holst 1998).

3.4.2.8 Amplifier noise

When amplifying the signals on-chip and/or off-chip two amplifier noise components is introduced: $1/f$ noise (flicker noise) and white noise. Flicker noise originates in the MOSFET and will ultimately limit the CCDs read noise floor. Note that flicker noise decreases by a factor 3.16 for each decade increase in the amplifier frequency and falls at this rate until the second noise component the white noise floor is encountered. Thermal or white noise also known as resistor noise has several origins and is temperature dependent by \sqrt{T} (Janesick 2001). The CDS sampling technique also reduces white noise. With assumption that the noise of the second sample was uncharged from the instant of the first sample, the noise amplitudes are the same and are correlated in time. Therefore, the noise can be reduced by the CDS function (Baier 2001).

3.4.2.9 Quantification noise

Quantification noise is when the analog-to-digital converter produces discrete output levels. This means that a range of analog inputs can produce the same digital output. This uncertainty produces an efficient noise given by Equation 4 (Holst 1998).

$$n_{ADC_noise} = \frac{n_{well}}{2^N \cdot \sqrt{12}}$$

Equation 4: Quantification noise expressed in electrons (n_{ADC_noise}), $n_{well} \sim$ charge well capacity, $N \sim$ number bits for the ADC (Holst 1998; Janesick 2001).

Ideally the quantification noise is less than the noise floor and is achieved by selecting a high resolution ADC (high N).

3.4.2.10 Noise reduction by use of dark frames

No matter how much care is taken to reduce all sources of unwanted noise, some will remain. Fortunately, however, due to the nature of electronic imaging and the use of computers for storing and manipulating data, this remaining noise can be drastically reduce by subtraction of a dark frame from the raw light image. A dark frame is simply an image taken at exactly the same temperature and for the same duration as the light frame with the source of light to the CCD

blocked so that a “picture” of the dark is recorded. This dark frame will contain in image of the noise caused by dark current and other fixed pattern noise such as read out noise (Santa Barbara Instrument Group 1993a). However PRNU will not be removed by this dark current subtraction using a CCD to quantify the hyperspectral image from a PGP spectrograph.

3.4.2.11 Photon transfer

The photon transfer technique has proven to be one of the most valuable CCD transfer curves for calibrating, characterising, and optimising performance. The photon transfer method is used to evaluate numerous CCD parameters in absolute terms. These parameters include read noise, dark current, quantum yield, full well, linearity, PRNU, sensitivity, SNR, offset, and dynamic range. In addition, photon transfer is usually the first test performed in determining the overall health of a new CCD camera system. Well-behaved photon transfer data imply that a camera system is capable of taking precise measurements (e.g., absolute measurement errors typically less than 1% can be achieved). Also when camera problems do exist, photon transfer is usually the first diagnostic test tool called upon to identify subtle problems such as nonlinearity and noise issues like e.g. PRNU. Photon transfer also gives—almost magically—the conversion constant used to convert relative digital numbers (DN) generated by the camera into absolute physical units of electrons. This very important conversion constant is referred to as the “camera gain constant”, expressed in e^-/DN (Janesick 2001).

Although various noise sources exist, for many applications it is sufficient to consider photon noise, noise floor, and PRNU. Either the residual mean square (rms) or the noise variance can be plotted as a function of the signal level. The graphs are called the photon transfer curve and the mean-variance curve, respectively (Holst 1998).

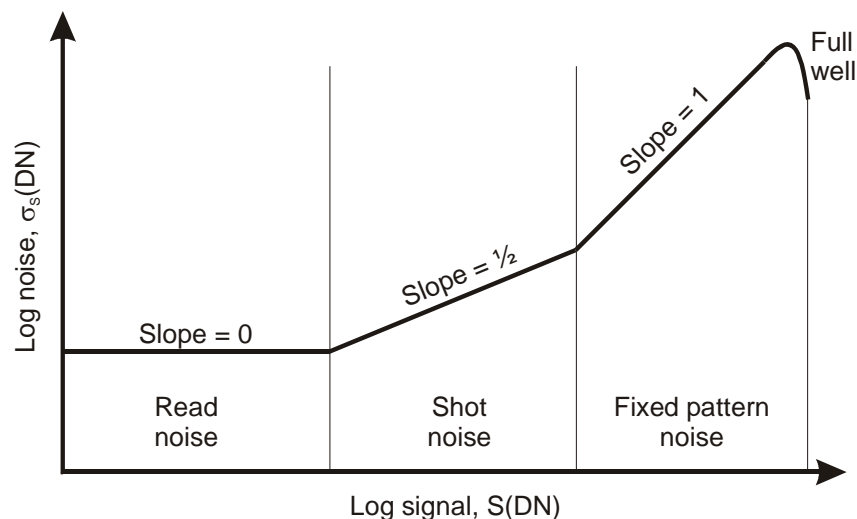


Figure 37: Total noise photon transfer curve illustrating the three noise regimes over the dynamic range of the CCD (after Janesick (2001)).

The photon transfer curve illustrated Figure 37 is a response from a CCD that is uniformly illuminated at different levels of light. The noise or standard deviation, $\sigma_s(\text{DN})$, is plotted as a function of the average signal, $S(\text{DN})$, for a group of pixels in the CCD array. Data is plotted in log-log scale in order to cover the large dynamic range of the CCD. Three distinct noise regimes are identified in the plot. The first regime is the read noise floor representing the random dark current noise. As the illumination to the CCD increase the noise

becomes dominated by shot noise of the signal mainly due to photon noise, shown in the middle region of the curve. Since the plot shown is on log coordinates, the shot noise is characterised by a line of slope $\frac{1}{2}$. The specific slope arises because the uncertainty in the quantity charge collected in any given pixel is proportional to the square root of the number of incident photons as mentioned earlier. The third regime is associated with PRNU, which is proportional to the signal and consequently produces a characteristic slope of unity on the log-log plot. The onset of full well is observed at some illumination level within the FPN regime and is seen as a break in the slope of one. At this point the charge spread between pixels (i.e., blooming), smoothing and lowering the noise as seen in the plot (Holst 1998; Janesick 2001). It should be noted that as PRNU increase the width of the second regime with slope $\frac{1}{2}$ decrease as the third regime slope 1 shifts to the left. At significantly large PRNU values the second regime is suppressed and the curve will shift directly from the noise floor, slope 0, to the FPN regime slope 1 (Holst 1998).

3.4.2.12 Signal-to-Noise-Ratio (SNR)

Signal-to-noise ratio describes the quality of a measurement. In CCD imaging, SNR refers to the relative magnitude of the signal compared to the uncertainty in that signal on a per-pixel basis. Specifically, it is the ratio of the measured signal to the overall measured noise (frame-to-frame) at that pixel. High SNR is particularly important in low-contrast applications requiring precise light measurement. It is not uncommon in scientific application to ask the CCD to detect contrast levels less than 1%. In theory, any level of contrast can be seen by the CCD as long as pixel nonuniformity is removed and the charge capacity is high enough for the SNR required (Janesick 2001). When calculating overall SNR, all noise sources need to be taken into consideration. Normally SNR is calculated on array basis assuming that the spectral composition of light is common for all pixels. This is however not the question working with line imaging spectrographs. For line imaging spectrographs each horizontal row is exposed to different wavelengths and a column wise SNR measure is therefore more appropriate since for example the pixel responsiveness is wavelength depended. G. Polder and G.W.A.M van der Heiden (2001) have recently confirmed that SNR for an Inspector V7 spectrograph is wavelength dependent. They concluded that in the blue part of the spectrum the SNR was lower than in the green and red part of the spectrum. Further they concluded it was due to a decreased quantum efficiency of the CCD, a smaller transmission coefficient of the spectrograph, as well as poor performance of the illuminant.

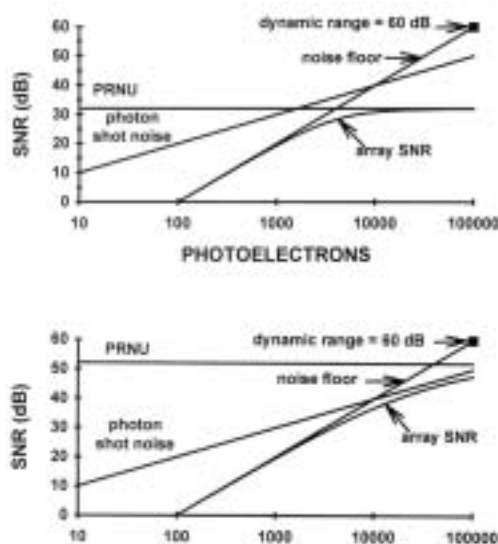


Figure 38: SNR as a function of noise for (top) photoreponse-nonuniformity = 2.5% and (bottom) photoreponse-nonuniformity = 0.25%. PRNU, photon noise, and the noise floor have slopes of 0, 10, 20, respectively. Dark current shot noise is considered negligible. Note a low SNR is bad and high SNR is good having a high contrast (Holst 1998).

Graphs can be used to illustrate SNR for the different noise sources as a function of their noise levels as shown in Figure 38. At low flux levels the SNR increases with the signal (noise floor is constant). At moderate levels, photon shot noise limits the SNR and at high levels, the SNR approaches $1/U$ ($U \sim$ photoreponse nonuniformity). SNR is often expressed as a power ratio (in dB), which is $20\log(\text{SNR})$. While the array may have a finite PRNU, it can be minimised through an appropriate algorithm (Holst 1998; Janesick 2001).

3.4.2.13 Pixel binning

Binning is the process of combining charge from adjacent pixels in a CCD during readout. This process is performed prior to digitisation in the on-chip circuitry of the CCD by specialized control of the serial and parallel registers. The two primary benefits of binning are improved SNR and the ability to increase frame rate, albeit at the expense of reduced spatial resolution. The SBIG ST-6 camera has the ability to perform binning into any arbitrary $M \times N$ binned pixels (super-pixels) through simple software control (Santa Barbara Instrument Group 1993a). Since both the serial register and summing well accumulate charge from multiple pixels during binning, they must have sufficient capacity to prevent saturation. However, the specifications of the particular CCD being used should be noted and understood before using the binning technique. This is especially true when working at high-illumination levels where saturation could lead to erroneous data collection.

The primary benefit of binning is higher SNR due to reduced read noise contributions. CCD read noise is added during each readout event and in normal operation, read noise will be added to each pixel. However, in binning mode, read noise is added to each super-pixel, which has the combined signal from multiple pixels. In the ideal case, this produces a SNR improvement equal to the binning factors. If this region is read out in normal mode the SNR will be 1:1, and the signal will be lost in the noise. However, with 2×2 binning, the SNR becomes 4:1, which is sufficient to observe this weak signal.

Unlike read noise, dark current noise is not reduced by binning since each pixel will contribute dark current noise to the super-pixel.

One of the most common applications of binning is spectroscopy. In spectroscopic CCD systems, the dispersed slit images lie along the CCD columns (perpendicular to the serial register) and the resulting images are then binned along the columns. Binning thus provides marked increases in SNR without any loss of spectral resolution. However spatial resolution is lost along the slit axis (http://www.roperscientific.com/ccd/library_encyclopedia.shtml).

3.4.2.14 Dynamic range

Dynamic range refers to intra-scene performance; that is, the ability to quantitatively detect very dim and very bright parts of a single image. Because the smallest measurable intensity varies between applications and experimental conditions, CCD manufacturers have adopted a definition for specifying dynamic range that is independent of how the camera is used. This definition is defined mathematically as: linear full well (electrons)/read noise (electrons), and is therefore a dimensionless number (http://www.roperscientific.com/ccd/library_encyclopedia.shtml).

Often the dynamic range is expressed in decibels: $20\log(\text{linear full well/read noise})$. Many manufactures list the dynamic range as signal-to-noise ratio. This value should not be confused with the actual SNR discussed earlier (Holst 1998).

3.4.2.15 Summary

As for the lenses a careful selection of a CCD camera with high quality components and design can reduce error sources like reset noise, amplifier noise, and $1/f$ noise significantly.

Cooling of the CCD reduces thermal induced fixed pattern noise (FPN) significantly, which is particular important to remove for low contrast signals and/or long exposures especially in the near infrared range of silicon based CCD arrays. Further at very low signal or charge packets the charge transfer efficiency decrease making it particularly bothersome when the SNR is low and the CCD array is large.

Cooling of the CCD cannot remove photoresponse nonuniformity (PRNU), which is normally the dominant pattern noise source. It is crucial to remove this noise source since the responsiveness of the pixels may change as much as 10% across the CCD. Taking the hyperspectral dependence of PRNU and the narrow band spectral interference into consideration correction is expected to become highly complicated of PGP based hyperspectral imaging systems. K.T. Hoheusle (2000) showed improved results within astronomical hyperspectral imaging after flat-field corrections confirming that hyperspectral flat-fielding can be expected to improve the quality of the data from the VTTVIS system. Later in this report image distortion in both the spatial and spectral direction caused by the PGP spectrograph complicates correction of systematic errors even more.

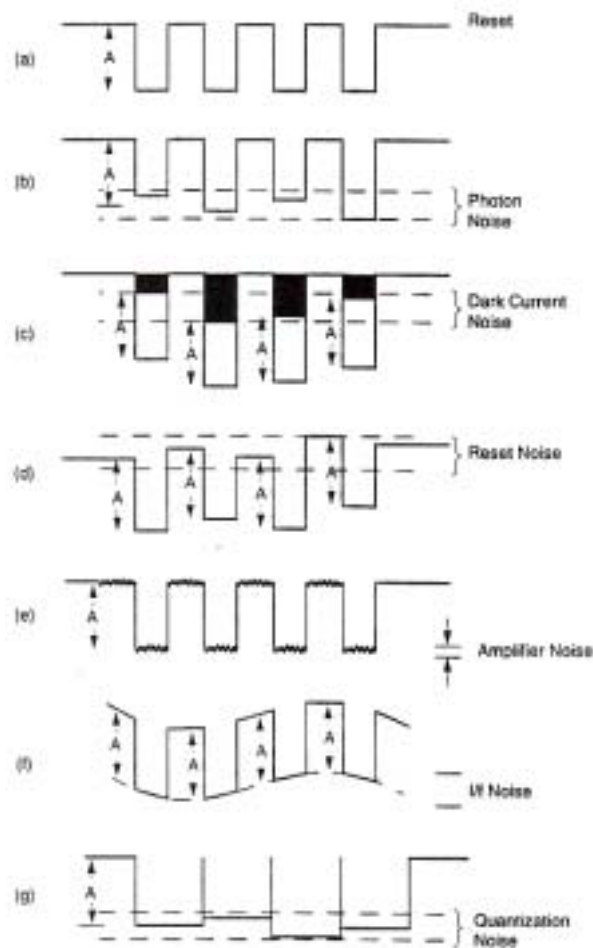


Figure 39: Noise sources affect the output differently. (a) through (f) represent the output after the on-chip amplifier, (g) is the output after the sample-and-hold circuitry. The array is viewing a uniform source that produces identical outputs (amplitude - A) for each pixel. (a) ideal output, (b) photon shot noise, (c), dark current shot noise, (d) reset noise, (e) amplifier noise, (f) amplifier $1/f$ noise, and (g) quantization noise. These values change from frame-to-frame. Pattern noise is not shown but is a variation that does not change significantly each frame. All these processes occur simultaneously (Holst 1998).

Photon noise is most cases the dominant noise source having minimised all other noise sources by proper camera selection and calibration. So even if there were no other noise sources in the image chain, the fundamentally statistical nature of photon production will lead to fluctuations in photon counting over a finite time interval leading to a finite SNR.

In Figure 39 in major CCD noise sources in illustrated and their effect on output signal.

3.5 Linearity of spectral range at the imaging plane

When a narrow beam of light has passed through the PGP-element it becomes dispersed according to wavelength as shown in Figure 21 page 22. Hereafter the triplet lenses focus the dispersed light at the CCD array with the shortest wavelength at the bottom at the longest at the top. To determine a specific

wavelength with the CCD array it is in literature commonly assumed that there is a linearly relationship between wavelength and the specific location at the CCD (Åstrand *et al.* 1996; Borregaard 1997; Herrala and Voutilainen 1994; Johansson 1998; Nielsen *et al.* 1999; Vaarala and Aikio 1997). However Braam *et al.* (1993) pointed out that this is not true. According to their results a two-piece linear model gave a significant better prediction of the wavelength location at the CCD array compared to a simple linear fit. A second order polynomial model was also tested but did not perform better than the two-piece linear fit as shown in Figure 40. Herrala *et al.* (1994a) showed a similar pattern in the spectral linearity of a PGP spectrograph in the visual range as Braam *et al.* (1993). Polder (2001) performed a spectral calibration of an Inspector V7 by using several spectral calibration sources and concluded 2nd order regression was performing the best.

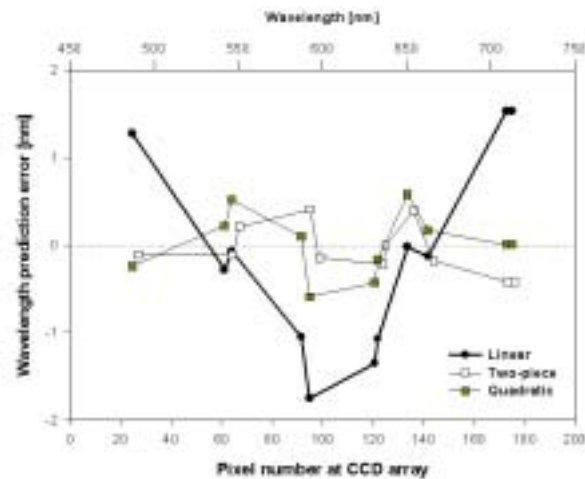


Figure 40: Wavelength prediction errors for different fitted model for an AISA PGP-spectrograph. The plot is based on Braam *et al.* (1993).

3.6 Bending of spectral lines at the imaging plane (smiling)

Several authors like Nielsen *et al.* (1999) or Åstrand *et al.* (1995) assume that the spectral wavelength location at the CCD array is independent of the spatial axis. However when light from different spatial location passes through the collimate triplet lens, the PGP-element, and the rear focusing triplet lens the spectral lines are bended also referred to as *smiling*. Vaarala *et al.* (1997) clearly showed the spectral bending for 3 three different wavelengths as illustrated in Figure 41.

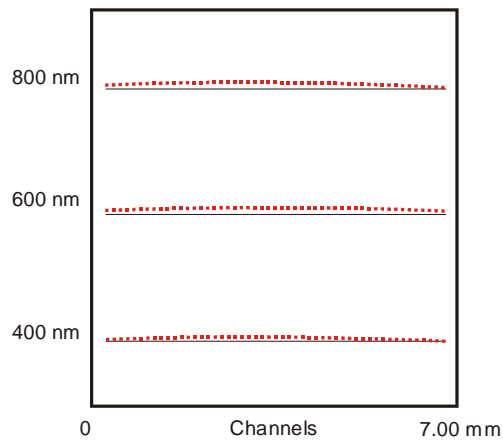


Figure 41: Bending of spectral lines for 400 nm, 600 nm, and 800 nm based on Vaarala et al. (1997).

This means that if the spectral calibration is performed at the vertical centre of the CCD array (the middle of the slit line) then all wavelengths at both endpoints of the slit will systematically be underestimated approx. 1-3 nm for all wavelengths. Polder and van der Heijden (2001) also concluded that due to aberrations in the grating the spectral lines are slightly bent across the spatial axis. In Polder and van der Heijden's case the bending was ± 1.3 nm at a wavelength 670 nm. Therefore they concluded the optimal spectral calibration procedure needed to be done separately for each spectral column across the spatial axis.

3.7 Distortion of the spatial axis

When doing spectral measurements with a linespectrometer like the PGP spectrograph it is normally assumed that the spectral response from a subarea i of an object line (see Figure 19 page 20) is projected vertically in a strait line at the CCD array. This assumption makes it possible to obtain the spectral composition from subarea i by extracting a vertical row(s) of pixels according the width of i as shown in Figure 3 on page 9 and Figure 6 on page 12. According to section 3.2.2.5 page 17 there will be neither distortion nor coma in a perfectly symmetrical system at magnification 1:1 and the latter assumptions will hold. The PGP spectrograph consists of a nearly symmetrical optical system with magnification 1:1 (Herrala and Voutilainen 1994). However studying Figure 42 it becomes clear that the holographic grating (HOE) in the PGP-element breaks the optical symmetry. In case of the central wavelength the front lens system collimating the light will cause a barrel distortion, which will be neutralised by the pincushion distortion in rear focussing lens system. For wavelengths different to the central wavelength the case is different. After the narrow line of light has passed the front lens there will be a maximal horizontal barrel distortion at both ends of the object line. Hereafter the HOE diffracts the light along the vertical axis. This diffraction of the barrel distortion object line cannot be neutralised totally in the spectral plane causing an increasing error in the spatial axis as the distance in the spectral plane increase from the horizontal position of the central wavelength. This is schematically illustrated in Figure 42 and is referred to as keystoneing.

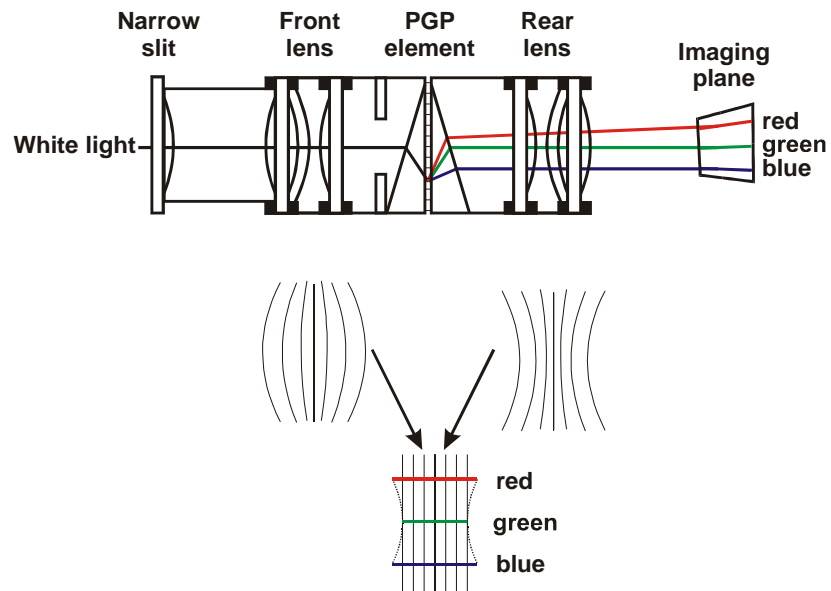


Figure 42: Schematic illustration of vertical bending along the spatial axis in a PGP spectrograph. Due to the wavelength separation caused by the grating in the PGP-element the optical system is not perfectly symmetric with a magnification 1:1. Therefore the optical system will not be totally free of distortion and coma.

The vertical bending along the spatial axis will cause a mixing of the spectral response between neighbouring sub areas from the object line. Under edge conditions like a leave edge next to a soil background this latter phenomena can produce reflectance spectra leading to erroneously interpretations if not foreseen.

3.7.1 A worst case study of the distortion of the spatial axis

Based on the ray tracing results for the VTTVIS it is possible to simulate the impact on the reflectance spectra at edge zones between for example leaf and soil areas depending on the horizontal distance from CCD array centre at 575 nm, which is the centre of symmetry for the imaging distortion. As previously mentioned the spatial distortion will cause a mixing of the spectral response between neighbouring sub areas. The extent of this mixing depend both degree of the spatial distortion for the used PGP spectrograph and on the resolution / pixel size of the CCD array used. In the example illustrated in Figure 43 the pixel size is assumed to be 27 μm wide. The simulated spectra is calculated by gradually mixing the measurerant pixel with the reflectance spectral from the area next to in the direction towards the CCD array centre based on the results from Equation 10 and the pre-set pixel width. The resulting equation is given in Equation 5.

Studying the effect of edge conditions on the reflectance it seems clear that this error source cannot be neglected. Due to the nature of the spatial distortion the effect is small in the range around 575 nm. However the effect becomes increasingly clear at 650 nm till 750 nm where the true spectra from object i is clearly mixed with the spectra from the neighbour area towards the CCD centre. The spectral area between 650 nm and 750 nm is commonly used for several indexes like red edge (chlorophyll content), Vegetation Index (VI), Normalised Difference Index (NDI), Soil Adjusted Vegetation Index (SAVI) etc. (Reusch 1997) and it is therefore important to minimise error sources within this range. According to Equation 5 the impact of the spatial bending is closely related to pixels width in the CCD. Therefore careful considerations should be done choosing camera resolution for the PGP spectrograph.

$$\begin{aligned}
R_{\text{mix}}(\lambda, H_{\text{pos}(575)}) &= R_i(\lambda) \cdot \frac{(w_p - \Delta H_{\text{pos}(575)}(\lambda_{\Delta 575}(\lambda), H_{\text{pos}(575)}))}{w_p} + R_n(\lambda) \cdot \left(1 - \frac{(w_p - \Delta H_{\text{pos}(575)}(\lambda_{\Delta 575}(\lambda), H_{\text{pos}(575)}))}{w_p}\right) \\
&= (R_i(\lambda) - R_n(\lambda)) \cdot \frac{(w_p - \Delta H_{\text{pos}(575)}(\lambda_{\Delta 575}(\lambda), H_{\text{pos}(575)}))}{w_p} + R_n(\lambda) \\
&= (R_i(\lambda) - R_n(\lambda)) \cdot \frac{(w_p - A \cdot \lambda_{\Delta 575}^2(\lambda) \cdot H_{\text{pos}(575)})}{w_p} + R_n(\lambda)
\end{aligned}$$

$R_i(\lambda)$:	[%]	True reflectance from the object area i
$R_n(\lambda)$:	[%]	True reflectance from the area next to object area i towards the vertical CCD centre
w_p :	[mm]	Width of 1 pixel at the CCD array defining the width of object area I
$\Delta H_{\text{pos}(575)}(\lambda_{\Delta 575}(\lambda), H_{\text{pos}(575)})$:	[mm]	Horizontal distance between the centre of area i at 575 nm and the actual location for a specific wavelength λ
$H_{\text{pos}(575)}$:	[mm]	Horizontal distance from position at 575 nm till the centre of the CCD array
$\lambda_{\Delta 575}(\lambda)$:	[nm]	Difference between the actual wavelength (λ) and 575 nm
A :	[]	Estimated constant based on ray tracing. For the VTTVIS spectrograph $A=1.5241419\text{E-}7$

Equation 5: $R_{\text{mix}}(\lambda, H_{\text{pos}(575)})$ simulates the systematic mixing of reflectance from neighbouring object points along the pixel columns depending on the horizontal distance from the centre of the CCD at 575 nm and on the specific wavelength.

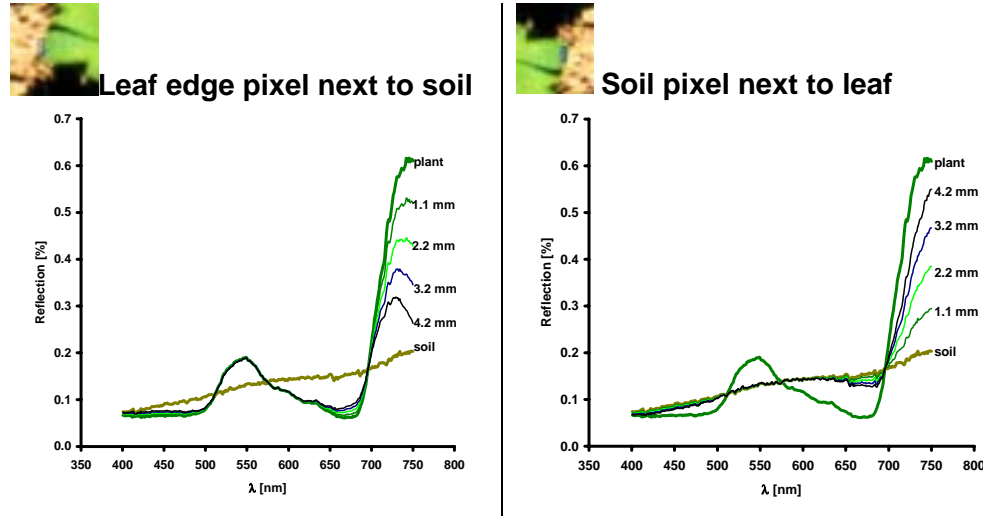


Figure 43: Simulated effect of edge conditions on the registered reflection spectra for the VTTVIS and the systematic measurement errors depending on the horizontal distance from the centre of the CCD caused by spatial distortion of the imaging plane. The actual pixel size is set to 27 μm wide and the extent of the spatial bending is simulated by used of Equation 10. The plant and soil reflectance spectra is measured far from edge condition zones and is assumed put next to each other visa-versa with pixel centre of measurerant pixel located 1.1, 2.2, 3.2, and 4.2 mm from the horizontal centre of the CCD array at 575 nm.

3.8 Distortion of the spectral axis

The principles concerning the distortion of spatial axis is similar for the distortion of the spectral axis. Assuming the object line of light passes the exact centre sagittal plane of the front lens in the PGP-element there will be no barrel distortion in the vertical direction. However after the object line of light is diffracted passing the HOE the light passes it is outside the centre sagittal plane except for the central wavelength (illustrated as green in Figure 44). Therefore pincushion distortion will have an impact on the spectral lines.

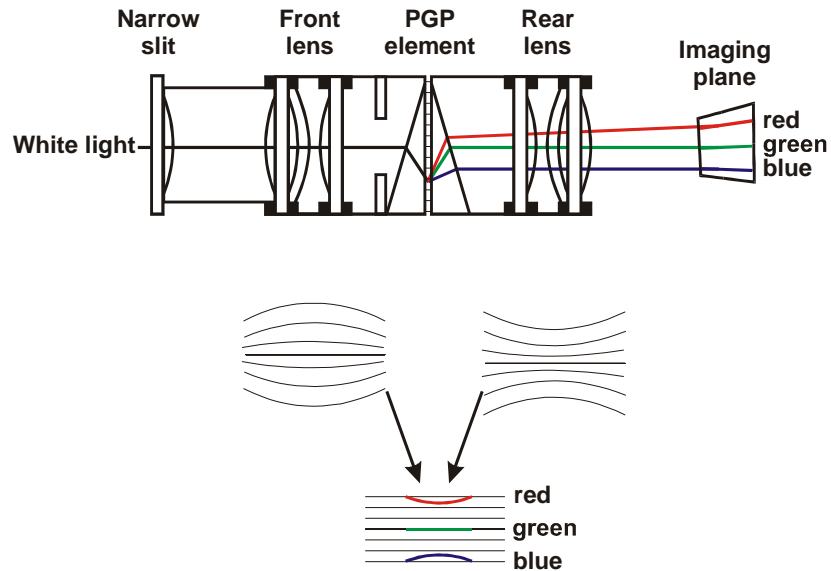


Figure 44: Schematic illustration of horizontal bending of the spectral lines in a PGP spectrograph. Due to the wavelength separation caused by the grating in the PGP-element the optical system is not perfectly symmetric with a magnification 1:1. Therefore the optical system will not be totally free of distortion and coma.

However, the distortion illustrated in Figure 44 does not fit when the bending or smiling of the spectral lines illustrated in Figure 41 on page 43. The reason for this difference is due to a change in entrance angle of the rays in the sagittal plane compared to an orthogonal entrance into the prism. This will increase the distance the rays from off axis object point must travel within the prism before reaching the grating. Consequently object points will enter the grating at a lower and lower point as the distance increasing from the slit centre. Further the change from the orthogonal entrance in the sagittal plane will cause an increasing dispersion as the distance increase from the slit centre. All together this causes the convex bending of the spectral lines. The refraction is highest for the short waved rays and the bending is therefore more noticeable for these compare to the long waved. The principles are briefly illustrated in Figure 45.

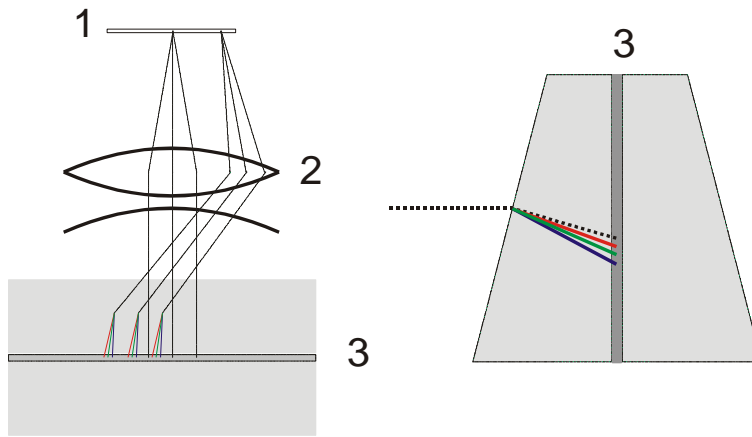


Figure 45: Illustration of the principles causing spectral bending. Left – scenario from above. Rays passing the slit (1) enters the spectrograph. The rays then pass the collimate lenses (2) and enters the PGP unit (3). The change in the entrance angle in the sagittal plane of the off axis rays causes dispersion. Right – scenario from the side. The dispersion and the change in angle causes an increase in the travelling distance for the off axis rays before reaching the grating, which results in spectral bending or smiling. The punctuated lines illustrate the rays from the object on the optical axis (~ the centre of the slit).

3.9 Assembling the camera unit to the PGP spectrograph

When assembling the camera unit to the PGP spectrograph proper adjustment can prevent several fatal error sources of which all are complicated to correct mathematical afterwards. In the following the origin of the different error sources and how to minimise these in connection with the assembling of the camera and the PGP spectrograph will be discussed. These error sources are displacement of the back focal length, rotation of the camera unit, and twisting of the camera unit at the assembling area.

3.9.1 Displacement of the back focal length

When mounting the camera unit to the PGP spectrograph it is important the paraxial focal plane is located exactly at the back focal distance of the PGP spectrograph (Polder and van der Heijden 2001). When this is not the case as illustrated in Figure 46 the picture gets blurred both in the spectral and spatial axis. The means that shape changes along the spectral axis caused by for example the Fraunhofer lines from the sun get smeared. In the spatial axis the latter also smears out the picture, which become most clear under edge conditions like between a leaf edge and a soil background. Adding the focal problems connected with performing measurements of a canopy as illustrated in Figure 19 page 20 proper adjustment of the back focal distance becomes even more crucial.

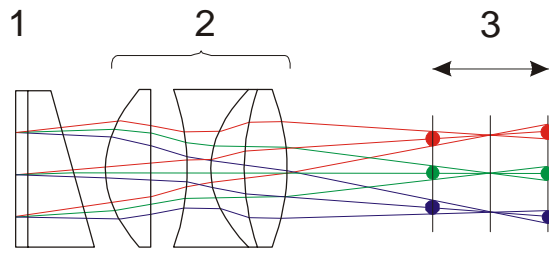


Figure 46: Schematic illustration of the effect to the focus on the paraxial plan caused by longitudinal displacement of the camera unit alias the CCD array. 1 ~ Grating and rear prism in the PGP; 2 ~ Focussing lens in the PGP; 3 ~ The vertical lines illustrates the longitudinal location of CCD array as it slides away from the true focal distance in the middle. The circles indicate the extent of the circle of confusion.

3.9.2 Rotation of the camera unit alias the CCD array

By studying Figure 47 it becomes clear that rotation of the CCD camera with rotation axis on the PGP system axis causes significant errors not only in the spectral registration on CCD array but also in the spatial axis. Due to the discrete nature of the CCD array it becomes very difficult to overcome the latter errors. Therefore to axis of the CCD array and the axis of the PGP spectrograph must be in line right from the beginning.

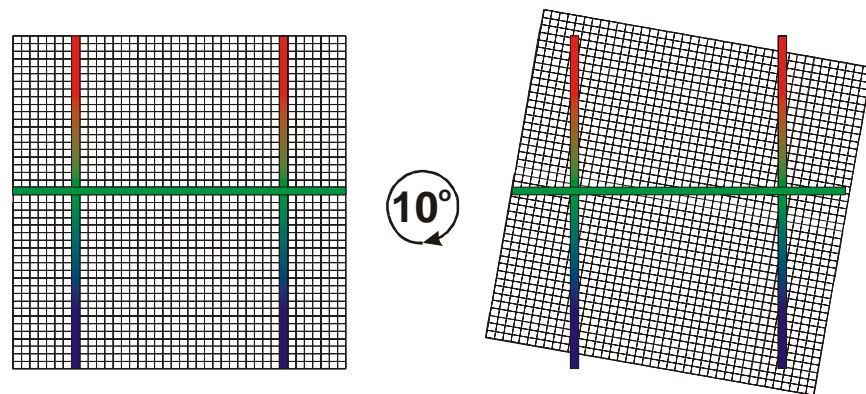


Figure 47: Schematic illustration of CCD camera rotated 10 degrees clockwise with rotation axis on the PGP spectrograph axis. The coloured bars illustrated PGP output axis and the empty squares the pixels of the CCD array in the camera unit.

3.9.3 Twisting of the camera at the assembling point of the VTTVIS

Twisting of the camera must be avoided. By studying Figure 48 it is clear that there is a risk of both spatial and spectral distortion. Both illustrations show “clear” cases but both situation can happen simultaneously. Furthermore, the CCD plane will not be in line with the focus plane smear the image. By proper adjustment this error source can be eliminated.

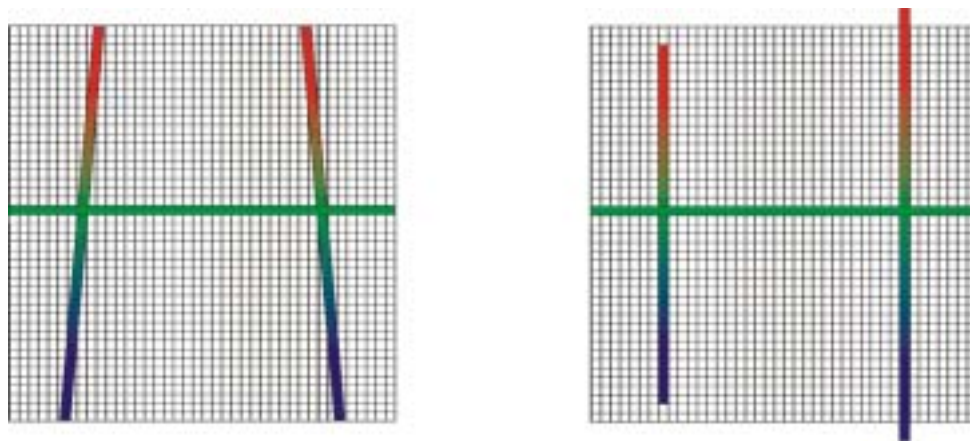


Figure 48: Schematic illustration of effect to the projected image from the PGP spectrograph onto the CCD array when twisting the camera mounting at the assembling point of the PGP spectrograph.

3.10 Summary and discussion

The principles and potential error sources using the VTTVIS line imaging spectrograph has been described and discussed briefly. It is clear the PGP-spectrograph is well adapted to rough environments since all parts are assembled into a single tube with no moving parts inside.

The system consists of three main units – the front lens, the PGP spectrograph, and camera. Within all units there are several error sources, which all add potential noise or bias to the hyperspectral image. Most of them can be removed or minimised by use of high quality parts. However using high-grade components cannot remove all error sources. The most serious error sources bending and keystoneing have been reduced $1/10^{\text{th}}$ in the Specims enhanced PGP spectrographs compared to the VTTVIS (Esko Herrala, *pers. comm.* 2002).

The varying focus depth measuring at a canopy creating smearing cannot be removed. The most efficient way to minimise the extent of this error is to increase the distance between the VTTVIS and the measurant.

The dominant error sources within a high-grade cooled CCD camera used with a hyperspectral line imaging spectrometer are photoresponse nonuniformity (PRNU) and photon noise.

PRNU is fixed pattern noise or more correctly bias which can be removed by performing hyperspectral flat-fielding. However due to image distortion in both the spectral and the spatial direction of the VTTVIS the estimation of the optimal correction model will be complex and time consuming. Thus after an appropriate correction model have been formulated and parameterised it crucial the VTTVIS can be assembled very accurate and precise obtaining exactly similar settings.

Having obtained the best possible setup of a line imaging spectrometer system photon noise can be expected to be the dominant noise source due to the fundamentally statistical nature of photon production leading to fluctuations in photon counting over a finite time interval.

The VTTVIS has a significant distortion of the spatial axis depending on wavelength and the distance from the slit centre. This bias has some severe consequences performing analysis on pixel basis especially at edge conditions. Knowing the horizontal location of the spatial object pixels projected on the CCD is wavelength dependence a model removing this image distortion ought to be developed prior to any analysis on object measurements.

Several papers and reports document the potential of using a line imaging spectrograph for soil/crop/weed classification or discrimination (Bennedsen et al. 2000; Bennedsen and Rasmussen 2001; Borregaard 1997; Borregaard et al. 2000; Feyaerts et al. 1999c; Feyaerts et al. 1999a; Feyaerts et al. 1999b; Feyaerts and Van Gool 2001; Nielsen et al. 2000; Pollet et al. 1999), nutrient diagnostics (Dumont and De Baerdemaeker 2001; Nielsen et al. 1999; Schut and Ketelaars 2001a), wood quality estimation (Hagman 1996), characterization of spatial heterogeneous canopies (Schut et al. 2000), Airborne imaging spectroscopy (Mäkisara and Tomppo 1996), and color characterisation (Ewing and Horton 1999; Johansson 1998; Stokman et al. 2000; van der Heijden et al. 2000). However, common for all of these publications are that they are not correcting for all the potential instrument errors mentioned in this chapter. The spectral non-linearity is corrected to some extent but the spatial image distortion is ignored. Many of the authors is averaging several pixels and thereby lowering the impact of the potential error. The authors have obtained still valuable information and knowledge useful to science. Due to the merge between instrument characteristics and measurant characteristics it will be difficult if not impossible to transfer the models and knowledge to new equipment. Thus instrumental characteristics and noise should be removed or minimised prior any analysis enabling knowledge transfer between systems.

4 Specifications of the line imaging spectrometer

The aim of this section is to give a detailed description of the equipment. The Department of Agricultural Sciences, AgroTechnology, KVL, Denmark, has been working with since 1995. This equipment consists of two line Imaging spectrometers one in the visible range (VIS) and one in the near infrared range (NIR), respectively (Borregaard 1997). These have been designed and manufactured by VTT, Finland, now commercialised by Spectral Imaging Ltd. (www.specim.fi) (Hyvarinen et al. 1998; Nielsen et al. 1999). However in this report only the VIS line imaging spectrometer (VTTVIS) will be described in details. Furthermore the measuring rig to which the VTTVIS is mounted will be described.

4.1 The front lens

The front lens used is a Schneider-Kreuznach Xenoplan 1.9/35 mm objective and the distance from the object plane to the lens should be within 1 to 2 meter (Borregaard 1997; Herrala and Voutilainen 1994). Schneider Optics, Inc. gives the following outline concerning the lens (<http://www.schneideroptics.com/cctv/cctv3/cctv3.htm>, 2000-01-31):

The 2/3" C-Mount lenses are designed for a spectral range of 400-1000 nm and can be used in the visible and near infrared range, practically without focus difference. The high optical performance is achieved by a sophisticated optical design and the use of ultra low dispersion glass. A special broadband coating reduces stray light and increases transmission over the whole spectral range.

These lenses offer:

- *Spectral sensitivity optimised for CCD cameras*
- *Usability in both visible and infrared range (400-1000nm), practically without focus difference*
- *Higher sensitivity obtained because of greater spectral bandwidth (especially with artificial light approx. 1.5f/stops)*
- *Super broadband coating and thereby reduced stray light and increased transmission*
- *Reduced color aberrations due to use of ultra low dispersion glass*
- *Minimal geometric distortion*
- *Improved illumination distribution*
- *Increased modulation*

The overall technical data for the Schneider-Kreuznach Xenoplan 1.9/35mm objective is given in Table 1 and Figure 49.

Table 1: Optical and opto-mechanical data for the Schneider-Kreuznach Xenoplan 1.9/35 mm objective (<http://www.schneideroptics.com>, 2000-01-31) (Schneider Optics Inc. 2000).

Opto-mechanical data		Optical data	
Filter thread (front)	M 49 x 0.75	Effective focal length (F')	34.9 mm
Rear outer diameter	standard C-mount	Front focal length (SF)	-6.5 mm
Aperture	f/1.9-22	Back focal length (S'F')	17.0 mm
Flange focal distance	standard C-mount	Principal point of separation (HH')	-13.4 mm
Overall length	32.9 mm	Pupil Magnification (AP/EP)	0.879
Recommended format	2/3" 1/2"	Image plane height (Diagonal 2u')	11.0 mm

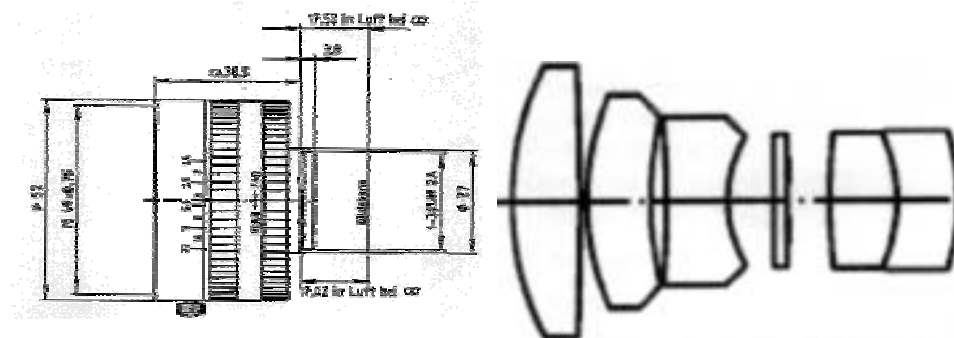


Figure 49: Sketch of the Schneider-Kreuznach Xenoplan 1.9/35mm objective to the left and the arrangement of the lenses to the right (Schneider Optics Inc. 2000).

Since the objective is optimised for light between 400 and 1000nm it is equipped with an ultraviolet blocking filter cutting off all light below 400 nm. Borregaard (1997) recognised that the front objective seemed to be the major source of crosstalk by reflections between the lens and the entrance slit of the PGP-element. A baffle with a narrow slit attached to the objective could be used to eliminate the "side-light". A high quality Canon lens as the front objective seemed to perform much better compared to the Schneider-Kreuznach Xenoplan 1.9/35mm objective (Borregaard 1997). However despite the performance problems the Schneider-Kreuznach Xenoplan objective will be used in this report.

As can be seen in Figure 49 there is a scale indicating the aperture and a knot to lock the settings. However for the focus ring there is neither a scale nor a knot, which would have been a valuable feature.

In today's PGP spectrographs from Specim the "mirror" effect from the slit plate has been removed by blackening and only 4-6% of the light is reflected back to the front objective. The new series of Schneider objectives also have very good lock both in aperture and focus (Esko Herrala, Specim, *pers. comm.*, 2002)

4.2 The VTTVIS PGP unit

The PGP spectrograph was assembled in 1994 and is one of the first units produced by VTT electronics, Finland. Today the line spectrometer is commercialised by SPECIM, Spectral Imaging Ltd. Finland. Several performance improvements have been done to the PGP-unit since 1994. However in this section the focus be on the specification and performance of the

PGP-unit delivered to The Department of Agricultural Sciences, AgroTechnology, KVL, Denmark, in 1995.

According to Esko Herrala, Specim, the error sources discussed in this section is partly related to older instruments like the VTTVIS system used in this report.

4.2.1 The slit

There is divergence in the actual slit width for the VTTVIS in the literature. In the Imaging Spectrograph Users Manual for the VTTVIS the slit width is 100 μ m (Vaarala 1994). However according to Borregaard (1997) Herrala has through a personal communication in 1996 stated that the slit width of the VTTVIS is 60-80 μ m and not 100 μ m. Therefore the actual slit width is set to 80 μ m in this report.

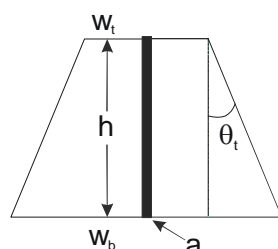
The length of the slit is 8.8 mm (Vaarala 1994).

4.2.2 The lenses

The VTTVIS has two high quality triplet lenses Melles Griot 01LA003 or 01LA005 that are used to collimate light (collimate lens) to the PGP-element and to focus light at the CCD array. The focal length of the lens is 40 mm with a NA (f-number) of 0.12. Triplet lens 01LA003 has an antireflection coating as specified in Melles Griot Optics Guide 5 catalog (Herrala and Voutilainen 1994).

4.2.3 The PGP-element

Table 2: Dimensions and technical data for the PGP-element in the VTTVIS.
Source: SPECIM Ltd.

	w_t :	4.07 (calculated)	- Width of prism top plane
	w_b :	6.4 mm	- Width of prism bottom plane
	h :	20 mm	- Height of prism
	θ_t :	11.7°	- Prism top angle
	a :	480 lines mm ⁻¹	- Grating constant of HOE
	n :	1.54 at 550 nm	- Refraction constant air->prism
	λ_c :	555 nm	- Central wavelength

In the VTTVIS a KG3 filter from Schott is placed between the collimate lens and the grating in order to eliminate excess NIR light which could cause stray light problems. This filter is slightly absorbing in the red part of the spectrum (650-700). This is called spectral flattening and helps to reduce the high dynamic range caused by the lamp spectral distribution and the CCD sensitivity (peaking in the red part of the spectrum (Herrala and Voutilainen 1994).

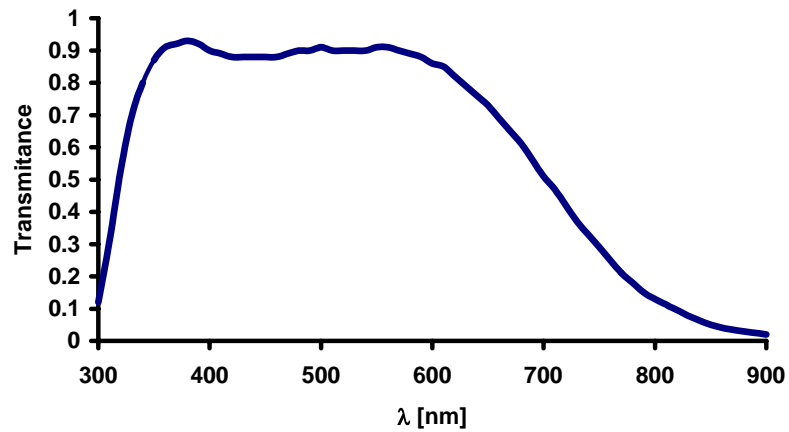


Figure 50: Transmittance of the KG3 filter from Schott inside the PGP-element (Herrala and Voutilainen 1994).

The nearly symmetrically prisms is coated at the input and output surfaces with a standard MgF_2 -antireflection coating (Herrala and Voutilainen 1994).

The grating in the VTTVIS PGP-element is based on a holographically produced volume transmission grating manufactured on DCG between two protective glass plates by Physical Optics Corporation. After sealing the holographic grating can tolerate considerable amount of humidity, temperature (tested up to 80 °C), and optical radiation together with physical shock and vibration (Herrala and Voutilainen 1994). According to the manufacture the diffraction efficiency (DE) of their gratings in the VIS region is between 30 and 70 %. The grating used in the VTTVIS had DE 70, 67, and 42 % at 413, 543, and 670 nm, respectively (Herrala and Voutilainen 1994).

VTT Electronics extrapolated the actual spectral range from the VTTVIS from a linearity experiment to approx. 399 to 708 nm. The specification was 400 to 720 nm ± 5 nm. However camera mount tolerances may cause some dislocation of the spectral range (Herrala et al. 1994b).

4.2.4 Performance of the VTTVIS based on ray tracing

In February 2000 ray-tracing results revealing the scale of the aberration errors in the VTTVIS were received from SPECIM Ltd. The ray tracing consists of five spot diagrams in the spectral range of 400 nm to 700 nm in 25 nm steps. Each of the spots corresponds to different distances from the centre axis towards the edge of the detector: centre of detector, 1.1 mm, 2.2 mm, 3.3 mm, and 4.4 mm for the vertical centre respectively. Due to the symmetry of PGP spectrograph only the right half of the image plane is covered.

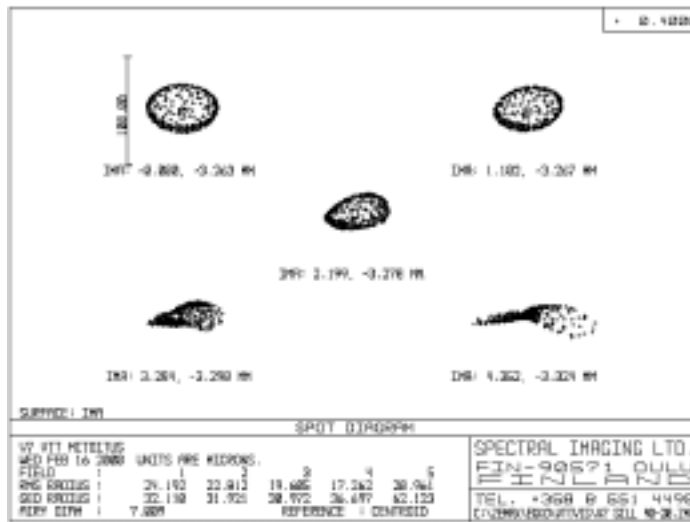


Figure 51: Example of a ray tracing spot diagram for the VTTVIS at 400 nm. The small open circle in each spot diagram indicates the centre of the cloud.

Table 3: Result from the ray tracing in the spectral range of 400 nm to 700 nm in 25 nm steps performed by SPECIM Ltd. Each of the locations corresponds to different distances from the centre axis towards the edge of the detector: centre of detector, 1.1 mm, 2.2 mm, 3.3 mm, and 4.4 mm for the vertical centre respectively. The spot location diagrams at 400 nm are illustrated in Figure 51.

Wavelength [nm]	Centre location of spot diagram [horizontal (h), vertical (v) in mm from centre of the CCD array]							
	h	v	h	v	h	v	h	v
400	0	-3.263	1.102	-3.267	2.199	-3.278	3.284	-3.298
425	0	-2.706	1.101	-2.710	2.196	-2.721	3.280	-2.739
450	0	-2.165	1.100	-2.169	2.194	-2.179	3.276	-2.196
475	0	-1.637	1.099	-1.640	2.192	-1.650	3.273	-1.666
500	0	-1.117	1.098	-1.120	2.191	-1.129	3.271	-1.145
525	0	-0.605	1.098	-0.608	2.190	-0.616	3.270	-0.631
550	0	-0.098	1.097	-0.101	2.189	-0.109	3.269	-0.122
575	0	0.404	1.097	0.401	2.189	0.394	3.269	0.382
600	0	0.903	1.097	0.900	2.189	0.894	3.269	0.882
625	0	1.399	1.098	1.397	2.190	1.391	3.270	1.380
650	0	1.893	1.098	1.891	2.190	1.886	3.271	1.876
675	0	2.386	1.099	2.385	2.192	2.380	3.273	2.371
700	0	2.879	1.099	2.877	2.193	2.873	3.276	2.865
725	0	3.370	1.100	3.369	2.195	3.365	3.279	3.360
750	0	3.863	1.102	3.862	2.198	3.859	3.283	3.854

Based on the results from the ray tracing it is possible to extract the extent of the three aberration errors: spectral linearity, bending of spectral lines at the imaging plane, and distortion of the spatial axis depending of wavelength.

4.2.4.1 Testing linearity of spectral lines at the imaging plane

Based on section 3.5 page 41 it cannot be expected that there is a linear relation between vertical position at the CCD array and the wavelength. However depending on the demands and the exactness to which a narrow spectral band can be measured at the CCD array and of course also on the slit

width an assumed linear relationship could be sufficient. Based on the ray tracing in Table 3 an optimal fitting equation for the relation between a specific wavelength and its CCD location can be estimated at 2x4 horizontal positions plus 1 (~the centre of the PGP) for the imaging plane projected at CCD array due the symmetry of the PGP-element. The spectral ray trace for the 5 horizontal positions 0, 1.1, 2.2, 3.3, and 4.4 mm, respectively is pooled and linear and quadratic fitting is performed. The fitted equations are shown in Equation 6.

A: $V_{\text{pos}} = 2.029074\text{E-}02 \cdot \lambda - 11.31469714$

B: $V_{\text{pos}} = -3.35\text{E-}06 \cdot \lambda^2 + 2.414368\text{E-}02 \cdot \lambda - 12.38332920$

Equation 6: Linear (A) and quadratic (B) fitted equations to the vertical position (V_{pos}) in mm from the horizontal central of the CCD array depending of the specific wavelength (λ) in nm. The fitting is based of ray tracing results for the VTTVIS spectrograph.

The residual plot of the spectral curve fitting based on the results from Equation 6 is shown in Figure 52. The pattern of the residual plot is very similar to Braam *et al.* (1993) shown in Figure 40 page 42. The impact of the spatial location is clear studying the residual plots and caused by the bending of the spectral lines. The quadratic curve fitting reduced the estimation error of the spectral location especially in the blue region. However the pattern in the residuals is still systematic and further improvements can be obtained if necessary. A maximal error of 60 μm in the estimation of the spectral location correspond to approx. 3 nm assuming a spectral range of 350 nm with a vertical imaging height of 7.14 mm at the CCD array.

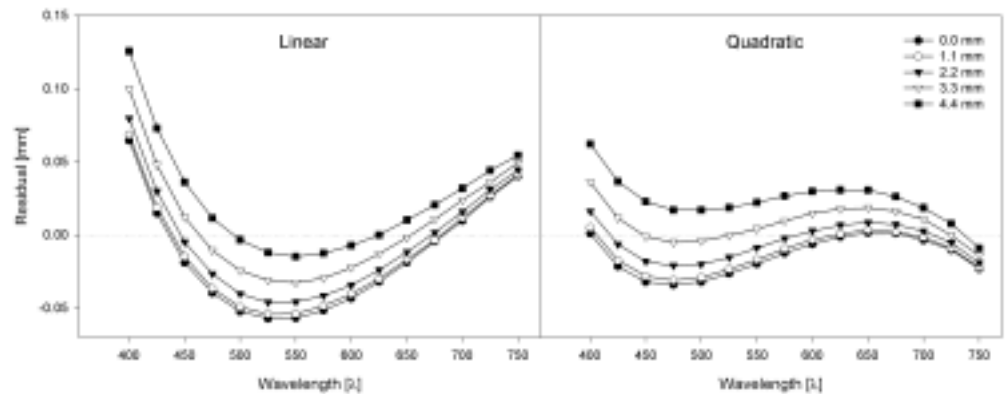


Figure 52: Residual plot of the difference between the predicted vertical position of a wavelength and the estimated position found by ray tracing at different distances from the vertical centre of CCD array. The residual plot is for the linear and quadratic curve fitting equations.

Implementing Equation 8, which model the bending of the spectral lines can significantly reduce the bias caused by varying distances from the horizontal centre of the PGP-element. Equation 7 is a modification of Equation 6B implementing Equation 8 describing the relation between the vertical position at the CCD array depending on the wavelength and the horizontal distance from the centre of the PGP-element.

$$V(\lambda, H_{pos}) = V_{\text{centre-pos}}(\lambda) + V_D(\lambda, H_{pos}) = A \cdot \lambda^2 + B \cdot \lambda + C + (b \cdot \lambda + c) \cdot H_{pos}^2$$

$$= A \cdot \lambda^2 + (B + b \cdot H_{pos}^2) \cdot \lambda + (C + c \cdot H_{pos}^2)$$

$$A = -3.36\text{E} - 6$$

$$B = 0.02411085$$

$$C = -12.34491484$$

$$b = 6.8214\text{E} - 6$$

$$c = -5.9200667\text{E} - 3$$

Equation 7: $V(\lambda, H_{pos})$ [mm] is the quadratic fit of the relationship between the vertical position of a specific wavelength at the horizontal centre of the CCD array $V_{\text{centre-pos}}(\lambda)$ combined with the fitted equation describing the bending of the spectral lines depending on the wavelength and the horizontal distance from horizontal centre of the CCD array $V_D(\lambda, H_{pos})$. A, B, C, b, and c are the fitted constants based on the ray tracing results of the VTTVIS.

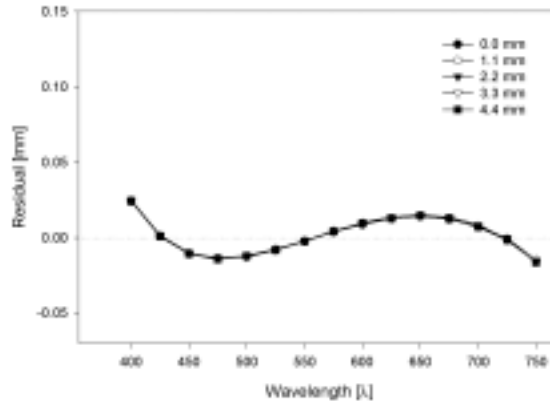


Figure 53: Residual plot of the difference between the predicted vertical position of a spectral wavelength and the measure position found by ray tracing at different distances from the vertical centre of CCD array. The residual plot is for the quadratic curve fitting equation combined with a fitted equation describing the spectral bending.

When comparing Figure 52 and Figure 53 it is clear that the systematic error caused by the spectral bending is almost eliminated. By including the spectral bending it is only necessary to measure the spectral distribution at the horizontal centre of the object line in order to perform the spectral calibration. Still according to the residual plot in Figure 53 there is a systematic pattern, which the quadratic fitting cannot overcome. However the maximal error of 25 μm in the estimation of the spectral location correspond to approx. 1.2 nm assuming a spectral range of 350 nm with a vertical imaging height of 7.14 mm at the CCD array.

4.2.4.2 Testing the bending of the spectral lines at the imaging plane

Based on the ray tracing for the VTTVIS it is possible to quantify the bending of the spectral lines at the imaging plane. Figure 54 shows the bending in steps of 50 nm by plotting the vertical distance between the spectral location at the horizontal centre (0.0 mm) and the actual vertical location. The spectral bending is smallest for 750 nm increasing with decreasing wavelength. The overall shape of the bending is similar to the results of Vaarala *et al.* (1997).

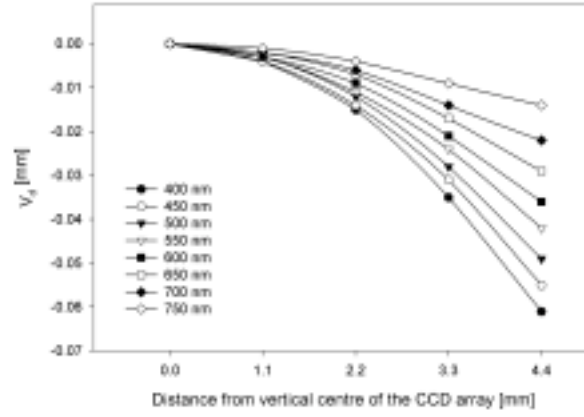


Figure 54: Spectral bending at the imaging plane for the VTTVIS based on ray tracing. V_d is the vertical distance from the spectral location at the horizontal centre of the imaging plane depending on wavelength.

Studying V_d and its dependence on both wavelength and the distance from the vertical centre of the image plane it becomes clear that one relatively simple equation can almost eliminate the errors caused by the spectral bending.

$$V_D(\lambda, H_{pos}) = (6.8214E-06 \cdot \lambda - 0.0059200667) \cdot H_{pos}^2$$

Equation 8: The vertical distance in mm from the spectral location at the horizontal centre of the imaging plane (V_d) depending on wavelength (λ) and on the horizontal distance from the vertical centre of imaging plane (H_{pos}). The results are based on ray tracing plot diagrams for the VTTVIS spectrograph.

By applying Equation 8 the maximal error in the estimation of the spectral location is reduced from 60 μm when assuming the spectral location is a straight horizontal line till a maximum of 1.5 μm which is a reduction of almost 40 times.

The bending of the spectral lines is all downwards according to the theory in section 3.6 on page 42 and Vaarala *et al.* (1997). However according to the theory describing the spectral distortion of a PGP-spectrograph it was also expected to have a certain degree of upward bending at wavelengths longer than the central wavelength at 555 nm for the VTTVIS and downward bending for shorter wavelengths, which seems not the case for the VTTVIS. Taking the distortion of spatial axis depending on wavelength in 0 below into consideration, which shows the visual centre symmetry at 575 nm it is now possible to extract and show the impact of the latter theory. If pincushion distortion is present as shown in Figure 44 on page 46 the overall downward spectral bending down this when doing visual inspection. Assuming the overall downward bending is almost constant for all wavelengths if the CCD array is exactly in line with the paraxial focal plane then by subtracting the actual vertical location of a wavelength with the vertical location of the wavelength at 575 nm for a specific horizontal location it should be possible to extract the pincushion bending of the spectral lines.

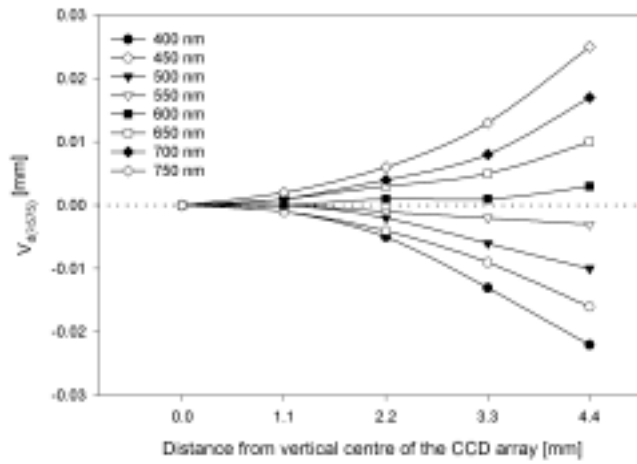


Figure 55: Plot illustrating spectral pincushion distortion in the VTTVIS based on ray tracing after subtracting an all downward spectral bending. By subtracting the actual vertical location of a wavelength with the vertical location of the wavelength at 575 nm ($V_{d(\lambda 570)}$) for a specific distance from the vertical centre of the CCD array it is possible illustrate the pincushion bending of the spectral lines.

4.2.4.3 Fitted equation describing the wavelength at the CCD array

Based on results from the ray tracing results equations have been developed and fitted in order to minimise the systematic errors caused by different distortion errors. However these equations describes the vertical location depending on the horizontal distance from the centre of the CCD array and the specific wavelength. However for practical use the horizontal and vertical distance from the centre of the CCD array is known and the specific wavelength is unknown. By rearranging Equation 7 it is possible to obtain an equation for use in practice as shown in Equation 9 for the VTTVIS spectrograph.

$$\lambda(H_{pos}, V_{pos}) = \frac{-(B + b \cdot H_{pos}^2) + \sqrt{(B + b \cdot H_{pos}^2)^2 - 4 \cdot A \cdot (C + c \cdot H_{pos}^2 - V_{pos})}}{2 \cdot A}$$

H_{pos} : Horizontal distance from the centre of the CCD array[mm]

V_{pos} : Vertical distance from the centre of the CCD array[mm]

$$A = -3.36E - 6$$

$$B = 0.02411085$$

$$C = -12.34491484$$

$$b = 6.8214E - 6$$

$$c = -5.9200667E - 3$$

Equation 9: $\lambda(H_{pos}, V_{pos})$ predicts the specific wavelength at the imaging plane of the VTTVIS depending on the horizontal and vertical distance from the centre of the CCD array. The equation and the parameters are based on ray tracing on the VISVTT spectrograph.

Table 4: The specific wavelength for the VTTVIS depending on the location at the CCD array. The wavelength is calculated by use of Equation 9, which is estimated from the ray tracing results

Vertical distance from the centre of CCD [mm]	Horizontal distance from the centre of the CCD [mm]				
	0	1.1	2.2	3.3	4.4
	Wavelength [λ]				
4	758.0	758.0	758.2	758.4	758.7
3.5	731.8	731.9	732.0	732.3	732.7
3	705.9	705.9	706.1	706.5	707.0
2.5	680.2	680.2	680.5	680.9	681.4
2	654.7	654.8	655.0	655.5	656.1
1.5	629.4	629.5	629.8	630.3	631.0
1	604.4	604.5	604.8	605.4	606.1
0.5	579.6	579.7	580.0	580.6	581.4
0	554.9	555.0	555.4	556.1	556.9
-0.5	530.5	530.6	531.0	531.7	532.6
-1	506.2	506.4	506.8	507.5	508.5
-1.5	482.2	482.3	482.8	483.6	484.6
-2	458.3	458.5	459.0	459.8	460.9
-2.5	434.6	434.8	435.3	436.2	437.3
-3	411.1	411.3	411.8	412.7	413.9
-3.5	387.8	388.0	388.5	389.5	390.7
-4	364.6	364.8	365.4	366.4	367.7

The distribution of the specific wavelengths at the imaging plane of the VTTVIS according to Equation 9 is shown in

Table 4. This gives a good idea of that the specific wavelengths are not distributed in horizontal lines at the CCD array as often assumed by different authors.

4.2.4.4 Smearing of object points at the PGP imaging plane

Herrala *et al.* (1994a) illustrated by use of a spot diagram a good summary of the point smearing at the Inspector V7 imaging plane as shown in Figure 56. For short-wave spots below 450 nm the smearing in the spatial direction becomes relatively large compare to the CCD resolution. At 400 nm the spot diameter has grown to approx. 60 μm , which is more than 2 pixels in size if projected at the CCD array of the VTTVIS system.

In the spectral direction the spot smearing seems to be relative large for the 400 nm spot but also for the slit perimeter spots at displaced 4.0 mm. However, due to the configuration of the VTTVIS the slit perimeter spots correspond better to the spot at the 3.0 spot displacements. Thus, the ray smearing seems to be significant for wavelength below 450 nm and for perimeter pixels. However the level of significance will also depend on the resolution of the CCD array used.

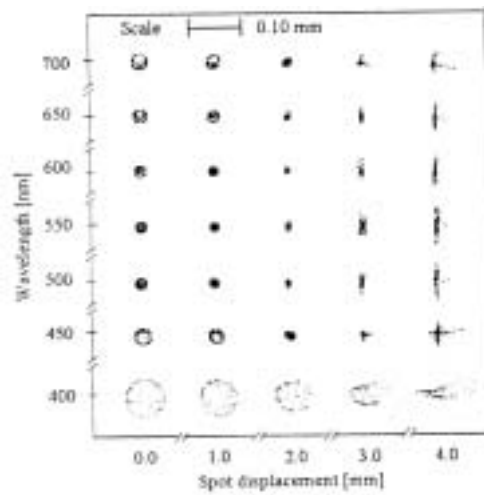


Figure 56: Simulated spot diagram across a 6.6 x 8.8 mm CCD detector surface. Due to symmetry along the centerline of the detector only half of the diagram is shown (Herrala et al. 1994a).

4.2.4.5 Distortion of the spatial axis depending on the wavelength

The ray tracing results for the VTTVIS can also be used to estimate the distortion of the spatial axis projected at the CCD array. Along the spatial axis the horizontal distance from the centre of the CCD array have been measured in steps of 25 nm at pre-set horizontal distances 0, 1.1, 2.2, 3.3, and 4.4 mm. The minimum horizontal distance from the centre of the CCD array is at 575 nm for all pre-set groups. This means that the sagittal plane of the collimating lens is located at 575 nm. Therefore by subtracting the horizontal distance from the centre of the CCD array at 575 nm from the actual horizontal distance from the centre within the spectral range of 400 nm till 750 nm within each of the pre-set groups it is possible to estimate the extent of the spatial distortion.

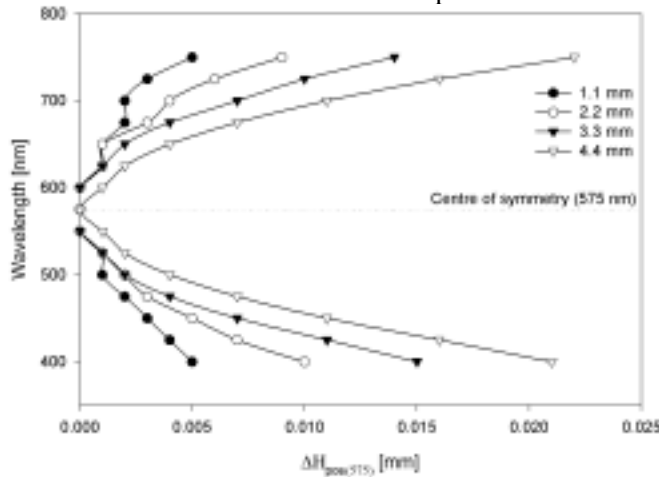


Figure 57: The spatial distortion within the VTTVIS for horizontal pre-set distances 1.1, 2.2, 3.3, and 4.4 mm from the centre of the CCD array in the spectral range of 400 nm till 750 nm. The wavelength, which have the shortest distance from the horizontal distance from the centre of the CCD array for all 4 pre-set groups is located at 575 nm is the centre of symmetry for the spatial distortion. $\Delta H_{pos(575)}$ is the horizontal distance between the location for a specific wavelength till the location at 575 nm within each of the pre-set groups for a specific object point i.

By use of curve fitting $\Delta H_{\text{pos}(575)}$ can be described by Equation 10 with a R^2 of 0.99 and maximal residual value of approx. 1.8 μm .

$$\Delta H_{\text{pos}(575)} = A \cdot \lambda_{\Delta 575}^2(\lambda) \cdot H_{\text{pos}(575)}$$

$$A = 1.5241419\text{E} - 7$$

Equation 10: The spatial distortion in the VTTVIS described as the horizontal distance between the location at the 575 nm and the location for a specific wavelength ($\Delta H_{\text{pos}(575)}$) in mm. $\lambda_{\Delta 575}(\lambda)$ is the spectral difference between the actual wavelength and 575 nm. $H_{\text{pos}(575)}$ is the distance of the measured point from the centre of the CCD at 575 nm.

The dimension of the CCD array is 6.5 x 8.6 mm, which correspond to the spatial axis x spectral axis for the S-BIG camera unit used for the VTTVIS. The CCD array is 6.5 x 8.6 mm corresponding to 242 x 375 pixels and a pixel dimension of 27 x 23 μm . Assume an object area i is located in pixel column 241 at 575 nm which is approx. 3.8182 mm from the centre of the CCD array. Then according to Equation 10 the centre of the latter object pixel will have moved approx. 17.8 μm further away at 750 nm meaning that 66% of area i is located in pixel column 242 and not pixel column 241.

4.3 The CCD camera unit

The imaging unit mounted to the PGP spectrograph is a 16-bit cooled SBIG CCD camera model ST-6, from Santa Barbara Instrument Group.

The CCD is equipped with a 50 K TE-cooler enabling cooling down to approx. -30 °C at an ambient temperature of 20 °C (Borregaard 1997; Santa Barbara Instrument Group 1993a). However operating under various sampling conditions -10 °C as cooling set-point seems to be practical achievable under all temperature conditions.

The elements of the CPU in the camera are namely the microcontroller, the frame store, and the power supply. The microcontroller is a 9.2 MHz 80188 based upon the 8088 microprocessor. It controls the operation of the CCD camera at the lowest level (acting as a slave), receiving commands from the host/master computer and executing sequences of instructions to control and acquire images. The frames store allows holding three images in the CPU: a light image, a dark image, and a double-precision accumulation image. Finally, the power supply takes the supplied 12 volts and produces the various regulated voltages required by the CPU (Santa Barbara Instrument Group 1993a). Since the camera CPU act as slave it is relatively simple to develop programs controlling the camera. Santa Barbara Instrument Group (1993b) has published the low level CPU command structure such a direct control of the SBIG ST-6 camera. Jørgensen and Rasmussen (2002) have for example developed a Matlab program, LISS, capable of controlling and collecting data from two SBIG cameras simultaneously.

Santa Barbara Instrument Group (1993a) has developed a CCD operating software CCDOPS for the SBIG ST-6 camera. CCDOPS is mainly for astronomy use. This software packet is therefore not suited for measurement under varying lightning conditions like canopy reflection measurements under natural irradiation condition. For this purpose LISS is much better suited.

The communication between SBIG ST-6 and the master computer is via an RS-232 serial connection at a baud rate from 9.6 till 115 kilobit (Santa Barbara Instrument Group 1993a; Santa Barbara Instrument Group 1993b).

The CCD used is a Texas Instruments TC241-40 780- x 488-pixel frame-transfer CCD image sensor (Santa Barbara Instrument Group 1993a; Texas

Instruments 1991). According to Santa Barbara Instrument Group (1993a) the number of pixels is 375 x 242 each with a pixel dimension of 23 x 27 μ m giving an efficient light sensing array dimension of 6.6 x 8.8 mm. Comparing this with technical description of the TC241-40 CCD and Figure 31 on page 30 this means that 24 columns are used for potential dark references and 2 x 3 columns are used as border columns. In order to obtain a column resolution of 375 the columns are binning two by two. Further two rows in both the image sensing and the storage sensing area is used as border protection rows between the two areas.

By use of binning the following pixels sizes is available for the three possible readout modes of the SBIG ST-6 camera:

Table 5: Obtainable pixel sizes for the SBIG ST-6 camera by use of binning (Santa Barbara Instrument Group 1993a).

<i>Readout Modes</i>	<i>Number of Pixels</i>	<i>Pixel Size (μm)</i>	<i>Binning</i>
High	375 x 242	23.0 x 27	2:1 x 1:1
Medium	250 x 242	34.5 x 27	3:1 x 1:1
Low	250 x 121	34.5 x 54	3:1 x 2:1

The CCD TC241 spectral responsivity is shown in Figure 58. The CCD is UV enhanced due to the virtual phase architecture as discussed in section 3.4.1, page 29. The pixel sensitivity in the NIR range above 900 nm decreases rapidly towards zero.

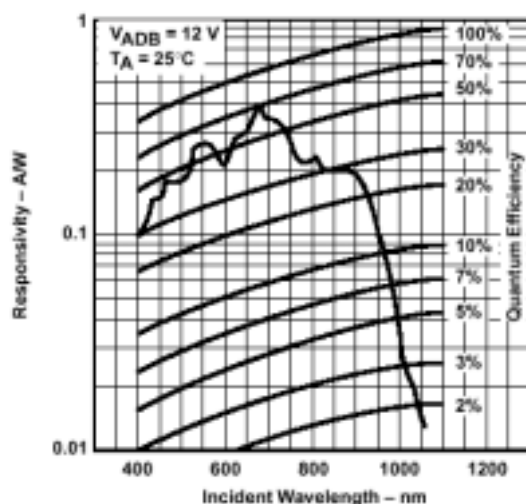


Figure 58: Spectral responsivity of CCD model TC241 from Texas Instrument used in the digital camera SBIG ST-6 (Texas Instruments 1991).

In Table 6 some of the electrical performance characteristics are given according to Texas Instruments (1991).

The camera is using frame transfer as exposure shutter. The speed of electronic shutter is characterized by time it takes after ended exposure to move the exposed pixels from the imaging area to the storage area. This process is fast and takes 1/300 second to perform minimizing streaking (Santa Barbara Instrument Group 1993a). Besides the electronic shutter the SBIG ST-6 has a mechanical shutter, which is used when recording dark frames preventing any light to enter the image area.

Table 6: Some of the electrical performance characteristics at 25 °C according to Texas Instruments (1991).

Parameter	Value	Comment
Dynamic range	60 dB	Dynamic range is $-20\log(\text{mean-noise signal divided by the saturation-output signal})$. The antiblooming mode functionality is disabled.
Charge-conversion factor	1.6 $\mu\text{V}/\text{e}$	
Charge transfer efficiency (CTE)	0.99995	
Signal-response delay	20 nm	
Gamma	0.98	Gamma (γ) is the value of the exponent in the equation below for two points on the linear portion of the transfer-function curve (this value represents points near saturation): $\left(\frac{\text{Exposure}(2)}{\text{Exposure}(1)}\right)^\gamma = \left(\frac{\text{Output_signal}(2)}{\text{Output_signal}(1)}\right)$
1/f noise (5 kHz)	0.13 $\mu\text{V}/\sqrt{\text{Hz}}$	
Random noise (f = 100 kHz)	0.11 $\mu\text{V}/\sqrt{\text{Hz}}$	
Noise-equivalent signal	120 electrons	

Table 7: Optical characteristics for the CCD in the SBIG ST-6 camera (Texas Instruments 1991), $T_A=40$ °C (unless otherwise noted). The TC241-40 is being use in the SBIG ST-6 camera.

PARAMETER			MIN	TYP	MAX	UNIT
Sensitivity	No IR filter	Measured at V_{LJ}	150		mV/e	
	With IR filter	(see Notes 10 and 11)	19			
Saturation signal, V_{sat} (see Note 12)	Antiblooming disabled, interface off		320	400	mV	
Maximum usable signal, V_{use}	Antiblooming enabled, interface on		160	360	mV	
Blooming-overload ratio (see Note 13)	Interface on		100			
	Interface off		200			
Image-area well capacity			250 x 10 ³		electrons	
Smear (see Note 14)			See Note 15		0.00072	
Dark current	Interface off		$T_A = 21^\circ\text{C}$		0.027	
Dark signal (see Note 16)	TC241-30				15	mV
	TC241-40				20	
Pixel uniformity	Output signal = 50 mV \pm 10 mV	TC241-30			3.5	mV
		TC241-40			5	
Column uniformity	Output signal = 50 mV \pm 10 mV	TC241-30			0.5	mV
		TC241-40			0.7	
Shading	Output signal = 100 mV				10%	

NOTES: 10. Sensitivity is measured at an integration time of 10.667 ms with a source temperature of 2856 K. A CM-500 filter is used.

11. V_{LJ} is the output voltage that represents the threshold of operation of antiblooming. $V_{LJ} = 1/2$ saturation signal.

12. Saturation is the condition in which further increase in exposure does not lead to further increase in output signal.

13. Blooming-overload ratio is the ratio of blooming exposure to saturation exposure.

14. Smear is a measure of the error induced by transferring charge through an illuminated pixel in shutterless operation. It is equivalent to the ratio of the single-pixel transfer time during a feed dump to the exposure time using an illuminated section that is 1/10 of the image-area vertical height with recommended clock frequencies.

15. Exposure time is 10.67 ms and the feed-dump clocking rate during vertical timing is 2.05 MHz.

16. Dark-signal level is measured from the dummy pixels.

4.4 Mounting the camera to the spectrograph

There are two orientations of the CCD chip with respect to the PGP-element because the image area is not square. The CCD can be mounted with a wide spectral range and a narrow spatial range, 6.5 x 8.6 mm, or with a narrow spectral range and a wide spatial range, 8.6 x 6.5 mm.

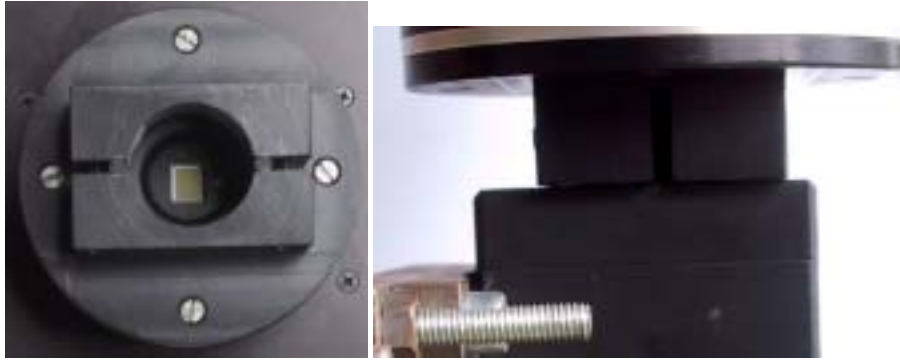


Figure 59: Left - Picture of the clamp arrangement on the SBIG ST-6 CCD camera used for fixation onto the VTTVIS PGP spectrograph. The image area of TC241 CCD can be seen in the center of image. Right – Picture of the clamp mounted on the PGP spectrograph. Note the slim line of light visible the left site of the clamp showing the camera is twisted at the mount.

The connection between the spectrograph and the SBIG ST-6 camera is a clamp arrangement as shown in Figure 59. The clamp arrangement has some disadvantages making it difficult to mount and orientate the CCD camera correctly. For example when rotating the CCD pixel columns into line with the spatial axes the clamp must be relaxed. After the adjustment the tightening is rather difficult without rotating the CCD a little. Due to the lack of a guiding thread there is also risk of changing the distance between the focus plane and the CCD getting the image out of focus. Due to the use of a clamp fitting there is also a risk of twisting at the assembling point resulting in image distortion as illustrated in Figure 48 page 49.

The clamp mounting is not used in today's systems anymore (Esko Herrala, Specim, *pers. comm.* 2002).

4.5 The measuring rig

The measuring rig consists of the two line imaging spectrometers one for the near infrared range (similar to Inspector N10) and one for the visual range (similar to Inspector V7), a Canon Digital IXUS, and two grey plate reference plates. The VTTVIS is angled 3.5° from nadir and the front lens is 108.5 cm above the horizontal plane of the grey plate surface. The Canon camera is used for documentation and is placed next to the lens of the VTTVIS with its CCD centreline in line with the slit of the PGP spectrograph. The viewing angle of the canon camera is similar to the VTTVIS and the distance between the centres of the two lenses is 6 cm. Two Spectralon™ panels both having Lambertian reflective properties with a reflectance of 25% within the spectral range of the VTTVIS are used reference. The grey plates were cut out of a Spectralon™ multi-step target panel SRT-MS-100. By using two references it is possible detect if one of the reference is by accident shadowed by for example a leaf or dirty in some way. The mounting frame is build very solid in order to fixate all units efficiently avoiding disturbing vibrations. The setup is shown Figure 60.



Figure 60: The VTTVIS measuring rig.

Jørgensen at Rasmussen (2002) further describes the hardware and software used to do measurements with the whole system.

4.5.1 Concerns using doped Spectralon™ as irradiation reference

According to Labsphere (2001) Spectralon™ grey scale material has a variance in reflectance $<0.5\%$ in the spectral range of the VTTVIS. The reference panels are primarily used to standardise measurements of target radiant flux in order to derive the biconical reflectance factor (BRF) on the assumption that the flux reflected from the panel can be used as a surrogate of the incident global irradiation (Kimes and Kirchner 1982) assuming Lambertian properties. However according to E.M. Rollin *et al.* (1997; 2000) both white and especially grey Spectralon™ panels have a non-Lambertian response under field conditions. Variation in the reflectance of the global flux with angle was near-Lambertian for incident angles up to almost 60° for the white Spectralon™ under direct solar irradiation. In contrast, grey Spectralon™ appeared near-Lambertian for incident angles below 30° as shown in Figure 61. Thus E.M. Rollin *et al.* (1997) concluded grey Spectralon™ was less suitable than white Spectralon™ for field use in UK. However studying Figure 61right it can also be argued that up to a relative incident angle of approximately 50° the grey Spectralon™ deviate less than the white Spectralon™.

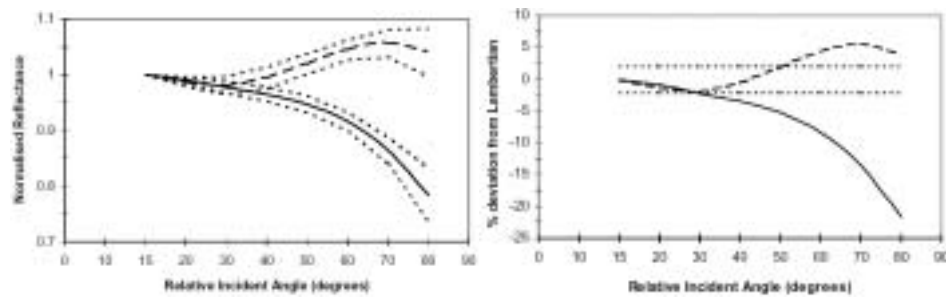


Figure 61: Left - Normalised reflectance of direct irradiance (divided by the cosine of the incident angle and normalised to incident angle of 15°) for optical grade Spectralon™ (solid line) and grey Spectralon™ (dashed line). Errors bars are denoted by the dotted lines. Right - Deviation from Lambertian of the reflected direct irradiance (divided by the cosine of the incident angle and normalised to incident angle of 15°) for optical grade Spectralon™ (solid line) and grey Spectralon™ (dashed line). A Lambertian response would be a straight line through zero. The dotted lines indicate $\pm 2\%$ deviation from Lambertian (Rollin *et al.* 1997).

The maximal solar altitude in the area of Copenhagen, Denmark, where the VTTVIS has been used is less than 58° ($\sim 32^\circ$ nadir) at solstice. Thus, using a grey Spectralon™ as reference panel for the VTTVIS the non-Lambertian properties of the panel should be taken into account in terms of the directional and spectral reflectance properties.

The reason for not using white Spectralon™ (99% reflective) is that a considerable part of the dynamic range of the CCD would be wasted covering the more than 50% gap in reflection between the canopy and the reference panel.

According to R.D. Jackson *et al.* (1987) the reference panel should be calibrated under field conditions using the equipment it is intended to be used with since a precise laboratory calibration will not apply exactly due to different measuring condition like spectral resolution, light source, and/or instrument characteristics. Thus a procedure calibrating the grey reference panel to the VTTVIS under field condition should be developed. Such a procedure could be adapted from the method described by R.D. Jackson *et al.* (1987) and E.A. Walter-Shea *et al.* (1993). R.D. Jackson *et al.* (1992) concluded that variation between Spectralon™ panels (in both their directional/directional and directional/hemispherical reflectance) is sufficient small for ‘generalized’ calibrations. Thus one calibration of the grey Spectralon™ panel for the VTTVIS should be sufficient. However, under field conditions dust contamination of the panel is likely causing a greater decrease in the reflectance at the shorter wavelengths (~ 450 nm) than at longer wavelengths (~ 850 nm) (Jackson *et al.* 1987). Therefore the calibration of the panel should be verified regularly working under field conditions.

R.D. Jackson *et al.* (1992) developed a “general” calibration equations for Spectralon™ panels which could be used if some error can be tolerated and a individual calibration is not available. These equations were for white Spectralon™ panels and it is not known if they can be adapted to Spectralon™ panels doped with black pigment.

4.6 The documentation and classification camera

When performing measurements with a line imaging spectrometer it is difficult for the human mind to interpret and control the object line spectra for potential errors. If however a conventional RedGreenBlue (RGB) picture is

taken simultaneously with each measurement taken with the VTTVIS spectrograph then it will be relatively easy to get a rough idea of the origins to the measured spectra. A simple way to obtain this feature is to place a digital camera next to the lens of the VTTVIS with its CCD centreline in line with the slit of the PGP. Due to the offset between the two lenses there will be a relatively small parallax error when measuring for example canopy with a depth dimension. Still such a setup has proven to be a valuable tool when trying to classify and understand the measured spectra.

4.7 Summary

The VTTVIS system consists of a Scheider-Kreuznach Xenoplan 35 mm front lens for objects within a focus range of 1 to 2 metre, A VTT PGP spectrograph with a spectral range of approx. 400-750 nm depending on the CCD dimension, and a SBIG ST-6 16-bit cooled camera with a TC-241-40 frame-transfer CCD with a resolution of 375 x 242 pixels $\sim 8.8 \times 6.6$ mm.

The SBIG camera has a micro controller which act as slave for external master software hosted by a conventional PC. The master-slave setup makes it relatively easy to develop new software. Jørgensen at Rasmussen (2002) have for example developed such software to do measurements under field condition with varying irradiance levels.

Based on ray tracing estimations for the VTTVIS spectrograph the existence of significant distortion in both the spatial and the spectral direction has been proven. Further it was shown that it was relatively simple to model the image distortion in both directions. Thus there is a basis for correcting the image to a straight row vs. column form cleaned for spatial and spectral bending as illustrated in Figure 7 on page 12. However, the smearing of the rays presented in Figure 56 on page 61 can potentially add complications to such an image correction.

The mounting of the SBIG camera to the PGP spectrograph is based on a clamp system, which has several drawbacks. It is for example difficult to perform an axis alignment of the spectrograph image and the CCD plane without introducing unintentional rotation and/or twisting when tightening the clamp.

The measuring rig is constructed in a manner minimising vibration when measuring. Further the rig is equipped with 25% reflective Spectralon™ panels within the perimeters of the object line enabling irradiance quantification when estimating the hyperspectral reflectance across the object line. However, the grey Spectralon™ have a non-Lambertian response under field conditions, which should be taken into account in terms of the directional and spectral reflectance properties.

A conventional digital camera is placed next to the lens of the VTTVIS with its CCD centreline in line with the slit of the PGP spectrograph. This has proven to be a valuable tool when trying to classify and understand the measured spectra.

5 Adjustment and calibration procedure

It is clear each of the units in the VTTVIS to some degree all add distortion and noise to the projected hyperspectral image of the measured object line. Some of the error sources can be minimised by use of high quality lenses and CCD cameras. However doing a proper calibration of the actual system several error sources can be avoided or minimised. The adjustments and calibrations should be performed prior to any measurements with the VTTVIS:

1. The front lens should be focussed avoiding smearing
2. The distance between the CCD and the PGP image plane must fit the rear focal length of the PGP spectrograph avoiding both spatial and spectral smearing
3. The projected image from the PGP spectrograph must be adjusted very accurate by rotating the CCD until the spectral centre wavelength of the PGP is parallel with the horizontal pixel rows of the CCD.
4. Individual wavelength calibration for each of the columns is important due to the spectral distortion of the PGP spectrograph
5. Hyperspectral flat fielding is a rather complicated task but highly recommended. The flat fielding evens out or minimise bias due to variations in the PGP slit, optical vignetting, and PRNU in the CCD array
6. Correction of the image distortion created by the PGP unit in the spatial and spectral direction. If it is possible to straightening up the image by empirical measurements points four will become unnecessary

The different adjustment and calibration procedures are briefly described in Spectral Imaging Ltd. (1997) and will be used as offset for this chapter. For each procedure the principles are described with focus on the VTTVIS and some examples are given.

When performing the adjustment and calibration procedures it is presupposed that the darkframes are taken under similar conditions is subtracted the raw image prior to any adjustment and calibration evaluations.

5.1 Adjustment of the camera mounting to the spectrograph

After the SBIG CCD camera and the PGP spectrograph has been assembled they must be aligned so that the spatial axis of the spectrograph is parallel to the horizontal pixel rows of the CCD array. When the alignment has ended the back focal length can be optimised (Spectral Imaging Ltd. 1997). The fine-tuning of both the axis alignment and the back focal length both uses the results from moment analysis. The principles will therefore briefly be described.

5.1.1 The principles of moment analysis

The centre of a peak measured with a CCD returns a discrete spectrum. The nature of a spectrum is not discrete but continuous and the exact location a peak is therefore not necessarily within the centre of a CCD pixel. In fact the peak centre can be located between two pixels within the light insensitive area.

Fortunately in this case a sharp peak is always blurred a little after it has passed through the different kind of optics and the neighbouring pixels are therefore receiving a small fraction of the light from the peak. This phenomenon can now be turned into an advantage making it possible to determine the exact location of a peak even though its centre is located between two pixels in the light insensitive area of the CCD. Often the centre of a peak within discrete spectrum is found by fitting a gauss distribution to the spectrum a then determine the centre the gaussian fit. Another approach is to use the moment analysis used by Desmond McMorro, Risø National Laboratory, Denmark <http://www.risoe.dk/afm/personal/demc/demc.htm>) in a Matlab function named *peakm.m* (<http://www.ill.fr/tas/matlab/doc/spec1d/spec1d.html>). The equation for estimating the exact centre is given in Equation 11.

$$pos_{centre} = \frac{\sum_{i=1}^N pos_i \cdot (I_i - I_{background})}{\sum_{i=1}^N (I_i - I_{background})}$$

Equation 11: Finding the centre position of a peak by use of moment analysis. Pos_i ~ i'te pixel position at the spatial pixel column of the measured intensity count. I_i ~ i'te intensity count of the light measured at pos_i . $I_{background}$ ~ average background intensity count. N ~ number of pixels in the selected window.

The principles of the moment analysis are illustrated in Figure 62 by use of a spectral peak created by a mercury lamp. The width of Full Width Half Maximum (FWHM) of the peak can also be estimated by use of the *peakm.m* Matlab function.

$$FWHM = 2 \cdot \sqrt{ABS \left(\frac{\sum_{i=1}^N pos_i^2 \cdot (I_i - I_{background})}{\sum_{i=1}^N (I_i - I_{background})} - \left(\frac{\sum_{i=1}^N pos_i \cdot (I_i - I_{background})}{\sum_{i=1}^N (I_i - I_{background})} \right)^2 \right)}$$

Equation 12: Estimating FWHM of a peak by use of moment analysis. Pos_i ~ i'te pixel position at the spatial pixel column of the measured intensity count. I_i ~ i'te intensity count of the light measured at pos_i . $I_{background}$ ~ average background intensity count. N ~ number of pixels in the selected window.

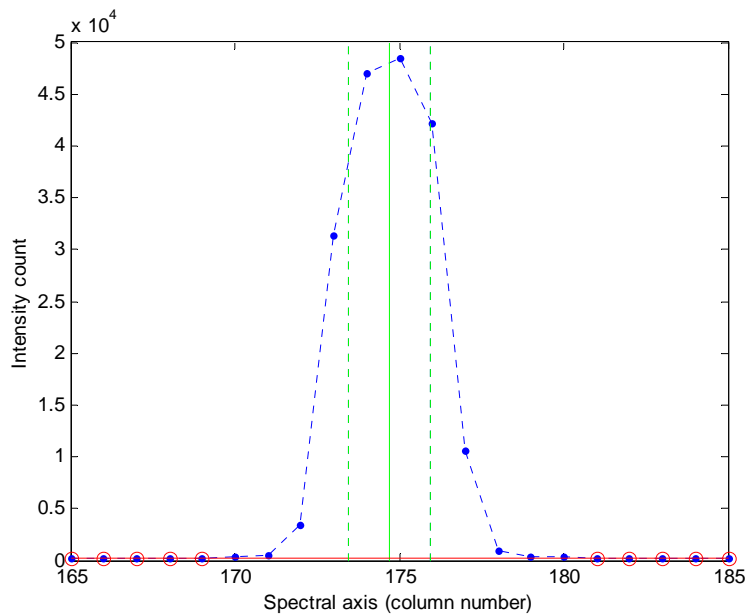


Figure 62: Illustration of the principles behind the moment analysis by use of a mercury peak at 546.07 nm. The blue points are the registered intensity count of a column of the pixels in the spectral direction at CCD array. The red circles indicate the pixels used to calculate the average background signal. The vertical green line shows the calculated centre of the peak. The vertical punctuated green lines gives the calculated FWHM of the peak.

5.1.2 Axis alignment procedure

The axis alignment can be done in several different ways, but the procedure described usually gives the best results.

1. Removed the front lens. *If however the light source is placed behind the front lens and the light is reflected into the lens via a white bar with lambertian properties the removal is often not necessary*
2. Place a light source with narrow spectral lines in front of the spectrograph slit or behind the front lens mounted on the spectrograph and reflect the light back into the spectrograph via a white reference bar placed approx. 1 metre from the front lens. *Good light sources for this are pencil style spectral calibration lamps from Thermo Oriel (2001). An optional integrating sphere with the lamp inside could also be used to obtain more uniform illumination*
3. Perform a rough alignment visually by looking at the measured image in the controlling software like e.g. LISS made by Jørgensen and Rasmussen (2002). *This alignment can also be perform by the original camera controlling software delivered by Santa Barbara Instrument Group (Santa Barbara Instrument Group 1993a; Santa Barbara Instrument Group 1998). The lines should be aligned along the spatial rows so than the peaks of lines have the same spectral pixel number for the first and the last pixel column (Spectral Imaging Ltd. 1997)*
4. The fine-tuning of the alignment cannot be done visually and a specially designed fine-tuning procedure should be used

5.1.2.1 Principles for fine-tuning the axis alignment

Visually it will not be possible to align the axis of the PGP spectrograph image and the CCD array when the rotational difference is below one pixel. The

bending of the spectral lines earlier discussed makes the final adjustment difficult visually. By use of a 2nd order polynomial fit an approx. 100% axis alignment is practically obtainable knowing the spectral bending is symmetrical around the centre of the slit. The procedure is:

1. Estimate the spectral centre position of each peak for every spatial pixel across the spatial axis
2. Fit a 2nd order polynomial through the estimated peak centres.
3. Estimate the spectral peak positions for the first and the last spatial pixel column by use of the 2nd order polynomial
4. Estimate the difference between the two peak positions
5. Rotate the CCD camera until the difference is zero

The principles are schematically illustrated in Figure 63.

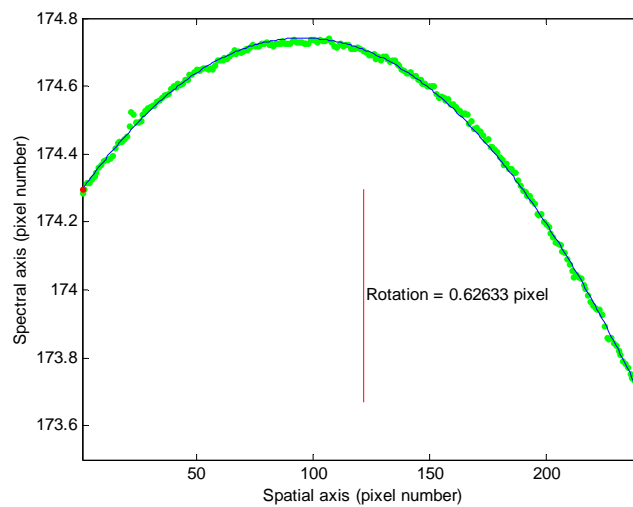


Figure 63: Schematic illustration of fine-tuning axis alignment by use of a mercury peak at 546.07 nm and the fine-tuning procedure. The green points are the estimated peak centres along the slit/spatial axis. The blue line is the 2nd order fit to the peak centres. The red points and the red vertical line illustrate the degree of axis rotation in pixels.

5.1.3 Back focal length (BFL) adjustment

In order to secure the best possible measurement with a relative low degree of spectral and spatial smearing the CCD plane must be located exactly at the BFL of the PGP spectrograph as discussed in section 3.9.1 at page 47. Prior to the BFL adjustment the axis alignment should be performed. In fact the axis alignment setup can be used for the BFL procedure by focussing not on the peak location but on the FWHM and the peak selected. By moving the CCD camera forward and backward the BFL change result in changes in the FWHM of the peak due changes in circle of confusion (see Figure 46 on p. 48). The smallest obtainable FWHM is at the exact position of the paraxial focal plane of the PGP spectrograph equal to the BFL of the spectrograph. The procedure is:

1. Perform the axis alignment procedure. *Keep the exact setup as for the axis alignment procedure without the front lens mounted. In fact the same peak can be used during the following steps*

2. Change the distance of CCD camera on the PGP spectrograph mounting. Avoid any rotation and tilting of the camera during this operation.
3. Measure the relative distance of the CCD camera in relation to the smallest possible longitudinal distance of the camera mounted onto the PGP spectrograph. *The measurement can be done by use of a measuring gauge*
4. Perform a measurement. *This can be done by for example the LISS software developed by Jørgensen and Rasmussen (2002)*
5. Calculated the median of the estimated FWHM values of 242 peaks along the spatial axis.
6. Plot the relative distances versus the median FWHM's.
7. Repeat step 2
8. When several measurements has been collected use this to estimate the optimal relative longitudinal of the CCD camera equal to the BFL of the PGP spectrograph

5.2 Adjustment and focus of the front optic

When the axis alignment procedure and BFL procedure has been performed the last step is to focus the measurant onto the plane of the entrance slit of the PGP spectrograph. This is done by adjusting the focus of the front objective to the distance of the measurant. The focusing is carried out by placing the front lens focus object shown in Figure 64 in the same distance as the object to be measured. Hereafter the focus is adjusted until FWHM of the peak created by the white line in the spatial direction has reached its minimum. During the focussing it is advisable to use a stabilised light source in order to obtain the optimal focus.

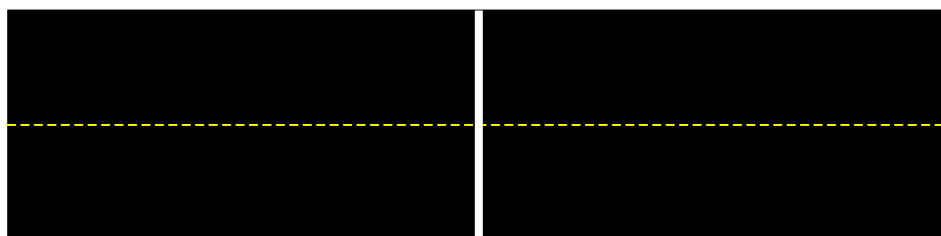


Figure 64: Front lens focus object. The yellow punctuated line indicates the narrow line measure by the VTTVIS. When FWHM of the peak created by the white line has reached its absolute minimum the best possible focus is obtained.

Remember to take the varying focus depths of for example a canopy into account placing the front lens focus object it a proper distance (see section 3.2.2.9 on page 20).

5.3 Spectral calibration procedures for the VTTVIS spectrograph

As discussed earlier the non-linearity in the VTTVIS spectrograph dispersion causes small deviations in the wavelength scale of the image projected onto the CCD array. There is also indication of that a 3rd order polynomial will be able to describe this non-linearity well. To be able to perform a spectral calibration

using a 3rd order polynomial curve fit several known calibration peaks spread in the whole spectral range of the VTTVIS is needed.

Several different calibration sources can potentially be used to create peaks with known wavelengths. Lasers can be used to create known peaks with a very high intensity. Since the whole slit width must be illuminate with a common intensity a beam expander is needed. However during initial calibration tests using lasers it was concluded that it was difficult to obtain an even light intensity by use of beam expanders. If the light intensity in the spectral direction of the slit is not even the true peak centre will be displaced at the CCD. It was therefore concluded lasers were not an optimal calibration source in this case. Ordinary halogen or tungsten lamps in combination with interference filters can also be used for spectral calibration. However temperature, filter angle, and aging variations should be taken into account (Herrala and Voutilainen 1994). G. Polder and G.W.A.M. Heijden (2001) concluded gas excitation lamps were best suited for spectral calibration compared to narrow band filters and a fluorescent lamp. Thus gas excitation sources will be used to calibrate the VTTVIS in the following example.

The spectral calibration procedure is:

1. Select gas excitation lamps to span the whole spectral range of the VTTVIS evenly with calibration peaks
2. Perform at least 5 measurements of each lamp using similar setup as for the axis alignment procedure
3. Record at least 5 darkframe images with exposures similar to the exposure used for each of the gas excitation lamps used. Calculate the median dark current for each pixel and exposure
4. Subtract the median darkframe image from each of the images of the gas excitation lamps. Add a counter offset of 100 preventing negative intensity counts. Calculate the median image for each of the calibration lamps
5. Locate symmetrical peaks with a horizontal baseline. Look up the specific wavelength for each selected peak using e.g. CRC Handbook of Chemistry and Physics (Weast and Astle 1982)
6. Perform moment analysis for each of the selected peaks for all spatial pixel rows estimating the position of the peak centre position at CCD array
7. Fit a 2nd order polynomial through the peak centre position across the spatial axis for each of the selected gas excitation peaks. Use the peak centre positions based on the 2nd order polynomial fit in the spectral calibration in order to reduce noise
8. Depending on the number of selected peaks and their distribution within the spectral range of the VTTVIS perform a 1st, 2nd, and/or a 3rd order polynomial fit through the estimated peak positions for each of the spatial rows
9. Study the residual plot and excluded clear outliers if necessary
10. Optionally, a global calibration model can be developed

In the following an example is given of the practical use of the spectral calibration procedure described above.

5.3.1 Spectral calibration using Hg, He, Cd, and Neon lamps

The gas excitation lamps used in this example were kindly lent of Ph.D. Peter Snoer Jensen at the Department of Optics and Fluid Dynamics, Risø National Laboratory, Denmark. The gases used were Mercury (Hg), Neon (Ne), Helium (He), and Cadmium (Cd). The gas excitation spectrum for each of the gases was found in the CRC Handbook of Chemistry and Physics (Weast and Astle 1982).



Figure 65: Setup measuring the light from gas excitation lamps.

5.3.1.1 The measuring setup

All measurements were performed in a darkened room at AgroTechnology, KVL, Denmark. Initially the lamp was placed right in front lens of the VTTVIS. However the irradiation entering the CCD was then far too high. Therefore the lamp was placed above/behind the front lens of the VTTVIS illuminating a white panel with a reflectance of approx 100% in visual range. The reflected light from the panel was then measured by the VTTVIS. The exposure needed was between 3.6 to 54 seconds depending on the lamp used.

5.3.1.2 Pretreatment of the data

For each lamp 5 measurements were done with common exposure for each lamp. After all lamps had been measured 5 darkframes were recorded for each exposure used. The median darkframes was subtracted all the lamp measurements according to their exposure. Then a counter offset of 100 was added preventing negative counts. The median image for each lamp was then calculated. The median is used since it gives more reliable estimates compared to mean.

By visual inspection the distinct peaks were located for each lamp. The peak should be close to symmetric and reach the base line at both ends. Due to the very high SNR caused by the long exposure peaks with a count as low as 300 (out of a max of approx 45000) could be used. The wavelengths for the peaks were located by use of CRC Handbook of Chemistry and Physics (Weast and Astle 1982). If the registered peak consisted of several narrow peaks a weighted average was calculated based on their expected intensities. The excitation spectra registered by VTTVIS for each of the lamps plus the selected peaks and their wavelengths are shown in Figure 66.

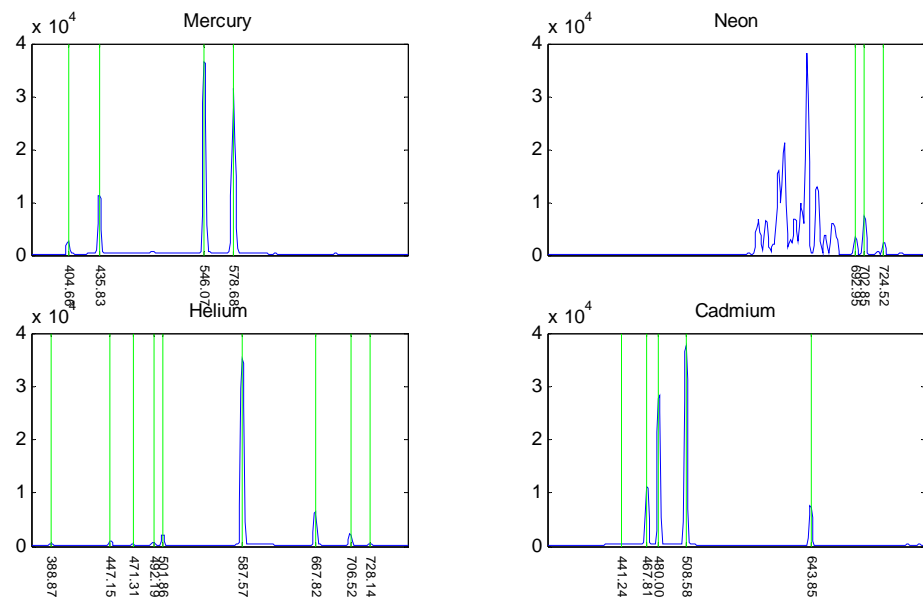


Figure 66: The spectra and selected peaks for each of the 4 gas excitation lamps. The locations of the peaks are indicated with green vertical lines and the specific wavelength is given below each of the peaks.

The center of each peak was estimated by use of moment analysis briefly described earlier.

5.3.1.3 The results after using moment analysis for the peak centre positioning

For each of the 242 spatial pixels rows the pixel location in the spectral column direction was estimated for each of the peaks for the four lamps. The estimated locations are illustrated for Helium in Figure 67. In order to reduce noise a 2nd order polynomial is fitted through the 242 peak locations for each of the selected peaks.

Studying the curvature of spectral peak location in the spatial direction indicate that the moment analysis has difficulties detecting the curvature of weak peaks like Cadmium at 441.24 nm and Helium at 728.14 nm. Due to the degree of the potential error and the potential benefit when included in the spectral calibration using a 3rd order polynomial fit these peaks will not be excluded. At approx. pixel location 22 there seems to be a small offset toward a higher spectral pixels location. A reason for this could be that the entrance slit of the PGP element is narrower at this particular point at the blue end of the slit.

The axial alignment is not perfect studying Figure 67 since the spectral pixels position of the perimeter spatial pixels rows is not equal. Subtracting the spectral peak position for the spatial pixel row 242 from pixel row 1 shows the CCD image plane is rotated approx. 0.6 pixels in relation to the PGP image plane.

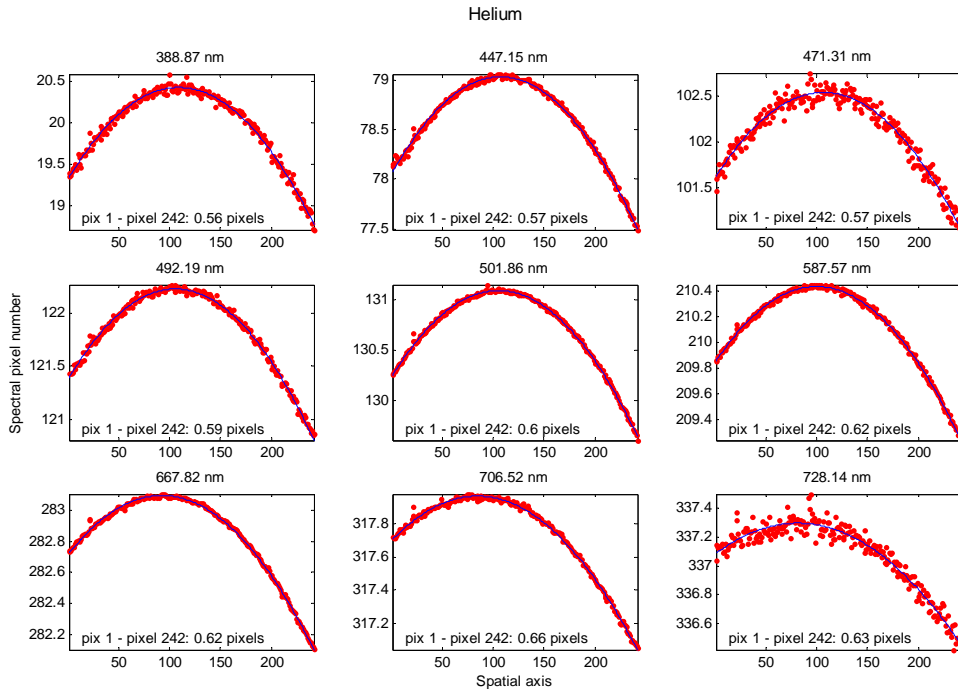


Figure 67: Spectral pixel location of the selected Helium peaks for each of the 242 spatial pixel rows. Furthermore the difference in pixels in the spectral direction between the peak location at spatial pixel row 1 and 242 is given. The blue line illustrates a 2nd order curve fit through the peak locations.

5.3.1.4 The spectral calibration for each of the 242 spatial pixel rows

For each of the 21 selected peaks their spectral pixel location were estimated based on the 2nd order polynomial fit through the 242 spectral peak locations. These 21 spectral pixels location were then used for an individual spectral calibration of the 242 spatial pixel rows. 1st order, 2nd order, and 3rd order polynomial fit were performed. The residual plots are shown in Figure 68 and they show a clean pattern in the residual for the 1st and 2nd order fit similar to Figure 40 on page 42 and Figure 52 on page 56. There is no clear pattern for the 3rd order fit and is therefore to be preferred for wavelength interpolation for the pixels within the CCD of the VTTVIS. The residuals are smaller than ± 0.5 nm, which is acceptable considering that the slit is approx. 4-5 nm wide.

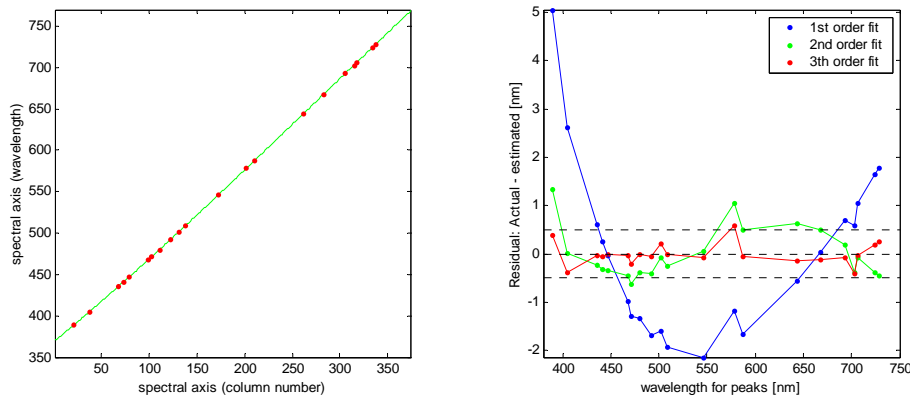


Figure 68: An example of the spectral calibration through the 21 calibration peaks by use of either a 1st, 2nd, or a 3rd order polynomial curve fit for the spatial pixel row number 122. To the right the residuals are shown.

5.3.1.5 A general spectral calibration model for the whole CCD array

By studying Figure 69 (left) and inspired by Equation 7 on page 57 it becomes clear that all the parameters within the third order calibration fit seem to form second order curves in the spatial direction. After fitting a 2nd order polynomial through the parameter values in the spatial direction the residual is shown in Figure 69 (right). The residuals all have a clear systematic pattern but taking the size of the residuals in relation to size of the parameters the error is insignificant in this context. Therefore a general spectral calibration equation can be developed.

$$\lambda = \alpha \cdot C^3 + \beta \cdot C^2 + \gamma \cdot C + \delta$$

$$\begin{bmatrix} \alpha \\ \beta \\ \gamma \\ \delta \end{bmatrix} = \begin{bmatrix} 9.8116\text{E}-13 & -2.9770\text{E}-10 & -6.5582\text{E}-07 \\ -8.5853\text{E}-10 & 2.3084\text{E}-07 & 5.5188\text{E}-04 \\ 9.0865\text{E}-09 & -1.0769\text{E}-06 & 9.5032\text{E}-01 \\ 9.2545\text{E}-05 & -2.0305\text{E}-02 & 3.6996\text{E}+02 \end{bmatrix} \begin{bmatrix} R^2 \\ R \\ 1 \end{bmatrix}$$

Equation 13: Calibration equation for estimation the wavelength, λ , in nm depending on the pixel number in the spectral direction, C , and on the pixels number in spatial direction, R .

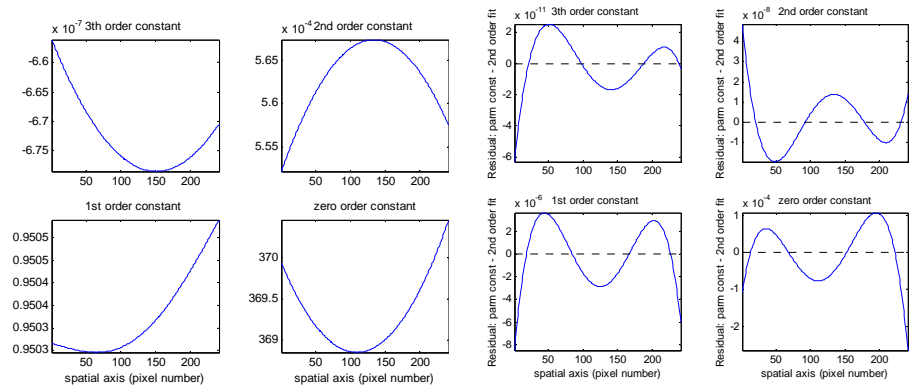


Figure 69: Left: The values of the four parameters used in the 3rd order calibration fit for each of the 242 spatial pixel columns. Right: The residuals for each of the parameters after fitting a 2nd order polynomial in the spatial direction

The difference between the wavelengths estimated by use of the 3rd order fit for each spatial rows number and the global calibration equation given in Equation 13. The difference is less than 1 ‰ of 1 nm and the error introduced by using the global calibration equation is therefore insignificant.

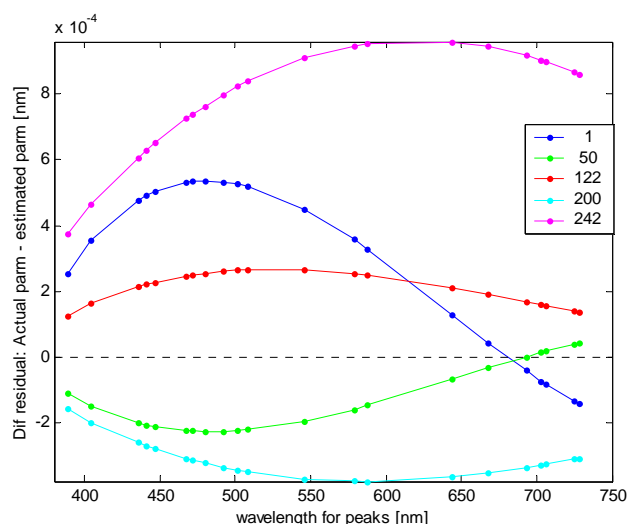


Figure 70: illustration of the difference between the wavelengths estimated by use of the 3rd order fit for each spatial rows number and the global calibration equation given in Equation 13. The difference is shown for the spatial pixel row number 1, 50, 122, 200, and 242.

5.3.1.6 Discussion and conclusion

The spectral calibration using four gas excitation lamps gave 21 calibration peaks distribution in the whole range of the VTTVIS. Due to the long exposure, the cooled CCD, and a 16-bit resolution peaks with intensity counts as low as approx. 300 could be used in the spectral calibration. The bending of the spectral lines in the spatial direction seems to be similar in size or perhaps a little smaller comparing Figure 67 on page 77 the results from the ray tracing in Figure 54 on page 58 when considering a pixel is 23 μm in the spectral direction. A direct comparison is difficult since the CCD was rotated approx 0.6 pixels in relation to the image plane of the VTTVIS. The residuals of the spectral calibration in Figure 68 had a similar shape and size as the ray trace results in Figure 52 on page 56. The size of the error of linearity fitted well with results from an earlier measuring report and with literature using the VTTVIS (the commercial name Inspector V7) (Hagman 1996; Herrala et al. 1994b; Polder and van der Heijden 2001). Due to the number of calibration peaks it was possible to fit a 3rd order polynomial to obtain accuracy much less than ± 0.5 nm except in the perimeter spectral range below 400 nm and greater than 725 nm. However, such accuracy is more than enough taking the slit width of 80 μm into consideration.

5.4 Spectral calibration based on the sun

Calibration procedures using gas excitation peaks are both labour and time consuming and under field conditions not applicable. Therefore an algorithm for both spectral verification and calibration under field conditions was developed based only on measurements of the solar spectrum.

In this section the basis will be developed for performing a spectral calibration of the VTTVIS only based on measurements of the solar spectrum. The idea is to use the local minima, which exist within the visible range solar spectrum due to Fraunhofer atomic absorption lines, water, oxygen, ozone, and aerosols absorption lines. When the exact wavelength for each of these local minima

have been determined it will be possible to develop an algorithm capable of performing a spectral calibration solely based on measurement of the solar spectrum.

5.4.1 Measurement setup

After the spectral calibration using gas excitation lamps described in the previous section 15 solar spectra were measured with the LISS system (see R.N. Jørgensen and P. Rasmussen (2002)) set to auto-exposure and darkframe subtraction as shown in Figure 71left. The potential bias due to dust at the white bar was minimized by moving the bar randomly between each measurement. In order to minimize the effect of varying irradiation intensities during the measuring session all pixels within each image was divided with the mean intensity count of the whole image. Hereafter the median of the 15 replicates was calculated for each of the 242 x 375 pixel giving a median image as shown in Figure 71 – right.

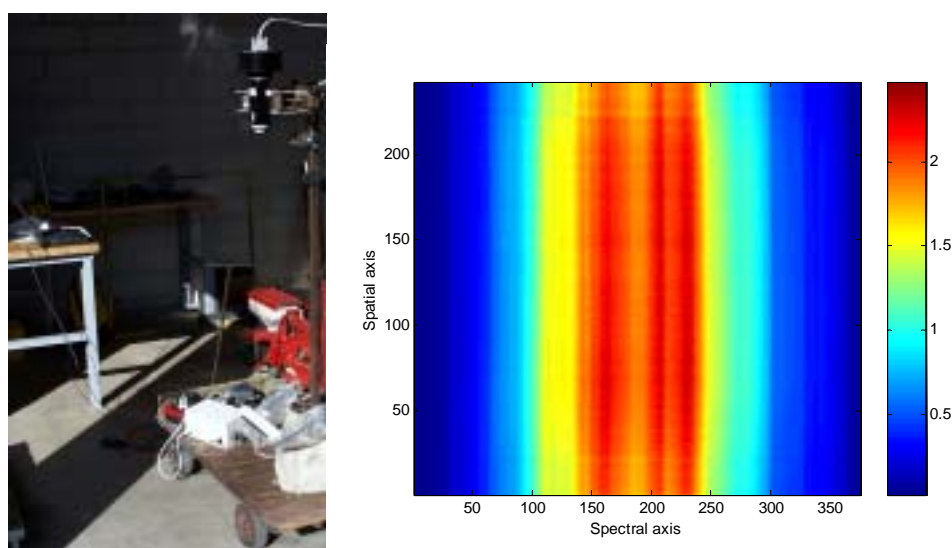


Figure 71: Left: The setup measuring the 15 solar spectra with the VTTVIS. Right: The median of the 15 solar spectra images after each image has been divided with the mean intensity count of the whole image.

Note that the intensity counts for the spatial pixel row number 22 have smaller intensity counts in the whole spectral range compared to the neighbouring rows. This has also been noted earlier in this documents during the spectral calibration using gas excitation lamps.

5.4.2 Noise reduction and estimation of local minima

Further noise reduction was searched obtained by taking the median of 11 successive spectra in the spatial direction giving 22 median spectra. Based on these the derivative spectra were estimated by use of the Savitsky-Golay 2nd order smoothing and first derivative with a window width of 3 pixels (see Figure 72). The Savitsky-Golay smoothing filter was developed by A. Savitzky and M.J.E. Golay (1964). The minima are placed where the derivative shift from a negative value to a positive value. The exact location where the derivative cross with the zero line was estimated by use of linearly regression between the two latter points. Then based on the calibration obtained in the previous section the wavelengths for each of the local minima were estimated.

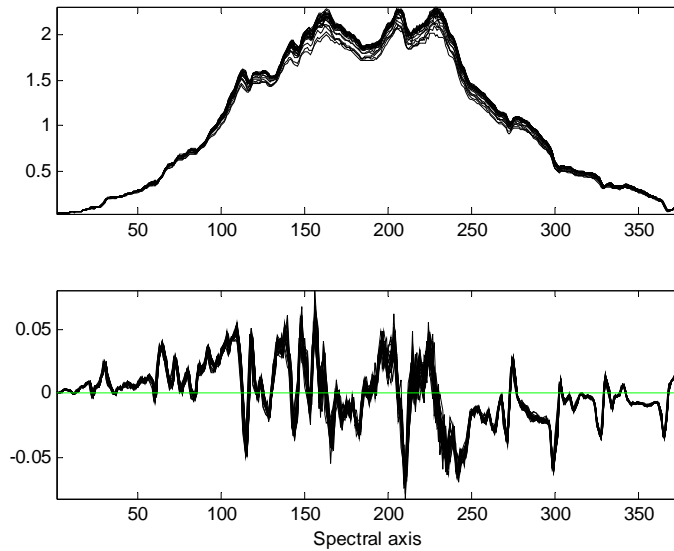


Figure 72: Top – The median spectrum of 11 successive spectra in the spatial direction giving 22 median spectra using the whole width of the spatial axis. Bottom – The derivative spectra of the spectra above by use of the Savitsky-Golay 2nd order smoothing and first derivative with a window width of 3 pixels (Savitzky and Golay 1964).

5.4.2.1 Locating common local minima

Within each of the 22 median spectra all local minima have now been found and their wavelengths have been estimated. The next procedure is to locate minima, which are common to all 22 median spectra. This is done in two steps as described below:

1. Within each spectra all local minima less than 5 nm apart are removed
2. Common minima present within all 22 median spectra and less than ± 0.5 nm apart from each other across the spatial direction are accepted. The rest is removed

The result of the procedure is shown in Figure 73 showing that it has been possible to locate 11 local minima within the solar spectrum, which do not vary more than ± 0.5 nm across the 22 median spectra. Luckily the 11 local minima are spread fairly even in the whole range of the VTTVIS. Figure 74 shows the difference between the median wavelengths of the specific common local minima minus the wavelength of the minima of the median spectra. There is a systematic trend in peak number 4 and 5 but else the difference seems noisy. The trend of peak 4 and 5 is opposite each other and they will probably therefore even out the bias in the spectral calibration to some extent.

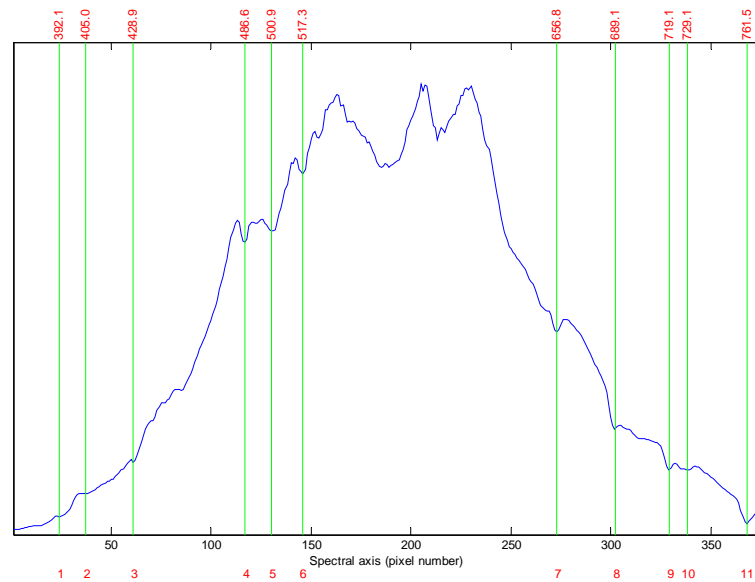


Figure 73: Common local minima for the 22 median spectra, shown in Figure 72, which are less than ± 0.5 nm apart from the median wavelength across the 22 median spectra. The median wavelengths for each of the local minima are written in red at top of the figure.

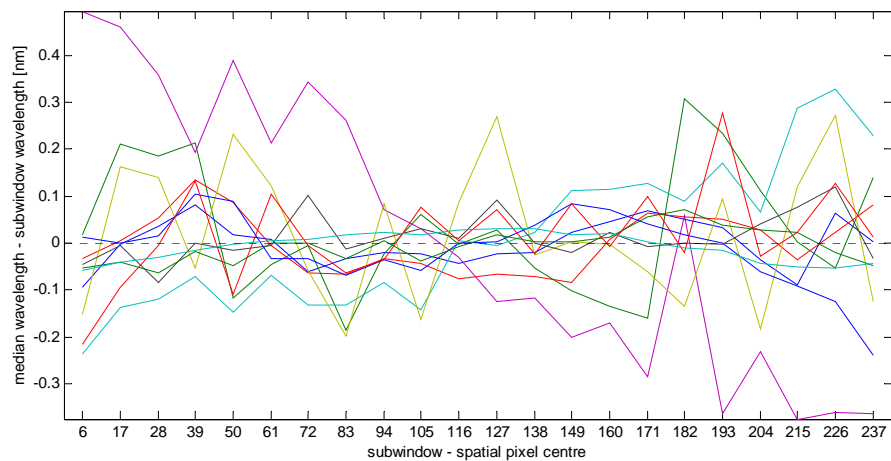


Figure 74: The center spatial pixel position of the 22 median spectra versus the difference between the median wavelength of the specific common local minima minus the wavelength of the minima of the subwindows. The red numbers to the right shows the number of the local minima showed in Figure 73.

5.4.3 Developing the solar calibration procedure

In section 5.4.2.1 the basis for a calibration procedure solely based on the solar spectrum was created. The measuring and preparation of the median solar spectrum is similar to section 5.4.1 and section 5.4.2. However the procedure for locating common local minima has altered slightly, due to the fact that the specific wavelengths are obviously not known. The two steps locating the common local minima are now based on the difference in pixels instead of wavelengths. Consequently in order make the procedure work rotational error of the CCD camera mounted on the PGP element should be minimized. The spectral bending across the spatial axis cannot be taken into account and the

procedure locating the local must therefore be less strict. The two steps to locate minima, which are common all 22 median spectra, based on pixels are:

1. Within each spectra all local minima less than 5 pixels apart are removed
2. Common minima present within all 22 median spectra and less than ± 2 pixels apart from each other across the 22 spectra are accepted. The rest is removed

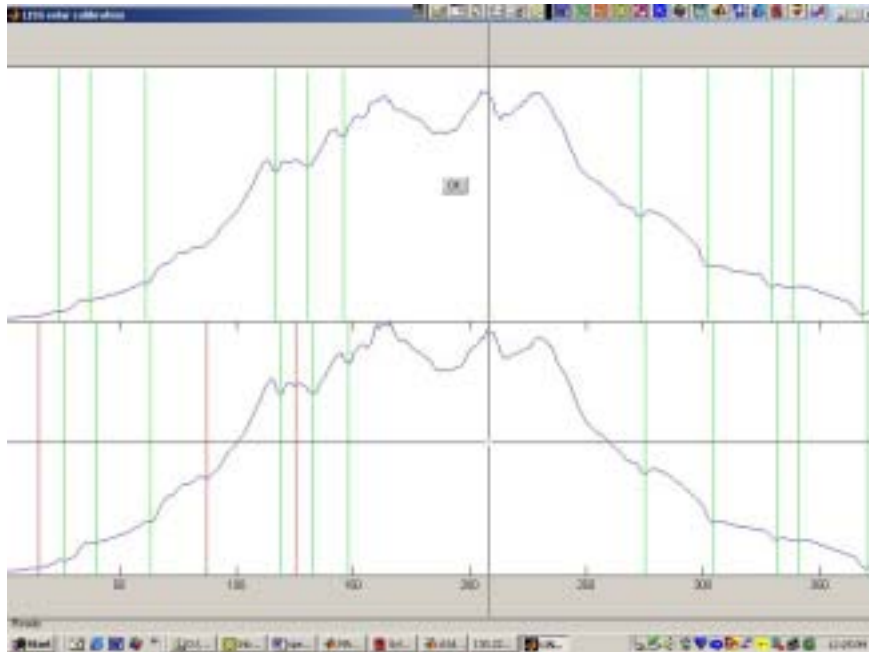


Figure 75: Graphic User Interface (GUI) to deselect local minima not common for the reference solar spectrum (top) and the target spectrum (bottom) used to calibrate the VTTVIS. The hair cross point is used to select/deselect local minima in both the reference and the target spectrum. The green vertical lines are selected/accepted minima and vertical red lines are deselected minima.

In order to secure that the local minima found fits with the reference spectra with the 11 local minima found in section 5.4.2.1. A visual classification or selection is performed by use of a Graphic User Interface developed in Matlab shown in Figure 75. Note the reference spectrum and the target spectrum in Figure 75 are not similar. It seems like there is a shift between the two solar spectra.

When the common local minima between the reference and the target spectrum have been selected the real calibration procedure can be initiated.

5.4.3.1 The final spectral calibration based on the solar spectrum and validation

The procedure is in fact very similar to the procedure described in 5.3.1.4 on page 77. The difference is that the spectral location of the selected minima for each of the 242 spatial pixel rows are now found by fitting a 2nd order polynomial through 22 spectral positions of each the local minima and then perform an interpolation of the peak positions for the 242 spatial rows.

In order to validate the calibration procedure a calibration is performed based on the 15 solar spectra used to develop the basic for this procedure. The GUI is shown in Figure 76 and it can be seen that the spectra in the reference (top) and the target (bottom) windows are similar except for one local minimum in the

target window. This local minimum is deselected and the spectral calibration is initiated by pressing the OK-button.

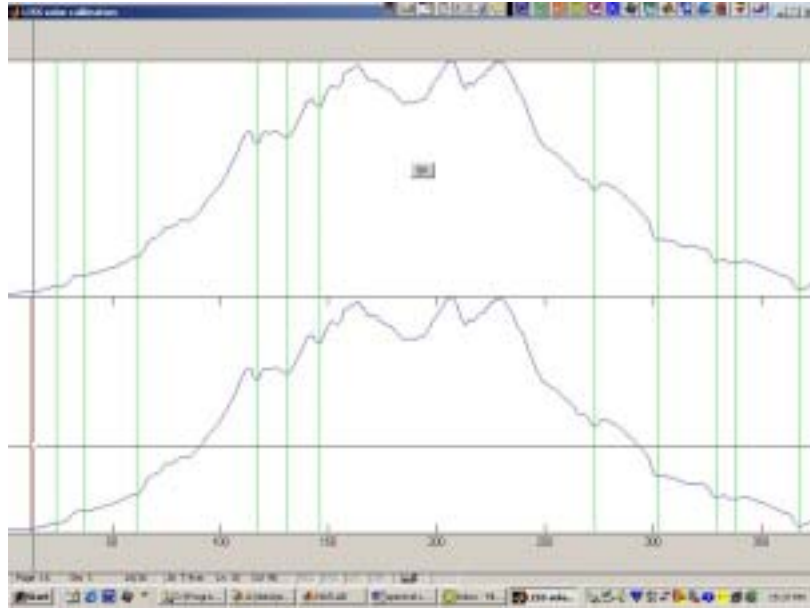


Figure 76: GUI used for the validation calibration using the reference spectrum. This is also the reason the spectra are similar.

The difference between the reference wavelengths and the estimated wavelengths using 1st, 2nd, and 3rd order polynomial curve fitting for the spectral calibration are shown in Figure 77. For the third order curve fit the difference is between ± 0.4 nm depending on the spatial row number. In fact the difference is ± 0.1 nm if the two local minima around 490 and 500 nm were excluded. As mentioned earlier in 5.4.2.1 these two peaks (number 4 and 5 in Figure 73 and Figure 74) have a systematic error pattern in the wavelength estimation depending on the spatial row number. However, since this error pattern seems work opposite each other the two local minima helps stabilizing the 3rd order spectral calibration and were therefore not be excluded.

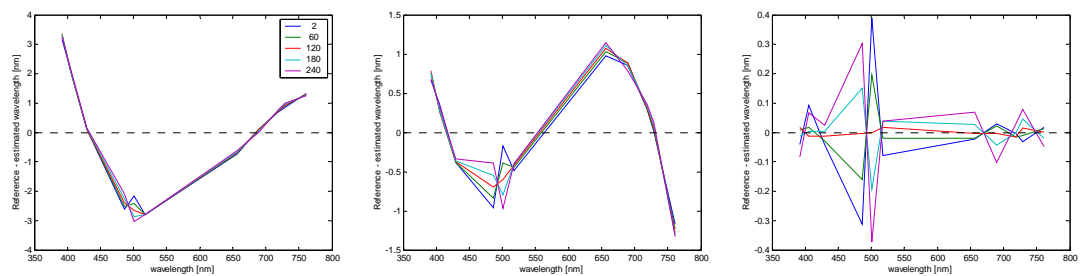


Figure 77: Residual plots between the reference wavelengths and the estimated wavelengths using 1st (left), 2nd (middle), and 3rd (right) order curve fitting for spectral calibration in nm.

By use of Equation 13 on page 78 the residual difference between wavelengths based directly on the gas excitation lamps calibration and the calibration based on the solar spectrum can be compared. The difference has not surprisingly a systematic pattern. However a difference of approx ± 0.25 nm in this context is relatively small.

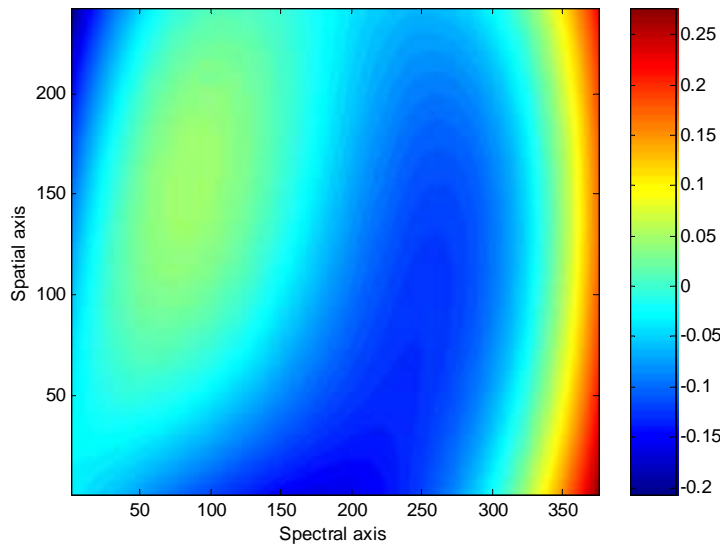


Figure 78: Residual difference between wavelengths based directly on the gas lamps calibration and the calibration based on the solar spectrum in nanometer.

5.4.4 Discussion and conclusion

Initially the spectral calibration based on the solar spectrum was tried by fitting the absorption wavelengths known from literature to the local minima within the solar spectrum measured by VTTVIS. However this calibration differed significantly for the calibration based on the gas excitation lamps. The procedure developed above overcomes this problem by locating the exact wavelength of the local minima using the spectral calibration based on the gas excitation lamps. The potential error in the spectral calibration summing the residuals from Figure 68 on page 77 and from Figure 78 will still not exceed approx. ± 0.5 nm. The procedure used for spectral calibration based on measurements of the solar spectrum seemed to be relatively robust to noise. Even with only one measurement of the solar spectrum the calibration result did not differ much from the calibration based on replicate measures. It can therefore be concluded that the procedure developed will be a valuable tool for verifying and calibration of the VTTVIS under field conditions. Even under laboratory conditions the procedure can be used as a fast reliable calibration of the VTTVIS.

With a single measurement of the solar spectrum it is now possible to perform a spectral calibration of the VTTVIS with an accuracy at least as good as using a second order polynomial fit based on 21 known gas excitation peaks comparing the residuals in Figure 68 on page 77.

5.5 Hyperspectral flat-fielding of the CCD array

The purpose of the hyperspectral flat-fielding is to obtain uniform sensitivity of the pixels in the spatial direction for each of the spectral pixel columns discussed briefly in section 3.4.2.6 on page 34. This is a necessity because the reflection is calculated as the ratio between the object pixels and gray plate pixels as shown in Figure 9 on page 13.

It should in theory be possible to even out the different pixel responsively by use of a light source with a known spectral composition. In lack of such a source alternatively a light source without any peaks and with a constant output should be sufficient. All lamps that work on the incandescence principle, whether conventional or halogen-filled, have a black-body (continuous) spectrum and therefore a color rendition index (CRI) of 100%. The CRI tells how close the spectrum is to a black-body spectrum, and the color temperature tells you what temperature (and therefore color) of black body it would be if it was one. The color temperature depends on what regime the lamp runs in. If a lamp is dimmed it will move the temperature down and therefore the spectrum towards the red. All practical incandescent bulbs are reddish, the lower-wattage ones redder than higher-wattage ones. They are all also relatively inefficient (i.e. produce more heat for a given amount of light). It is possible to get incandescent bulbs with built-in filters to make them bluer (and raise the effective color temperature). These are even more inefficient, since all a filter can do is convert some of the (unwanted) light into heat.

For this project a conventional 5-watt incandescent lamp was initially selected knowing that light intensity was probably too weak in short wave range of the VTTVIS. Further it is important that the illumination level is uniform over the whole area of the object line. The Department of AgroTechnology at KVL, Denmark, has a homemade integrating sphere capable of creating a circular area of uniform illumination from the latter lamp.

5.5.1 The measuring setup and data pre-treatment

The setup and the homemade integrating sphere are shown in Figure 79. Just by looking at the color of the light coming out of the sphere it seems to be a rather cold or reddish color temperature consequently with very small amount of blue in its spectrum.

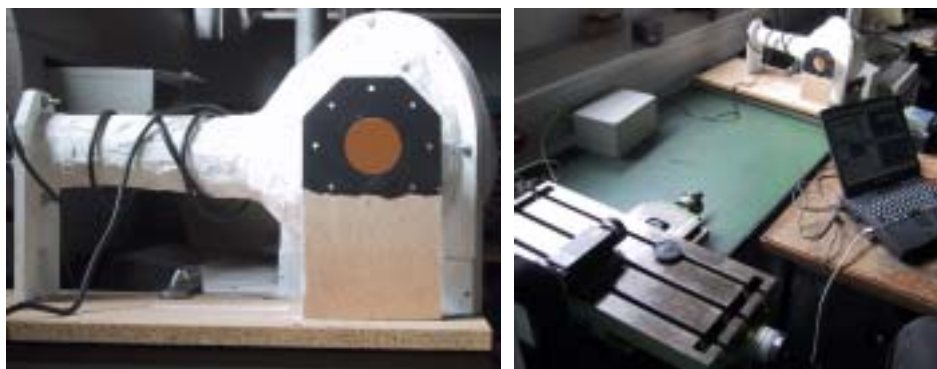


Figure 79: The setup for collecting measurements use to hyperspectral flat-fielding. Left – The homemade integrating sphere at the Department of AgroTechnology at KVL, Denmark. Right – The stepper table mounted with the VTTVIS pointing towards the outlet of the integrating sphere.

The width of the outlet from the sphere was narrower than the measuring line of the VTTVIS, which was approx. 200 mm. Therefore the measurement was done stepwise and then merged together. The distance from the lens to the sphere inlet was approx 112 cm ensuring the object line at the sphere wall was out of focus. When the measurements were done the room was kept dark. In order to fill the wells of the CCD approx. to a maximum of 70% an exposure of 8.2 seconds was needed. After the measurement had been done 15 darkframes were recorded with the same exposure. Prior to any work on the raw data from

the measurements of the sphere the median of the 15 darkframes was subtracted pixel wise.

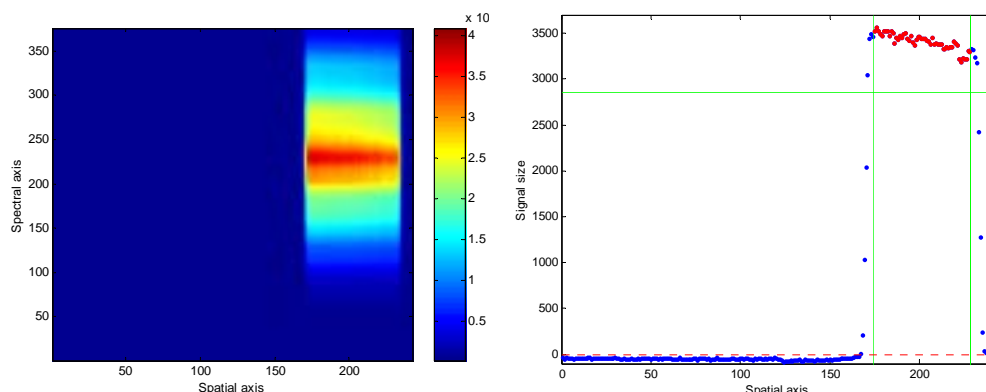


Figure 80: Left - An example of a single measurement with the VTTVIS of the outlet of the integrating sphere. Right - Schematic illustration of the criteria for selecting the area of the integrating sphere outlet. The horizontal green line is 80% of the maximum signal. The vertical green lines enclose the spatial pixel columns selected used as flat-fielding pixels columns. The negative signals are because there seems to be a small offset error of the median darkframe subtracted the raw data.

Measurements were collected moving the VTTVIS in steps of approx. 1 cm. When the full width of the slit had passed the sphere outlet the sphere was angled a little and a new stepwise measuring session was done. This was repeated 4 times.

Figure 80 shows the principles of the selected the spatial pixel columns belonging to the outlet of the sphere. There seems to be an introduction of an offset error when subtracting the median darkframe since negative values are present. This problem is also mentioned in the users manual for the SBIG CCD camera at page 62 (Santa Barbara Instrument Group 1993a) and is called underflowing. They solve the problem by adding a bias of 100 counts to the images, which will also be done in this case. The number of replicates for each pixel summed to between 17 and 22 measurements.

5.5.2 Results and discussion

Studying Figure 81D it is clear that the amount of light entering the VTTVIS is very small in the short-wave range. Further there seems to be an overall change in the signal intensity from the slit centre towards the perimeters of the slit. However this overall change is not uniform but is highly dependent on the spectral column or wavelength. Moving from the short wave range toward the long wave range of the CCD the shape of the signal across the spatial axis changes gradually from a concave shape to a convex shape as illustrated in Figure 81 B & C and Figure 83 A. The change is summarised by plotting the 1st and the 2nd order parameter from a 2nd order polynomial approximation for each of the 375 normalised curves as shown in Figure 82 left. Dividing with the mean signal count of each column across the spatial axis did the normalisation for each of the spectral columns. The shift from concave to convex happens at spectral column 59 where the 2nd order parameter shifts from a positive value to a negative. The reason is not clear but below 400 nm or spectral column 34 almost no light reach the CCD due to a very small transmission efficiency of the lenses used in the VTTVIS system of course combined with irradiation level of the lamp. Studying Figure 82 left changes occurs until approx. spectral column 75 where the shape of normalised signal count across the spatial axis seems to

stabilise. The stabilisation is probably due to the light intensity or pixel signal count has reached a level where the voltage of the CCD is proportional with the signal.

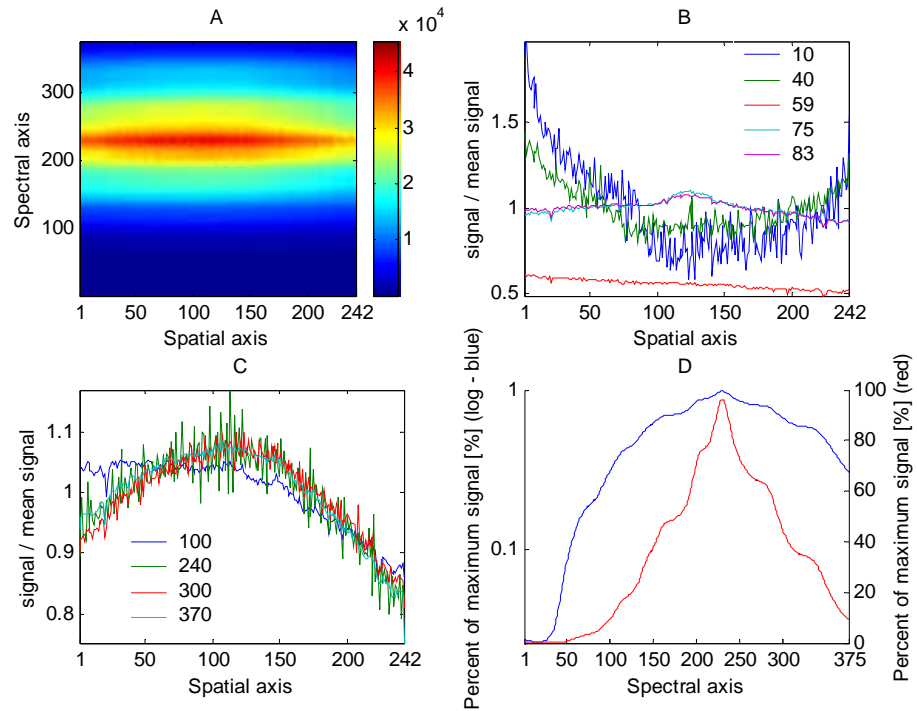


Figure 81: Graphically summary of the hyperspectral flat-fielding. A – Image showing the median signal minus the darkframe plus a bias of 100 counts. B – normalized signal for each spatial pixel rows along the spectral axis shown for the spectral pixel column numbers given by the legend. Dividing with the mean signal count of each column across the spatial axis did the normalisation for each of the spectral columns. C – The same as for B but different spectral pixel column numbers. D – The average normalized signal strength in percentage of maximum along the spectral axis shown in logarithmic scale with blue and normal scale with red.

From spectral column 75 to 84 an abnormal increase in the signal count occurs in between spatial pixel row 110 and 140. The reason for this increase is not known but it adds prove to the fact that there is systematic patterns or bias, which should be taken into account before estimating measured object reflectance.

During the analysis it seemed like significant noise was introduced to the signal count when it passed a certain threshold level towards large signal counts. The raw data visualising the transition from low noise to high noise is shown in Figure 83 C and D for the blue and red end of the CCD where the signal counts were still relatively small in relation to the bit range of the CCD.

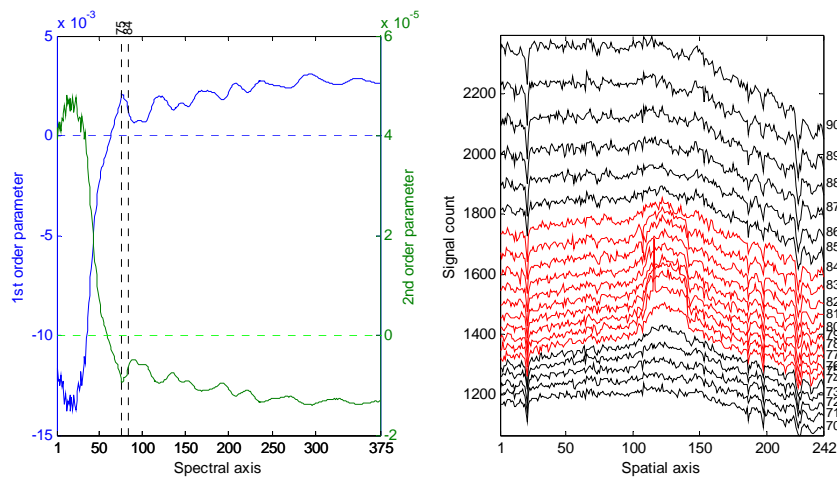


Figure 82: Left – Illustration of the 1st and 2nd order parameters from a 2nd order polynomial approximation across the spatial rows for each of the 375 normalised spectral columns. The vertical lines shows the spectral columns shown with red in the subplot to the right. Right – The signal count across the spatial axis for spectral columns 70 to 90. The red lines show a range of spectral pixel columns from 75-84 (~436-445 nm) where shapes are abnormal between spatial pixel row 110 and 140.

A strait forward way to visualise signal dependent increase in the variation would is to plot the standard deviation versus the mean signal each of pixels within the CCD. This would however create a confounded picture of the noise from within the whole VTTVIS system mixed with the spectral characteristics from the illuminator illustrated in Figure 81D.

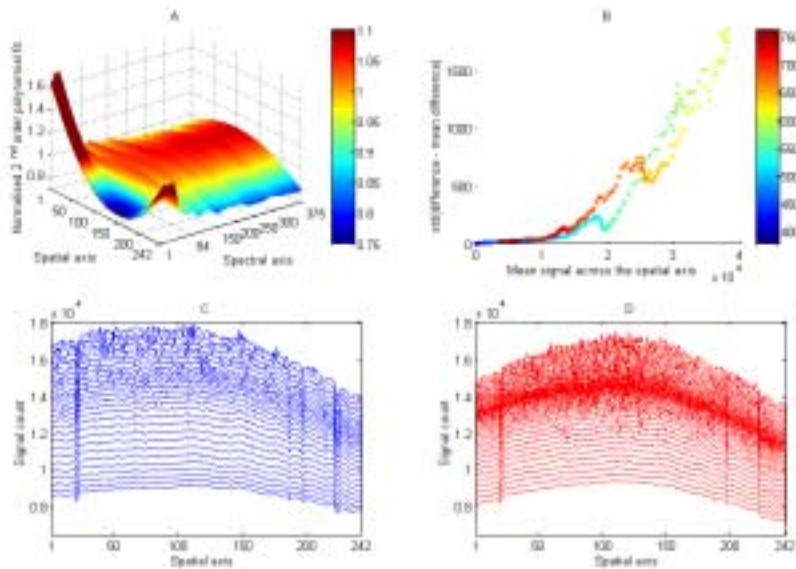


Figure 83: A – Illustration of normalised signal response based on a 2nd order polynomial fit across the spatial axis for the 375 individual spectral columns. B – The standard deviation of difference between spectral column i and $i+1$ across the spatial axis subtracted the mean of the latter differences versus the mean signal for each spectral column. The colorbar indicates the approx. wavelength of the spectral column in focus. C & D – Illustration of the increasing noise across the spatial axis as the signal count increase from spectral column 130-155 (C ~ blue) and a decrease from spectral column 305-350 (d~red).

The bias due to the lamp the VTTVIS system (e.g. due to variations in the slit width and vignetting) was minimised by using the difference between neighbouring spectral columns (spectral column i – spectral column $i+1$) across the spatial axis subtracted the mean of the difference within each difference column. The result is illustrated in Figure 83B. The noise level seems to be almost constant up till a mean signal count of approximately 11000 for signals registered both in the blue and the red end of the CCD.

If considering Figure 83B as a photon transfer graph by changing both axes into the logarithmic scale as shown in Figure 84 some interesting characteristics turns up. Further, if considering the photon transfer characteristics briefly discussed in section 3.4.2.11 on page 37 then the photon transfer curve can be recognised in Figure 84 as illustrated with the black solid line. The noise floor regime with a zero slope exists up till a mean signal count of approximately 2000. Hereafter the shot noise regime with a slope of $\frac{1}{2}$ continues up till approximately a mean signal count of 11000. If accepting Figure 84 as a kind of photo transfer curve then the steep part of the curve for mean signal counts ≈ 11000 should be associated with fixed pattern noise or PRNU with slope 1. However the slope illustrated with the punctuated line is approximately 1.5. This is greater than slope 1 as for the conventional photon transfer curve a log-log space. An increasing slope in the log-log space is equivalent with an increase in the power the noise is developing with depending on the signal count. Hence the standard deviation is developing with the power of 1.5 (e.g. $\log(x^{1.5}) = 1.5\log(x)$) which is not proportion with the signal count like in the PRNU case. Thus the greater slope must originate from some additional and unknown error sources, which are increasing faster than a proportional factor depending on then mean signal count. The fact that PRNU is the dominating noise source already at signal counts greater than 11000 agrees with Janesick (2001) who concluded that doped virtual phase CCD's like the SBIG ST-6 CCD have problems with fixed pattern noise like PNRU. Hence the primary noise source at signal counts greater than approximately $13\frac{1}{2}$ bits is probably PRNU for the VTTVIS system.

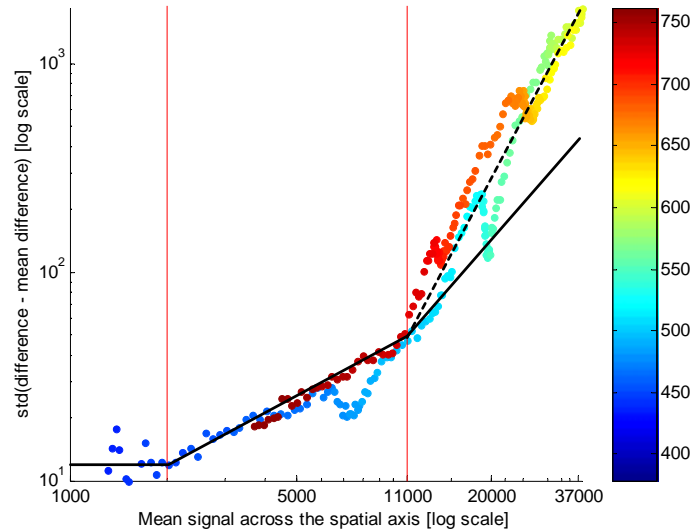


Figure 84: Figure 83B plotted as a photon transfer curve described in section 3.4.2.11 on page 37. The black solid line shows the ideal case of a photon transfer curve. The colorbar indicates the approx. wavelength of the spectral column in focus.

Studying Figure 85 and Figure 81 it is clear that the temperature of the lamp use was far too low. A more appropriate the temperature would have been

approx. 6000 K in combination with a filter optimising the intensity according to the light source and the spectral quantum efficiency of the system.

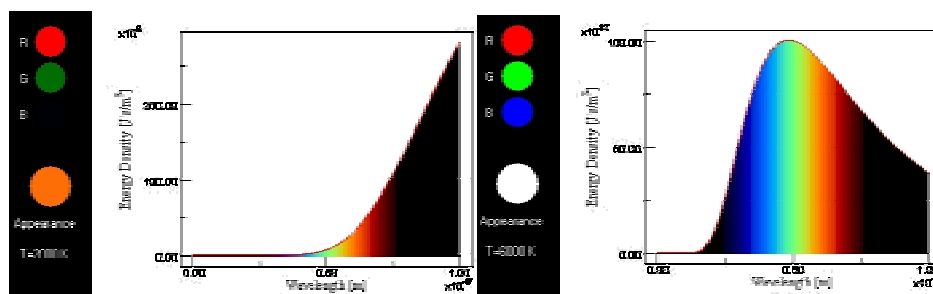


Figure 85: Spectral radiation from a black body at 2000 K and at 6000 K. (http://cat.sckans.edu/physics/black_body.htm).

Summing up it can be concluded that this initial attempt to perform hyperspectral flat-fielding was not meet. This was due to the use of a too cold lamp but also due to PRNU noise introduced when the signal passed a relatively low threshold of approx. one sixth of the CCD bit range. However, the result clearly shows there is a systematic pattern in the response of the VTTVIS system especially across the spatial axis. The bias should be minimised prior to any analysis. It is particularly important to remove this bias where the reflectance across the object line is based on irradiating estimates based grey plates placed in the perimeter of the object line as illustrated in Figure 9 on page 13. However, further investigations are needed to obtain a reliable model removing the system bias within the VTTVIS.

5.6 An alternative flat fielding procedure

The hyperspectral flat-fielding procedures did not succeed in the previous. Thus in the following a simple procedure for use under field conditions will be described reducing the bias in the response significantly.

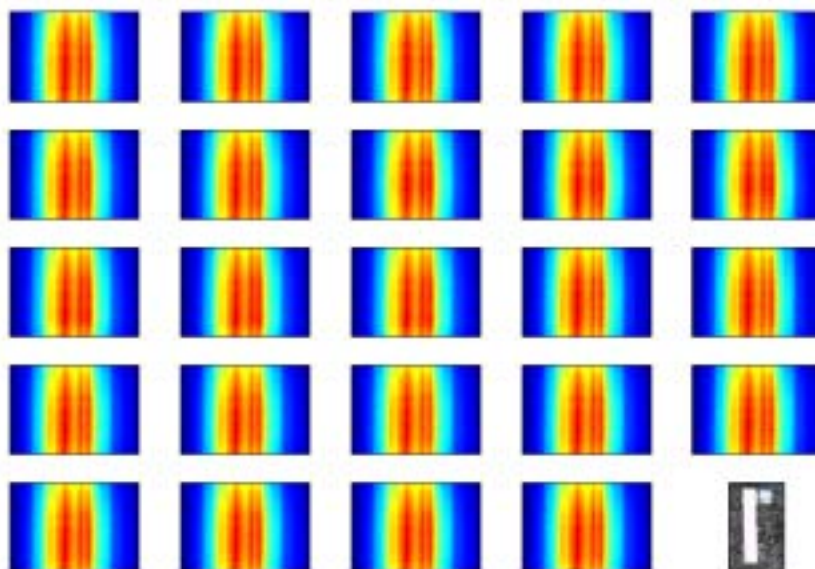


Figure 86: Normalized images of a white optical grade SpectralonTM used to reduce the systematic variation in the response across the object line (vertical direction 1->242). The horizontal direction contains the 375 spectral pixel columns.

Before and after a measuring session approximately three measurements were collected of a 99% white Spectralon™ panel during the growth season 2001. In order to minimize the effect of varying irradiation levels and exposures each pixel signal count were divided with the average signal count for the whole image. The result of the normalization is illustrated in Figure 86. Note the intensity or color variation in the spatial or vertical direction. Studying Figure 86 it becomes clear that the light sensitivity varies across the spatial object line depending on the spectral column number or wavelength. This phenomenon is illustrated in Figure 87A where 2nd order polynomials have been fitted across the spatial direction for selected spectral columns of the median image. The median image is based on the images in Figure 86. The extremum for each of the 375 2nd order polynomials is located. Hereafter the normalisation is done for the each of the 375 estimated polynomials and the spectral columns in the median image by dividing with the extremum found for each column. Bias still seems to be present studying Figure 87B after subtracting the normalised polynomials vectors from the normalised median image. This residual bias or pattern is assumed to originate from variation in the slit width and other systematic pattern sources. In order minimize the residual bias the median of all the differences illustrated in Figure 87B from spectral column 34 to 365 are estimated. The last detectable bias is the incorporated into the normalised 2nd order polynomial image (see Figure 88A) by adding residual pattern vector (the red line in Figure 87B) to each of the 375 spectral columns.

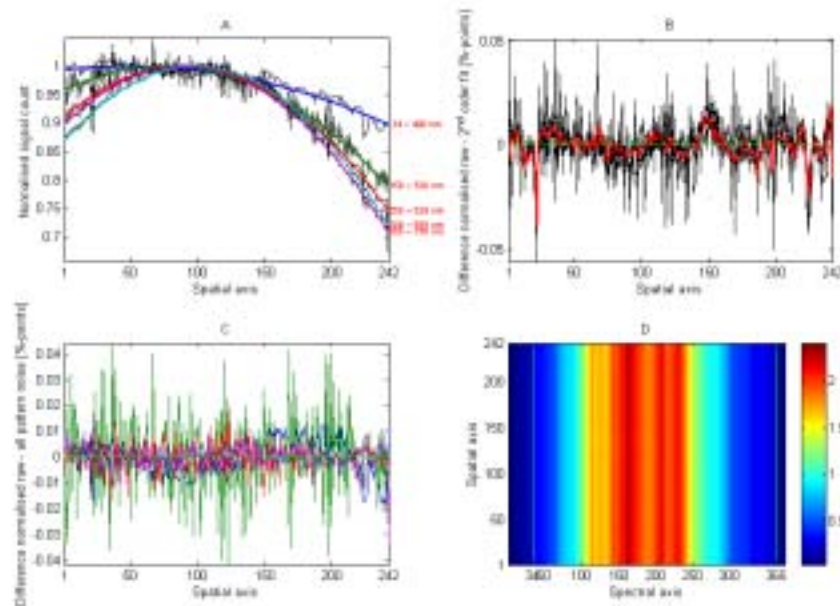


Figure 87:A – Normalised signal count across the spatial axis for selected spectral columns calculated by dividing with extremum of the 2nd order polynomial for each of the spectral columns. The colored lines are the fitted polynomials and the black lines are the normalized raw signal intensity. B – The black lines are the selected spectral columns after subtracting the fitted polynomials from the normalized raw signal. The red line is the median of all the differences from spectral column 34 to 365 revealing residual bias in signal sensitivity across the spatial rows. C – Similar to B but the residual bias has been subtracted. D – The corrected image of the median image estimated from Figure 86. The image has been corrected by dividing with the normalization image taking the 2nd order bias across the spatial axis and the residual bias into consideration (see also Figure 88). The vertical lines enclose the valid spectral range (~400-756 nm) for the VTTVIS system.

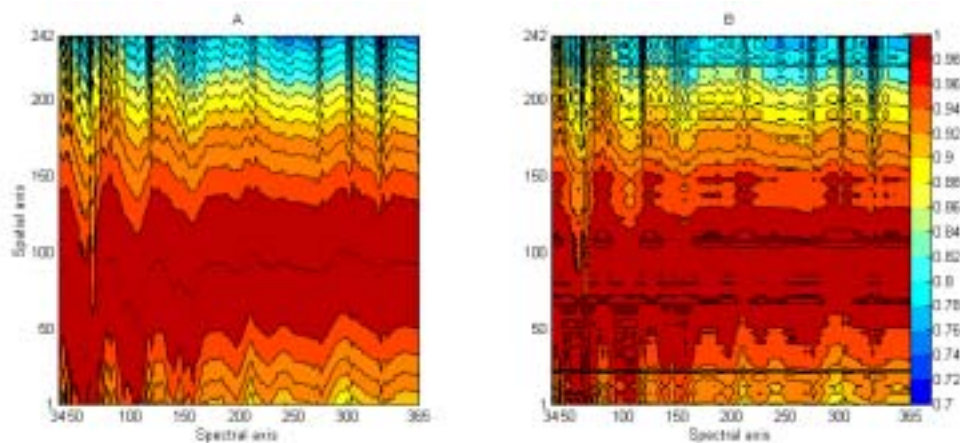


Figure 88: A – Ratio image based the 2nd order polynomial estimates across the spatial axis for correcting bias in the light response illustrated in Figure 87A. B - Ratio image based the 2nd order polynomial estimates plus the residual signal bias across the spatial axis correcting for bias in the light response across the spatial axis illustrated in Figure 87 A & B.

The resulting correction or normalization image is shown in Figure 88B. Thus prior to any analysis of a measured image collected by the VTTVIS the raw image should be divided with the ratio or normalization image in Figure 88B correcting for bias in the sensitivity of the VTTVIS across the spatial axis. It should be noted that this procedure is a second best solution in lack of a proper hyperspectral flat-fielding image. Further it has earlier been noted that the variation across the object line in the light response seemed to differ for low signal counts.

5.6.1 Procedure for estimating a normalization image in brief

Based on the previous description a procedure estimating a normalization image correcting the bias in the light sensitivity of the VTTVIS can briefly be described:

1. Record several (>10) measurements of a white 99% reflecting Spectralon™ panel under natural illumination conditions. Remember to move the panel randomly between each measurement
2. Removed measurements containing overexposed pixels
3. Normalize each image for varying irradiation levels and exposure by dividing the raw image with the mean of the whole image
4. Calculate the median image (im_median) of all the normalized images
5. For each of the 375 spectral columns fit a 2nd order polynomial across the 241 spatial pixels. Note that spatial pixel 242 is excluded because this row has a significant lower light response
6. Find the extremum for each of the 375 polynomials within the spatial range (1-242)
7. Normalise both im_median and the estimated polynomials by dividing with the extrema found in the previous point according spectral column number. This gives a normalized median image (im_median_norm) and a normalized polynomial fit image (im_poly_norm)
8. Subtract im_poly_norm from im_median_norm
9. Calculated the median of the result from point 8 in the spectral direction from spectral column 34 to 365 (~400-756 nm) revealing residual bias in the light response due to e.g. variation in the slit width (im_residualbias)

10. Estimate the final normalization image (im_norm_final) by adding im_residualbias to each of the 375 columns in im_poly_norm
11. Prior to any analysis of the raw images collected by VTTVIS divide the raw image with im_norm_final

5.6.2 Comparison with an earlier normalization image used

AgroTechnology, KVL, has also been aware of the bias in the light responsivity across the spatial axis dependent on the spectral column number. For comparison this normalization image is shown in Figure 89right. When comparing the image with Figure 88B there are similarities. For example the systematic decrease in the values across spectral columns for the spatial rows at approx row number 21 and 220 is common. Further, there seems to be similarities in the large-scale patterns. Still despite of the similarities the two normalization images are very different. The reason for this is not known since the procedure for estimating the “old” normalization image is not known.

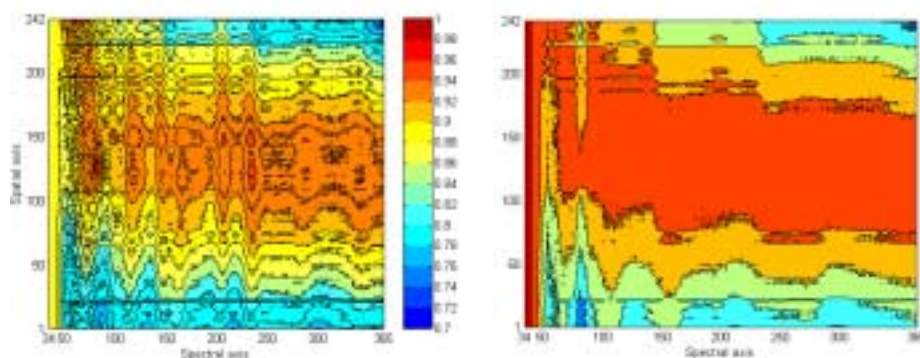


Figure 89: Normalization image earlier used at AgroTechnology, KVL, trying to correct for the bias in the light sensitiveness of the VTTVIS across the spatial axis. Left - The original normalization image has been normalized by dividing with the maximum value within the image. Right – The original normalization image has been normalized by dividing with the maximum value within each spectral column. For spectral column number less than 40 a preset value of 1 has been set due to missing data.

5.7 Procedure correcting PGP image distortion

The extent of the spectral and spatial bending is very limited relative to the CCD pixel scale except for the perimeter pixels. Thus, the demands to the signal quality are very high collecting the empirical basis for straightening up the hyperspectral image projected by the PGP spectrograph. Therefore all other systematic noise patterns should have been removed or minimised prior to this procedure.

The hyperspectral calibration procedure based on the four gas excitation lamps created the basis for a detailed description of the image distortion across the spatial axis. However, the spatial position of projected peaks cannot be extracted from the setup used for spectral calibration. Therefore the distortion of the spatial axis cannot be estimated. A minor change in the setup from the spectral calibration procedure will make it possible to extract both the spectral and the spatial origin of the peaks. By virtually punctuating the object line reflected by the white bar using matte non-reflecting material as shown in Figure 90 peaks separated both spatially and spectrally will be projected at the CCD array.

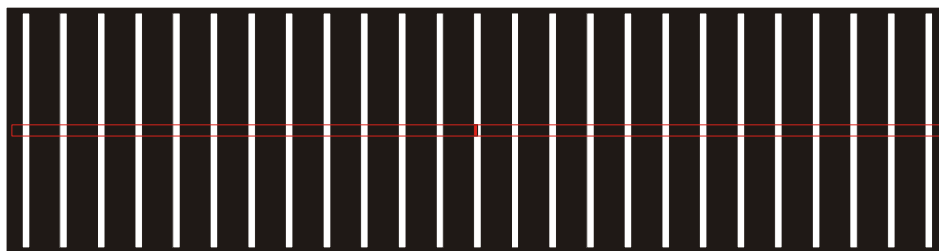


Figure 90: Schematic illustration of the setup for punctuating the object line reflecting the light from gas excitation lamps creating peaks both spectrally and spatially separated. The object line entering the PGP spectrograph of the VTTVIS is pictured as the red rectangle and the filled red square illustrates the left of the two object pixels at the centre of the object line.

The spatial width of the white areas should be approx. 2 pixels wide and evenly separated by a black area several matte pixels wide ensured good peak center estimations both in the spectral and the spatial direction.

The smearing the object pixels described in section 4.2.4.4 on page 60 and narrow-band interference can also have some unforeseen effects estimation of the peak centres.

However, it must be stressed that this procedure is a suggested procedure on how to create the empirical basis for developing a model capable of straightening up the hyper spectra image of the image line projected by the PGP spectrograph. Since several other instrumental problems described in the report have not been solved due to limitations of the VTTVIS itself this suggested procedure should be considered as inspiration and not as the final protocol on how to correct the image distortion.

5.8 Summary

Different adjustment and calibration procedures for the VTTVIS system have been described together with practical examples. By use of a common setup using one gas excitation lamp it is possible perform an axis alignment and an optimisation of the back focal length. By using additionally three selected gas excitation lamps 21 peaks could be located spread evenly within the spectral range of the VTTVIS. The spectral calibration clearly confirmed the spectral bending described in section 4.2.4 on page 54 and the need for separate spectral calibration for the 242 spatial pixel rows.

A third order polynomial described the spectral non-linearity well obtaining a residual less than ± 0.1 nm except for few potential outliers. Inspired by the results from the ray tracing on the systematic patterns in image distortion a relatively simply spectral calibration model was developed capable of spectral prediction for the whole CCD.

The spectral calibration based on several gas excitation lamps is labour and time consuming and new calibration procedure was developed. The new procedure only needed a few measurements of the solar spectrum to obtain a spectral prediction accuracy within ± 0.5 nm which was significantly better than seen in literature using two-piece, 1st order, or 2nd order polynomial fitting. Further, this new procedure enables fast and reliable spectral verification and calibration under field conditions.

The purpose of the hyperspectral flat-fielding was to obtain uniform sensitivity of the pixels in the spatial direction for each of the spectral pixel columns, which is a necessity when estimating the reflection as the ratio between the object pixels and the gray plate pixels placed in the perimeter of the object line. Already from the start it was clear that the light source was too cold

to perform a proper flat fielding. However, the result clearly showed systematic patterns in pixel response across the spatial axis. The relative difference in response between the spatial center object pixels and the perimeter pixels were up till approx 20%. The pattern seemed to depend on either the signal count and/or the wavelength. The weak pattern noise across the spatial axis was only obvious within a narrow signal intensity range between approx 2000 and 11000 counts. This was probably due a large PRNU within the CCD of the VTTVIS system. Thus the usable signal range of the CCD in the SBIG ST-6 camera seems to be only one sixth or $13\frac{1}{2}$ bits of the expected 16 bits range.

Further investigations with a better light source are surely needed to obtain a proper flat-fielding and to investigate the true bit-range of the 16-bit SBIG camera. However, a procedure is described minimising the systematic pattern in the light responsivity across the spatial axis using measurements of reflected light of white optical grade SpectralonTM under natural field conditions.

Due to several instrumental problems described in the report, which has not been solved due to limitations of the VTTVIS itself it was only possible to suggest a procedure on how to create the empirical basic for a model straightening up the hyperspectral image in both the spatial and spectral direction. Thus the suggested procedure should be considered as inspiration and not as the final protocol on how to correct the image distortion with the VTTVIS.

6 Discussion

Several specific subjects have already been discussed within the main chapters of this report with concern to instrument principles, instrument specifications, adjustment procedures, and calibration procedures. This chapter will discuss obtained knowledge from an overall viewpoint extracting the most important points with concern to potential instrument errors and system limitations.

The VTTVIS system consists of relatively few components, which are all fixed with no moving parts inside. This makes the system well adapted to rough environments like e.g. outdoor conditions. This report document however there are several potential error sources within the system itself. These are either random or systematic error sources. The majority of the random error sources originate from the CCD camera and can be minimised by using cooled high-grade cameras.

During the work with report and especially performing the hyperspectral flat-fielding in section 5.5, page 85, the SBIG camera showed to have severe photo response nonuniformity (PRNU) noise problems when the signal count exceeded approx. one sixth of the stated 16-bit range. Thus the SBIG quantification noise seems to be the major limiting factor to the VTTVIS system with concern to noise sources. However, further investigations are needed to prove the origin of the camera noise sources.

The nature of the random noise lowers the contrast between the true signal and the system noise making it harder to obtain significant results. However, replicates can increase the SNR of a signal and more important the result can be related directly to the characteristics of the measurant.

More severe is systematic instrument errors like FPN, PNRU, non-Lambertian reference panels, wrong instrument adjustments and calibrations, and image distortion. These errors cannot be removed by averaging several replicates except in rare cases where for example the systematic errors are random distribution at the CCD. A.G.T. Schut and J.J.M.H. Ketelaars (2001a) had problems with systematic instrument errors since they concluded that their results were probably a combination of sensor characteristics and canopy characteristics. The problem is not specific for A.G.T. Schut and J.J.M.H. Ketelaars (2001a) compared to several other authors using the PGP spectrograph for hyperspectral imaging. The only significant difference seems to be that A.G.T. Schut and J.J.M.H. Ketelaars are aware of the confounding between instrument and measurant characteristics compared to several other authors (see chapter 3.10 on page 49), which either ignores it or is not aware of them.

Based on the ray tracing it was possible to simulate the effect of the spatial image distortion (see chapter 3.7.1 on page 44). At edge conditions measuring a pure leaf object pixel with a pure soil object pixel as neighbour the plant spectrum became increasing mixed with the soil spectrum as distance increases from the central wavelength of the PGP spectrograph (~ 575 nm) and even further with increasing off-axis condition moving towards the slit perimeter. The mixing effect on the plant spectrum in the red area has a significant effect on commonly used indices like red edge, vegetation indices, and normalised difference indices potentially leading to erroneous conclusion if not aware of the spatial image distortion. Thus object pixels within transition zones should either be removed prior to analysis focusing on object characteristics or correction models should remove the image distortion.

But why is it so important to get rid of or counteract for all systematic error sources? The answer seems obvious but is often ignored due to the complexity of

correcting these errors as it also appears reading this report. Measurement results, which are confounded with instruments characteristics, are only true for the specific system configuration and cannot be generalised to cover other systems. This means that a huge amount of scientific results are of limited value when upgrading a system or altering it from an expensive scientific system to a cheap commercial system. Therefore new expensive field trials must be performed from scratch every time systems like the VTTVIS is upgraded or exchanged with new systems. If however the instruments characteristics were well characterised for both the outdated system and the new system prediction models could be transferred to the new system speeding up the model development significantly.

Fixed pattern noise such as dark current and read out noise is relatively simple to remove by subtracting a darkframe recorded under similar condition and settings as the image recorded. Using cooled cameras and darkframe subtraction photoresponse nonuniformity (PRNU) is normally the dominant pattern noise component typically varying $\pm 10\%$ across the CCD array. PRNU is highly spectral dependent often causing narrow band interference patterns. Hyperspectral flat-fielding using a stabilised light source without any peaks can be used to correct PRNU. In chapter 5.5 on page 85 hyperspectral fielding was searched performed for the VTTVIS. However this flat-fielding procedure accounted not only for the PRNU but also for other instrument characteristics causing fixed response patterns. The instrument characteristics causing these patterns were variations in the slit width, changes in off-axis transmission efficiencies, diffraction efficiencies, and CCD charge transfer efficiency. Valuable result were still obtained despite the illuminant used for the hyperspectral flat-fielding was far too cold for the VTTVIS having too small flux intensities in the blue short-wave range in relation to the increasing light intensities toward longer wavelengths. After the pixel signal had passed a minimum count of approx. 2000 a clear systematic pattern showed up across the spatial axis. The perimeter object pixels showed down to 25 % smaller signal compared to largest signal near the centre of the slit or object line as can be seen from Figure 81C on page 88. If it is not possible to produces a proper flat-fielding ratio image a second best alternative is described minimising the systematic pattern in the light responsivity across the spatial axis applicable under field conditions. Thus prior to any reflectance estimation based on the grey panels in perimeter of the object line correction for all fixed patterns in the signal response must be performed.

Having corrected for the fixed patterns in the response the measurement of the grey panels cannot be used directly for reflectance estimation as discussed in chapter 4.5.1 on page 66. While the angular dependence of the panel reflectance of a direct solar beam can be accounted for in terms of the directional-directional reflectance factors, the non-isotropic nature of the sky irradiance makes it difficult to quantify and predict the reflectance of this component. The significance of the sky irradiance component varies with ambient atmospheric conditions and this casts doubt on the validity of using either a directional/directional or directional/hemispherical correction of the panel reflectance in isolation. Instead, a combination of both reflectance factors may be more appropriate, based on the relative proportion of diffuse and direct irradiance (Gu et al, 1992). A further complication arise using a Spectralon™ doped with black pigment to produce a spectrally flat grey reference panel to quantify the solar radiation avoiding loss in dynamic pixels range of the CCD array compared to a optical white reference panel. The grey panel used in the VTTVIS setup showed at the front page only appear near-Lambertian for solar altitudes above 60°. Under Danish conditions the solar altitude never exceeds 58°. Thus, the angular dependence in non-Lambertian behaviour of grey

Spectralon™ should be modelled estimating the irradiation under field condition. Since all the reflectance spectra estimations within an object line are based on the irradiation quantification from the grey panel it is particularly important to be able to obtain the true hyperspectral irradiation level.

The analysis of the ray tracing for the PGP spectrograph showed a spectral calibration was necessary for each of the 242 spatial rows. Fortunately it was possible to construct a spectral calibration model for the whole CCD by fitting a 2nd order polynomial across the 242 spatial rows for each of the estimated parameters from the individual spectral polynomial fittings. Inspired by this a empirical calibration models covering the whole CCD array in the VTTVIS system were developed based peaks from gas excitation lamps. The model was further developed enabling a fast verification and calibration procedure under field conditions using the solar spectrum. Although these models are semi-empirical solutions, they perform better than the methods described in literature (Hagman 1996). Correction for the Fraunhofer lines in the solar spectrum will require a spectral correction prior to dividing the pixels within the object line with the irradiation estimation from the grey panel of the VTTVIS. However the spatial image distortion is the most important factor to remove or minimise performing classification and quantifications on pixel basis. Thus, a combined correction model for image distortion in the spatial and spectral direction is required. A procedure for collecting the empirical basis for such a model has been suggested. Prior to the latter procedure models removing or minimising any other systematic noise sources such as e.g. FPN and PRNU from the VTTVIS must have been developed and parameterised. The principles and the impact of these error sources have been described in this report. However it has not been possible within the scope of this project to remove these error sources to a satisfactory degree. There are several reasons to this but the main reason is due to the performance limitations of the VTTVIS system itself. The clamp arrangement used to mount the SBIG camera to the spectrograph (see section 4.4 on page 64) does definitely not encourage any development of highly accurate correction models. Further the SBIG camera seems to introduce severe quantification noise for signal counts exceeding only one sixth of the specified bit range. Assume it was possible to remove all pattern noise and random noise sources the smearing of the rays from an object point focused at the CCD array for wavelengths less than 450 nm and/or located off-axis in the slit perimeter can perhaps cause problems estimating an empirical model correcting the image distortion.

7 Conclusion

The main conclusions which can be drawn from this report are:

- I. The primary aim has been fulfilled giving a detailed description of the VTTVIS line imaging spectrometer used at The Department of Agricultural Sciences, AgroTechnology, KVL, Denmark, for hyperspectral measurements in the visual range
- II. The secondary aim has also been fulfilled by describing the potential error sources within the separate units of the VTTVIS system and the for the system working as a unit
- III. The third aim developing procedures for adjusting and calibrating the system has only been partly fulfilled. Procedures on how to perform the following tasks has been described:
 - a. Axis alignment
 - b. Back focal length alignment
 - c. Focussing the front lens
 - d. Hyperspectral calibration by use of gas excitation lamps
 - e. Hyperspectral calibration and verification based the solar spectrum

Two crucial calibration procedures have only been described partly. The hyperspectral flat-fielding procedure has in fact been fully described, but due to a too cold light source and significant noise in the camera it was not possible to verify its validity. Due instrument limitations it was only possible to present novel ideas with concern to the final and most important procedure. However an alternative and relative simple procedure using the solar light under field condition has been shown to some extent being able to compensate for a proper flat-field correction image.

Besides the main conclusions some additional can be made:

1. Several potential error sources can be avoided by carefully selecting high quality lenses and cameras
2. The clamp system mounting the camera to the PGP spectrograph should be altered
3. Large fixed pattern noise probably due to PRNU within the SBIG camera reduced the given 16 bits range to an actual 13½ bits range
4. Image distortion in the spatial direction can potentially have a significant impact on plant related indices within transition zones like moving from leaf to soil object pixel leading to bad conclusions or estimates
5. No publications was found correcting for or even describing the spatial image distortion within PGP based systems
6. Performance limitations within the VTTVIS system prevents full utilisation of the described adjustment, calibration and correction procedures
7. Knowledge gained in this report creates a valuable basis for building a new and better hyperspectral imaging system

8 Perspectives

The last additional conclusion in this report stated that the knowledge build up and described created a valuable basic for building a new and better hyperspectral imaging system. Therefore an application for a new project utilising the full potential of a new improved hyperspectral imaging system has been written with offset in this report and the knowledge obtained fulfilling the primary aim of the Ph.D. project. Thus in order to put this work into perspectives the core of the application will be presented here hopefully inspiring other scientists to carry on within this area.

By combining lines from a line imaging spectrograph in a sequent manner it is possible to construct an image of a canopy with both a high spatial resolution and a high spectral resolution. A.G.T. Schut and J.J.M.H. Ketelaars (2001a) have shown the latter images may be used to estimate e.g. blue edge, green edge, and green edge images of a grass canopy as shown in Figure 91.

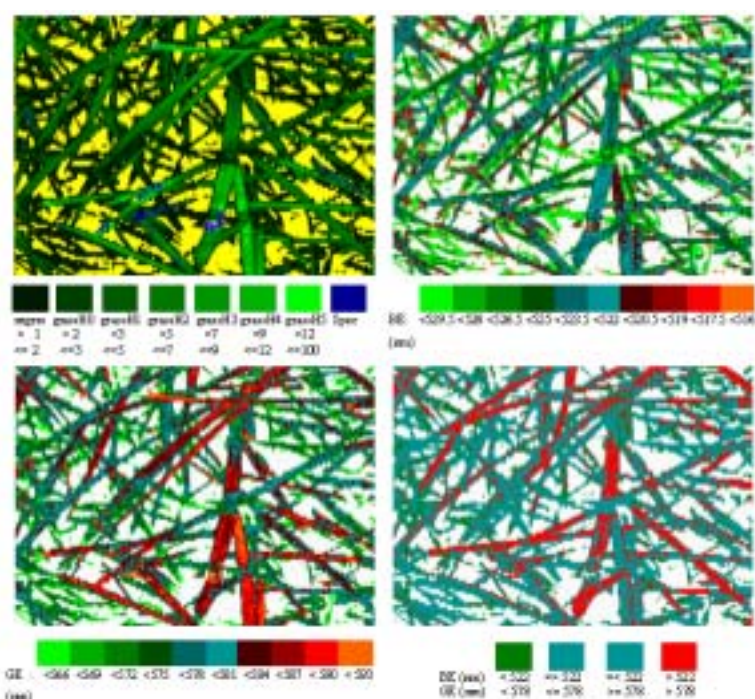


Figure 91: Images of 100 adjacent image-lines, representing an area of 10*15.2 cm. Left top: classified image, for each reflection intensity class the upper and lower boundary of the reflection percentage at 550 nm is given. Right top: position of the blue edge (BE). Left bottom: position of the green edge (GE). Right bottom: combined BE and GE position (Schut and Ketelaars 2001a).

The images in Figure 91 assume there is not any or only a minor image distortion from the Inspector system in the spatial direction. However, this is probably wrong since there is image distortion in both the spatial and the spectral direction within the image of the line projected on the CCD by the Inspector unit. However, the technology has developed since 1995 where the VTTVIS was build and it is therefore expected that a model straightening up the image can be developed if designing a new system. Furthermore the enhanced series of the Inspector spectrographs have only 1/10th of the bending and

keystone values compared to the older PGP spectrographs (Esko Herrala, *pers. comm.* 2002).

8.1 The application based on this report

8.1.1 Background

Spectral reflectance of leaves provides several options for the derivation of their structure and physiology by quantifying the patterns in both the visible and near infrared spectra. Thus, accurate spectral characterisation at both leaf and canopy levels will allow improved optical determination of plant physiological factors related to nutrient deficiencies and other injuries caused by external stress like pests and climate. Science has for more than a century tried to describe and quantify the latter relations between canopy reflectance and plant physiological status (Mestre 1935; Shull 1929; Younes et al. 1974). A number of spectral indices have been proposed for this purpose (Broge and Leblanc 2001; Chen 1996; Datt 1999; Daughtry et al. 2000; Dusek et al. 1985; Wiegand et al. 1991). Ideally a spectral measure should be highly sensitive to vegetation, insensitive to soil background, irradiance strength and direction, and phenological stage. None the spectral indices can fully meet these criteria (Jackson et al. 1983; Wessman 1990).

Hyperspectral imaging sensors, with a spatial resolution of a few mm², have been used for crop and weed species classification by several authors only using the spectral information of the single pixels and not the pattern of the pixels within the image (Borregaard 1997; Borregaard et al. 2000). Hence, the (Feyaerts et al. 1999c; Feyaerts et al. 1999a; Nielsen et al. 1999; Nielsen et al. 2000; Nielsen and Henriksen 1996; Pollet et al. 1999) spatial or shape information have not been included, yet. However, hyperspectral reflectance of vegetation plants and weeds show spatial and temporal variation due to different nutrient levels, competition with other vegetation plants, herbicides, insects, and so on. On the other hand projects applying broadband imaging only utilizing 1-3 broadbands have performed similar attempts of classification. However, overlapping leavers within and/or between the plant species cause serious stability problems for the algorithms. Further, the broadband domain imaging is not capable of precise color matching, due to strong dependency of this domain on factors like spectral power distribution of the light source and object geometry. By using hyperspectral imaging it can be proven images can be made independent of the light source (color constancy) and object geometry (normalize color constancy) (Polder et al. 2000; van der Heijden et al. 2000). Having color constancy it is assumed that all pixels have a response in the linear domain of the sensor and that shadowed objects receive radiation of similar composition as the unshadowed parts. In canopies this assumption will be violated due to the wavelength dependent light transmission of the leaves (A.G.T. Schut, Plant Research International, *pers. comm.* 2002).

Nitrogen diagnostics and quantification has been performed on different crops by use of hyperspectral imaging (Dumont and De Baerdemaeker 2001; Jørgensen 2000; Nielsen et al. 2000; Schut and Ketelaars 2001d). Water stress and grass sward quality have also been assessed by Plant Research International in the Netherlands (Schut and Ketelaars 2001c; Schut and Ketelaars 2001b). None of the authors have utilised the valuable information available if applying pattern or shape imaging analysis principles.

By combining classification techniques and nutrient diagnostics techniques hyperspectral imaging will reveal new unexplored potentials. It will for example

be possible to estimate plant performance for each crop within e.g. an organic intercropping system independent of weeds. However, in order to secure reliability of such an estimation hyperspectral pattern analysis techniques should be included in the algorithms. At Plant Research International A.G.T. Schut is working on applying the shape information to nutrient diagnostic algorithms separating clover and grass prior to hyperspectral nutrient diagnosis. However, this work is not published yet (A.G.T. Schut, Plant Research International, *pers. comm.* 2002).

8.1.2 Project outline

8.1.2.1 Title

Application of hyperspectral imaging for remote estimation of plant performance e.g. in intercropping systems

8.1.2.2 Hypothesis

Plant performance can be estimated remotely for each of the species grown within e.g. an intercropping system by use of hyperspectral imaging

8.1.2.3 Aim

To develop a reliable hyperspectral imaging system and algorithms capable of quantifying species specific plant performance within intercropping systems grown under natural field conditions including weed interference

8.1.3 Specific demands to the hyperspectral imaging system

The combination of high spatial and high spectral resolution requires high irradiance levels throughout the canopy profile. Direct light, contrary to diffuse light, can be focused on a small area minimizing energy inputs. When light is projected under an angle on a surface, shadows will be produced. To minimize this effect, the angle between light beam and measured reflection should be minimized (Schut et al. 2000). Further the irradiation level over the spectral range should be optimised to compensate the decreasing sensitivity of silicon based CCD arrays towards the near infrared range.

The system should be able to scan an area of approx. 500 x 500 mm with a spatial resolution of at least 1 mm² with a speed of at least 2 lines per second. Further the shape of the pixels should be as square as possible. Therefore it will be necessary to use a relatively narrow slit width of approx 20 µm if the line width is to be 50 cm.

8.1.3.1 The Inspector unit

The Inspector unit should have a spectral range of approx. 400-1000 nm. The Inspector V9 has an approved range of 430-900 nm using a Standard 2/3" CCD (6.6 x 8.8 mm). However using a CCD with a greater height the spectral range of the Inspector V9 can be enhanced according Specim Ltd., Finland. The size of the CCD should be approx. 8.4 mm in the spectral direction to obtain a spectral range of 400-1000 nm.

8.1.3.2 The CCD camera

The CCD camera should be at least a 12 bit – preferably a 16 bit cooled camera capable of measuring at least 2 full frames per second. Further it should be possible to perform binning in both directions.

Due to the image distortion the “true” hyperspectral image must be estimated by use of interpolation. To make this possible there must be no or almost not hyperspectral interference in the quantum efficiency between the pixels (see section Figure 35 on page 35).

Hamamatsu has a camera which could potentially fulfil the latter demands. The Hamamatsu Orca ER (C4742-95-12ER) is a B/W CCD digital camera using a progressive scan interline CCD chip (ER 150 chip) with high sensitivity in the VIS-NIR region and substantially better noise characteristics at high frame rates. The Peltier cooled, hermetically sealed vacuum head is cooled to -20 °C, reducing dark noise and minimizing thermal drift which makes this camera an ideal choice for demanding scientific applications. However it will be necessary to rotate the camera to obtain a spectral range of 400-1000 nm. By doing this the full slit width of 8.8 mm cannot be utilized fully since the CCD height is only 6.6mm. By not using the perimeter of the slit will also lower the extent of the image distortion.

8.1.3.3 Assembling the Inspector and CCD camera

The empirical models used for the correction of the hyperspectral image distortion demands the mounting or the location of the CCD camera is always exactly the same in relation to the Inspector imaging plane. This will demand that the camera mount has several very accurate adjustments options. It must be possible to adjust the CCD camera in all three x, y, z directions and also in the rotational direction.

8.1.3.4 Illumination

The illumination should be one or several stabilized light sources or flashes. The overall spectral power composition of these sources should be optimised to the spectral quantum efficiency of the system. This will ensure a good dynamic range of the system over the whole spectral range.

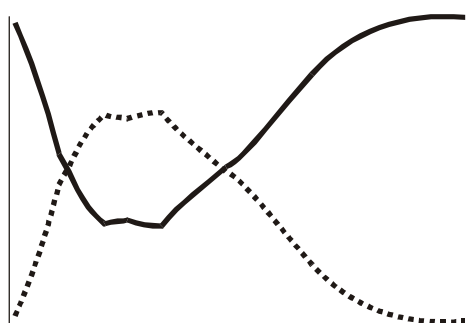


Figure 92: Schematic representation of the spectral power distribution of the light source (the full line) compensating for the varying quantum efficiency of the overall Inspector system (the punctuated line).

The angle between the light beam projected onto the canopy measuring line and the reflected light entering the measuring system should be as small as possible minimizing shadow effects (Schut et al. 2000).

It is preferable that none of the illuminators have peaks within their spectrum since this will disturb the image correction models significantly due to the discrete nature of a CCD array.

8.1.3.5 Varying focus depths

The focus depth varies along the image line as shown in Figure 20 on page 20. Therefore the distance between the canopy and focusing lens should not be too close in order to ensure a certain range where the amount of focus loss is regarded as acceptable. Since the spatial resolution should be approx. 1 mm the circle of confusion should not exceed $\frac{1}{2}$ mm for ± 10 cm from the preset focus distance if possible (see also 3.2.2.9 on page 20).

8.1.3.6 The measuring chamber

The main concept of the chamber shown in Figure 93 is based on the system described by A.G.T. Schut *et al.* (Schut *et al.* 2000).

The dimensions of the chamber are approx. 240 x 100 x 100 \pm 20cm (length, width, and height). The chamber should be constructed of light materials in a very rigid way minimising displacements and vibrations during a scanning session. Further the chamber is light tight letting not external light enter. All inside surfaces are painted in matte black minimising reflections. The outside surface is highly reflective avoiding heating within the chamber when sampling in sunny conditions.

The height of the chamber can be adjusted by the controlling software ± 20 cm ensuring optimal focus conditions under varying canopy heights. The top of the canopy is sensed by use of a 50 cm wide bar of photodiodes as shown in Figure 93.

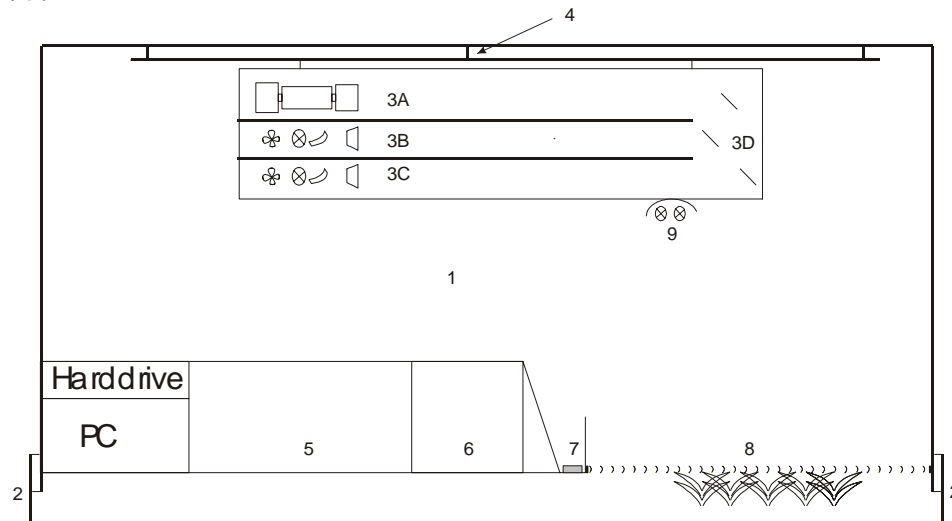


Figure 93: Schematic illustration of the Hyper-spectral Imaging Sampling System (HISS). 1 ~ The chamber is shutting out all external light source like e.g. the sun. 2 ~ A sliding system for height adjustment. 3A ~ The Inspector line imaging system with a cooled CCD camera. 3B & 3D ~ Primary and secondary illumination sources equipped with a bar lens and a filter adjusting the spectral power distribution. 3D ~ Fixed mirrors. 4 ~ Translation table. 5 ~ Electronics. 6 ~ Manuals, spare parts and tools. 7 ~ Spectralon reflectance standard. 8 ~ Sensor for adjusting the chamber height. 9 ~ gas excitation lamps for spectral verification and calibration.

As mentioned earlier a minimum of distance is needed for obtaining acceptable focus depth. In this case 2 meter is evaluated as acceptable. In order to minimize the height of the chamber mirrors are used to redirect the path of vertical reflected light and the illumination beam 90°. Another reason to redirecting the light path to a horizontal direction is to minimise the height of the chamber. This will lower the impact of wind under field conditions.

The translation table should be able to move in steps of $\pm 1/2$ mm in a fast and accurate way.

The measuring system consisting of the Inspector V9, the CCD camera, and the focus lens is mounted within the box under the translation table in a way so it is possible to perform adjustments in all directions and rotational directions. Further a heat-isolating layer is placed between the system and the illumination system.

The illumination is stabilized light sources or flashes with no peaks within their spectra optimised to even out the spectral quantum efficiency of the overall measuring system. Furthermore specialized filters will be put into the light beam to obtain the best possible spectral power composition of the illuminator. A fan will be used cooling the light sources.

A 60 x 5 cm Spectralon™ reflectance standard is used to measure the overall spectral power distribution of the illumination beam. Further the bar is used for verification and spectral calibration of the system by reflecting the light from gas excitation lamps with known peaks. When the verification or calibration is ended the Spectralon™ is sealed protecting the surface from dust and dirt.

The PC hosting the controlling software should be vibration and dust secured. The images are stored at an external Hard Drive (HD) with firewire/1394 or USB-2 connection. The external HD should be mounted in a vibration and dust protected box enabling use of indoor system and thereby minimizing costs. The benefit of using external HD with firewire or USB-2 is that the huge amounts of data easily can be transported back to the office and analysed directly from the HD the data was stored at in the field. The PC should also be equipped with wireless Ethernet enabling remote control of the whole system via e.g. PCANYWARE.

8.1.3.7 The software

The system software controlling the whole system should be able to act as slave for a master Graphic User Interface (GUI) hosted by Matlab. This setup is to be preferred since Matlab cannot really handle multi threads and real time programming. Matlab is however a very flexible software system enabling a fast construction of advanced and flexible GUIs minimizing the restrictions to the scientists using the system within various areas. This is the main reason for the master – slave setup.

It is beyond the scope of this document to describe the whole software system in details. However listed below are some of the actions which could be sent from the master GUI to the slave software giving an idea of the demands to the slave software:

1. Initiate calibration routines like e.g.
 - a. Focus of front lens
 - b. Back focal length
 - c. CCD rotation
 - d. CCD position in the horizontal and vertical direction
2. Goto position x
3. Set exposure

4. Take image
5. Set data and comments to be stores with the image
6. Set filename
7. Ask for status
8. Set path
9. Set take image conditions
10. Set take image series conditions (e.g. start position, step size, and end position)
11. Take image series
12. Open/close to reference bar
13. Set chamber height
14. Get chamber height
15. Get status from canopy height sensor bar
16. Get maximum pixel count
17. Get pseudo RGB image (ultra fast scan in only 3 broad bands)

9 Reference list

- Aikio,M. Optisk komponent. VTT Electronics. [FI000090289B], 1-11. 1994. Finland. *Patent*.
- Aikio,M. Optical component comprising prisms and a grating . Valtion Teknillinen Tutkimuskeskus. 93907891.1[EP 0 635 138 B1], 1-6. 1995. Finland. *Patent*.
- Alonso,M. and J.F.Edward. 1972a. "Diffraction." *Physics*. Addison-Wesley Publishing Company. Massachusetts. 696-718.
- Alonso,M. and J.F.Edward. 1972b. "Inteference." *Physics*. Addison-Wesley Publishing Company. Massachusetts. 668-695.
- Alonso,M. and J.F.Edward. 1972c. "Wave geometry." *Physics*. Addison-Wesley Publishing Company. Massachusetts. 643-667.
- Åstrand,E., M.Österberg, and A.Åström. 1996. "Near-sensor real-time imaging spectroscopy for industrial applications." *SPIE Proceedings*. 2661:154-165.
- Baier,S. CCD imaging systems. Burr-Brown Corporation, 7.1-7.30. 2001. *Electronic Citation*.
- Batthey,D.E., J.B.Slater, R.Wludyka, H.Owen, D.M.Pallister, and M.D.Morris. 1993. "axial transmissive f/1.8 imaging raman spectrograph with volume-phase holographic filter and grating." *Applied Spectroscopy*. 47:1913-1919.
- Bennedsen,B.S. and P.Rasmussen. 2001. "Plant spectra classification by neural networks." In G.Grenier and S.Blackmore, editors, Agro Montpellier. Montpellier, France. (June 2001):151-156.
- Bennedsen,B.S., P.Rasmussen, and H.Nielsen. 2000. "Crop growth information from line spectrometer data using neural networks." *Agricultural Engineering*.00-PA-007.
- Borregaard,T. Application of imaging spectroscopy and multivariate methods in crop-weed discrimination. 1-174. 1997. The Royal Veterinary and Agricultural University, Department of Agricultural Science. *Ph.D. Thesis*.
- Borregaard,T., H.Nielsen, L.Norgaard, and H.Have. 2000. "Crop-weed discrimination by line imaging spectroscopy." *Journal Of Agricultural Engineering Research*. 75:389-400.
- Braam,B., J.Okkonen, M.Aikio, K.Mäkisara, and J.Bolton. 1993. "Design and first test results of the Finnish Airborne Imaging Spectrometer for different Applications, AISA." *SPIE Proceedings*. 1937:142-151.
- Broge,N.H. and E.Leblanc. 2001. "Comparing prediction power and stability of broadband and hyperspectral vegetation indices for estimation of green leaf area index and canopy chlorophyll density." *Remote Sensing of Environment*. 76:156-172.
- Burke,M.W. 1996. *Image acquisition*. Chapman & Hall. London.
- Chen,J.M. 1996. "Evaluation of vegetation indices and a modified simple ratio for boreal application." *Canadian Journal of Remote Sensing*. 22:229-242.

- Datt,B. 1999. "A new reflectance index for remote sensing of chlorophyll content in higher plants: Tests using Eucalyptus leaves." *Journal of Plant Physiology*. 154:30-36.
- Daughtry,C.S.T., C.L.Walthall, M.S.Kim, E.B.de Colstoun, and J.E.Mcmurtrey. 2000. "Estimating corn leaf chlorophyll concentration from leaf and canopy reflectance." *Remote Sensing of Environment*. 74:229-239.
- Dickson,L.D., R.D.Rallison, and B.H.Yung. 1994. "Holographic polarization-separation elements." *Applied Optics*. 33:5378-5385.
- Dumont,K. and J.De Baerdemaeker. 2001. "In field wheat nitrogen assesment using hyperspectral imaging techniques." In G.Grenier and S.Blackmore, editors, *Agro Montpellier*. Montpellier, France. (June 2001):905-910.
- Dusek,D.A., R.D.Jackson, and J.T.Musick. 1985. "Winter wheat vegetation indices calculated from combinations of seven spectral bands." *Remote Sensing of Environment*. 18:255-267.
- Eisberg,R.M. and L.S.Lerner. 1982. "Wave Optics." In J.J.Corrigan, editor, *Physics: Foundations and Applications, combined volume*. McGraw-Hill International Book Company. Auckland. 1314-1372.
- Ewing,R.P. and R.Horton. 1999. "Quantitative color image analysis of agronomic images." *Agronomy Journal*. 91:148-153.
- Feyaerts,F., P.Pollet, L.Van Gool, and P.Wambacp. 1999a. "Hyperspectral image sensor for weed selective spraying." *SPIE Proceedings*. 3897:193-203.
- Feyaerts,F., P.Pollet, L.Van Gool, and P.Wambacp. 1999b. "Sensor for weed detection based on spectral measurements." *ASA-CSSA-SSSA*. Madison, USA.1537-1548.
- Feyaerts,F., P.Pollet, L.Van Gool, and P.Wambacp. 1999c. "Vision system for weed detection using hyper-spectral imaging, structural field information and unsupervised training sample collection." *British Crop Protection Council*.607-614.
- Feyaerts,F. and L.Van Gool. 2001. "Multi-spectral vision system for weed detection." *Pattern Recognition Letters*. 22:667-674.
- Filella,I., L.Serrano, J.Serra, and J.Penuelas. 1995. "Evaluating wheat nitrogen status with canopy reflectance indices and discriminant analysis." *Crop Science*. 35:1400-1405.
- Frenning,T. 1984. *Politikens foto 2*. Politikens Forlag A/S. København.
- Guyot,G., F.Baret, and S.Jacquemoud. 1992. "Imaging spectroscopy for vegetation studies." In F.Toselli and J.Bodechtel, editors, *Imaging Spectroscopy: Fundamentals and Prospective Applications*. ECSC, EEC, EAEC. Brussels and Luxenborg. 145-165.
- Hagman,O. On reflections of wood: Wood quality features modelled by means of multivariate image projections of latent structures in multispectral images. 1-281. 1996. Luleå University of Technology. *Thesis*.
- Hahn,F. and A.Y.Muir. 1993. "Weed-crop discrimination by optical reflectance." *Fourth International Symposium on Fruit, Nut, and Vegetable Production Engineering, March 1993*.

- Hatfield, J.L. and P.J.Pinter. 1993. "Remote-sensing for crop protection." *Crop Protection*. 12:403-413.
- Herrala, E. and J.Okkonen. 1996. "Imaging spectrograph and camera solutions for industrial applications." *International Journal of Pattern Recognition and Artificial Intelligence*. 10:43-54.
- Herrala, E., J.Okkonen, T.Hyvarinen, M.Aikio, and J.Lammasniemi. 1994a. "Imaging spectrometer for process industry applications." *SPIE Proceedings*. 2248:33-40.
- Herrala, E. and O.Voutilainen. 1994. *Imaging spectrometer for visible or near infrared spectral range*. VTT Electronics / Optoelectronics. Oulu, Finland.
- Herrala, E., O.Voutilainen, and J.Okkonen. Measurement report of imaging spectrograph. SL 0894-0955004004, 1-7. 1994b. VTT Electronics. *Report*.
- Hoheusle, K.T. Astronomical hyperspectral imaging - Flatfield corrections. Ninkov, Z. and Hornak, J. P. 1-23. 2000. Rochester, NY 14623-5604, Center for Imaging Science, Rochester Institute of Technology. *Report*.
- Holst, G.C. 1998. *CCD arrays, cameras, and displays - Second edition*. SPIE Press.
- Hyvarinen, T., E.Herrala, and A.Dall'Ava. 1998. "Direct sight imaging spectrograph: a unique add-on component brings spectral imaging to industrial applications." *SPIE symposium on Electronic Imaging*. 3302:165-175.
- Jackson, R.D., T.R.Clarke, and M.S.Moran. 1992. "Bidirectional calibration results for 11 Spectralon and 16 BaSO₄ reference reflectance panels." *Remote Sensing of Environment*. 40:231-239.
- Jackson, R.D., M.S.Moran, P.N.Slater, and S.F.Biggar. 1987. "Field calibration of reference reflectance panels." *Remote Sensing of Environment*. 22:145-158.
- Jackson, R.D., P.N.Slater, and P.J.Pinter. 1983. "Discrimination of growth and water stress an wheat by various vegetation indices through clear and turbid atmospheres." *Remote Sensing of Environment*. 13:187-208.
- Janesick, J.R. 2001. *Scientific charge coupled devices*. SPIE Press. Bellingham, Washington.
- Johansson, M. Implementation and evaluation of a real time spectral classification system. 1-37. 1998. Department of Electrical Engineering, Linköping University, Linköping, Sweden. *Thesis*.
- Jørgensen, R.N. Quantitative nitrogen diagnostic in Red Fescue by use of line imaging spectroscopy - By use of multivariate analysis. 2000. Risø National Laboratory, Denmark. *Unpublished course report*.
- Jørgensen, R.N. and P.Rasmussen. Development and design of a Line Imaging Spectrometer Sampler (LISS) - A user manual. Risø-R-1189(EN), 1-44. 2002. Risø National Laboratory, Denmark. *Risø Report*.
- Kimes, D.S. and J.A.Kirchner. 1982. "Irradiance measurement errors due to the assumption of a Lambertian reference panel." *Remote Sensing of Environment*. 12:141-149.
- Labsphere. A guide to reflectance coatings and materials. 1-25. 2001. Labsphere Inc.

- Mäkisara,K. and E.Tomppo. 1996. "Airborne imaging spectrometry in national forest inventory." *IEEE International Geoscience and Remote Sensing Symposium*. 2:1010-1013.
- Melles Griot. Fundamental Optics. <http://www.mellesgriot.com/ch1-00.htm> . 1999. *Internet Communication*.
- Mestre,H. 1935. "The absorption of radiation by leaves and algae." *Cold Spring Harbor symposia on quantitative biology*. 3:191-209.
- Nielsen,H., R.Devantier, and B.S.Bennedsen. 2000. "Multivariate analysis for crop growth information from line spectrometer data." *Agricultural Engineering*. 00-PA-019.
- Nielsen,H. and K.Henriksen. 1996. "Bestemmelse af afgrøders karakteristika ud fra kombinerede spektrale og geometriske informationer fra reflekteret lys.". The Royal Veterinary and Agricultural University, Denmark. *Unpublished paper*.
- Nielsen,H., P.Rasmussen, R.Devantier, and B.S.Bennedsen. Potentials for measuring crop data by analysis of spectral information. [12], 83-92. 1999. Institut für Geodäsie und Geoinformatik, Fachbereich Landeskultur und Umweltschutz, Universität Rostock. Interner Bericht Heft . Bill, R., Grenzdörfer, G, and Schmidt, F.
- Polder,G. and G.W.A.M.van der Heijden. 2001. "Calibration and characterization of spectral imaging systems." The 2nd International Symposium on Multispectral Image Processing and Pattern Recognition, 22-24 October, Wuhan China.
- Polder,G., G.W.A.M.van der Heijden, and I.T.Young. 2000. "Hyperspectral image analysis for measuring ripeness of tomatoes." *ASAE International Meeting*. No. 003089.
- Pollet,P., F.Feyaerts, P.Wambacp, and L.Van Gool. 1999. "Weed detection based on structural information using an imaging spectrograph." *ASA-CSSA-SSSA*. Madison, USA.1579-1591.
- Reusch,S. Entwicklung eines reflexionsoptischen sensors zur erfassung der stickstoffversorgung landwirtschaftlicher kulturpflanzen. 1-156. 1997. Institut für Landwirtschaftliche Verfahrenstechnik der Christian-Albrechts-Universität zu Kiel. *Ph.D. Thesis*.
- Rollin,E.M., D.R.Emery, and E.J.Milton. 1997. "Reference panel anisotropy in field spectroscopy." *Seventh International Symposium on Physical Measurements and Signatures in Remote Sensing*. G.Guyot and T.Phulpin, editors, Balkema, Rotterdam.
- Rollin,E.M., E.J.Milton, and D.R.Emery. 2000. "Reference panel anisotropy and diffuse radiation - some implications for field spectroscopy." *International Journal of Remote Sensing*. 21:2799-2810.
- Santa Barbara Instrument Group. 1993a. *CCD camera operating Manual for the model ST-4X, ST-5 and ST-6*. Santa Barbara Instrument Group. Santa Barbara.
- Santa Barbara Instrument Group. Universal CPU command structure - Supports ST-4X, ST-5, and ST-6 cameras. 1-31. 1993b. Santa Barbara, California, Santa Barbara, California. *Report*.
- Santa Barbara Instrument Group. CCDOPS - Version 4.0 for Windows 95, Macintosh and DOS. Santa Barbara Instrument Group. 1-104. 1998. Santa Barbara, Santa Barbara Instrument Group. *Report*.

- Savitzky, A. and M.J.E. Golay. 1964. "Smoothing and differentiation of data by simplified least squares procedures." *Analytical Chemistry*. 36:1627-1639.
- Schneider Optics Inc. Xenoplan 1.9/35mm - performance data. 2000. Schneider Optics Inc. *Pamphlet*.
- Schut, A.G.T. and J.J.M.H. Ketelaars. 2001a. "Effects of nitrogen stress in grass swards on evolution of ground cover and spectral characteristics of leaf strata." *SPIE Proceedings*. 4542.
- Schut, A.G.T. and J.J.M.H. Ketelaars. Imaging spectroscopy. 2001b. Plant Research International, Wageningen, The Netherlands. *Pamphlet*.
- Schut, A.G.T. and J.J.M.H. Ketelaars. Imaging spectroscopy for detection of drought stress. 2001c. Plant Research International, Wageningen, The Netherlands. *Pamphlet*.
- Schut, A.G.T. and J.J.M.H. Ketelaars. Imaging spectroscopy for detection of nitrogen stress. 2001d. Plant Research International, Wageningen, The Netherlands. *Pamphlet*.
- Schut, A.G.T., J.J.M.H. Ketelaars, J. Meuleman, J.G. Kornet, and C.K. Lokhorst. 2000. "Imaging Spectroscopy for characterization of spatially heterogeneous canopies." In C. Zhao, editor, *Progress of Agricultural Information Technology. International symposium on intelligent agricultural information technology*. Beijing World Publishing Corporation, China. Beijing. 288-293.
- Searcy, S.W. 1989. "Machines see red... and so much more." *Agricultural Engineering*. November/December:10-15.
- Shull, C.A. 1929. "A spectrophotometric study of reflection of light from leaf surfaces." *The Botanical Gazette*. 87:583-607.
- Spectral Imaging Ltd. 1997. *Inspector - imaging spectrograph - user manual*. Spectral Imaging Ltd., Finland.
- Spectral Imaging Ltd. 1999a. *Application note 1 - Real-time imaging spectrometry for surface inspection and on line machine vision*.
- Spectral Imaging Ltd. Imaging Spectrometry. <http://www.specim.fi/aboutim.html> .
- 1999b. Spectral Imaging Ltd. *Internet Communication*.
- Spectral Imaging Ltd. 1999c. *Technical note 2 - Use of order blocking filter (OBF) with ImSpector*.
- Spectral Imaging Ltd. 2000. *Inspector - imaging spectrograph - user manual*. Spectral Imaging Ltd., Finland.
- Stokman, H.M.G., Th. Gevers, and J.J. Koenderink. 2000. "Color measurement by imaging spectrometry." *Computer Vision and Image Understanding*. 79:236-249.
- Texas Instruments. TC241 - 780- x 488-pixel CCD image sensor. 1-18. 1991. *Report*.
- Thermo Oriel. Pencil style spectral calibration lamps. 2001. *Catalog*.
- Vaarala, T. 1994. *Imaging spectrograph - users manual*. VTT Electronics, Finland.

- Vaarala,T. and M.Aikio. 1997. "An advanced prism-grating-prism imaging spectrograph in on-line industrial applications." *SPIE Proceedings*. 3101:322-330.
- van der Heijden,G.W.A.M., G.Polder, and Th.Gevers. 2000. "Comparasion of multispectral images across the internet." *SPIE Proceedings*. 3964:196-206.
- Waltershea,E.A., C.J.Hays, M.A.Mesarch, and R.D.Jackson. 1993. "An improved goniometer system for calibrating field reference- reflectance panels." *Remote Sensing of Environment*. 43:131-138.
- Weast,R.C. and M.J.Astle. 1982. *CRC Handbook of Chemistry and Physics*. CRC Press. Boca Raton, Florida.
- Wessman,C.A. 1990. "Evaluation of canopy biochemistry." In R.J.Hobbs and H.A.Mooney, editors, *Remote sensing of biosphere functioning*. Springer-Verlag. New York. 135-156.
- Wiegand,C.L., A.J.Richardson, D.E.Escobar, and A.H.Gerbermann. 1991. "Vegetation indexes in crop assessments." *Remote Sensing of Environment*. 35:105-119.
- Younes,H.A., R.M.Abel-Aal, M.M.Khodair, and A.G.Abel-Samie-. 1974. "Spectral reflectance studies on mineral deficiency in corn plants." Willow Run Laboratories - Environmental Research Institute of Michigan. Michigan.1105-1124

Title and authors

The VTTVIS line imaging spectrometer - Principles, Error sources, and Calibration

Rasmus Nyholm Jørgensen

ISBN		ISSN	
87-550-2967-1; 87-550-2969-8 (Internet)		0106-2840	
Department or group		Date	
Plant Research Department		28 Feb. 02	
Groups own reg. number(s)		Project/contract No(s)	
		1310116-0-9	
Pages	Tables	Illustrations	References
113	7	93	89

Abstract

Hyperspectral imaging with a spatial resolution of a few mm² has proved to have a great potential within crop and weed classification and also within nutrient diagnostics. A commonly used hyperspectral imaging system is based on the Prism-Grating-Prism (PGP) principles produced by Specim Ltd. Finland. One of the novel systems based on the PGP spectrograph (VTTVIS) was build by The Department of Agricultural Sciences, AgroTechnology, KVL, Denmark, in 1995. Several other agricultural institutions have now implemented the technology in their research. None of these has published any thoroughly work describing the basic principles, potential error sources, and/or adjustment and calibration procedures. This report fulfils the need for such documentation with special focus on the system at KVL.

The PGP based system has several severe error sources, which should be removed prior any analysis. Most of the random noise sources can be minimised by carefully selecting high-grade components especially with concern to the camera. Systematic error sources like CCD fixed pattern noise (FPN), CCD photoresponse nonuniformity (PRNU), CCD charge transfer efficiency (CTE), slit width variations, changes in off-axis transmission efficiencies, diffraction efficiencies, and image distortion have a significant impact on the instrument performance. Procedures removing or minimising these systematic error sources are developed and described for the system build at KVL but can be generalised to other PGP based systems.

The know-how achieved is put into perspectives describing novel ideas for a new scanning hyperspectral imaging system and potentials estimating species specific plant performance within a multi cropping system.

Descriptors INIS/EDB

Available on request from Information Service Department, Risø National Laboratory,
(Afdelingen for Informationsservice, Forskningscenter Risø), P.O.Box 49, DK-4000 Roskilde, Denmark.
Telephone +45 4677 4004, Telefax +45 4677 4013